

**MATERIALS AND NANOSTRUCTURES FOR  
LIGHT-MATTER INTERACTIONS IN 2D**

A THESIS SUBMITTED TO THE UNIVERSITY OF MANCHESTER

FOR THE DEGREE OF DOCTOR OF PHILOSOPHY

IN THE FACULTY OF SCIENCE AND ENGINEERING

2021

**TONGCHENG YU**

DEPARTMENT OF PHYSICS AND ASTRONOMY

# Contents

<b>List of Figures and Tables.....</b>	<b>5</b>
<b>Abstract.....</b>	<b>11</b>
<b>Declaration.....</b>	<b>13</b>
<b>Copyright Statement.....</b>	<b>14</b>
<b>Acknowledgments .....</b>	<b>15</b>
<b>1. Introduction.....</b>	<b>16</b>
1.1 Background and research interest .....	16
1.2 Graphene .....	21
1.2.1 Band structure .....	21
1.2.2 Electrical and optical property .....	22
1.3 MoS <sub>2</sub> .....	24
1.4 Electro-optical modulators.....	26
1.4.1 Basics of optical modulators .....	26
1.4.2 Electro-optical modulators based on 2D material.....	28
1.5 Surface plasmon polaritons (SPPs).....	30
1.5.1 Developments of plasmonics .....	30
1.5.2 Maxwell's equations and Drude model for metals .....	33
1.5.3 Surface plasmon polaritons (SPPs) and its waveguides .....	35
<b>2. Methods and techniques .....</b>	<b>43</b>
2.1 Fabrication .....	43
2.1.1 Sample preparation: mechanical cleavage or wet transfer.....	43
2.1.2 Photolithography and Patterning.....	46
2.1.3 Electron beam lithography .....	48
2.1.4 Deposition and lift-off.....	49

2.2 Characterisation techniques .....	51
2.2.1 Raman spectroscopy .....	51
2.2.2 Atomic force microscopy .....	52
2.2.3 Scanning electron microscopy .....	53
2.2.4 X-ray photoelectron spectroscopy .....	54
2.2.5 Ellipsometry .....	54
2.2.6 Fourier transform infrared spectroscopy .....	56
2.2.7 Electronic transport measurements .....	57
2.2.8 Finite-Difference Time-Domain simulation .....	58
<b>3. A MoS<sub>2</sub> electro-optical modulator based on Fabry-Perot structure .....</b>	<b>59</b>
3.1 Introduction.....	59
3.2 Sample preparation .....	61
3.3 Normal reflection .....	63
3.4 Reflection modulation with gate voltage at oblique incidence .....	64
3.5 Optical constant analysis from ellipsometry .....	66
3.6 Lorentzian dispersion model.....	68
3.7 Transfer matrix modeling .....	72
3.8 Conclusion .....	74
<b>4. A graphene plasmonic slot waveguide modulator .....</b>	<b>75</b>
4.1 Introduction.....	76
4.2 Device structure and fabrication methods.....	77
4.3 Experimental setup and transmission modulation .....	80
4.4 Concept of light field imaging in 2D .....	85
4.5 Light propagation in plasmonic slot waveguides.....	87
4.6 Nanoscale light field imaging in graphene .....	89
4.7 Conclusion .....	98
<b>5. An effect of dielectric fabrication techniques on graphene gating .....</b>	<b>99</b>

5.1 Introduction.....	99
5.2 Device structure and fabrication methods.....	101
5.3 Positive and negative gating hysteresis.....	103
5.4 Dependence of graphene gating characteristics for four samples with dielectrics fabricated by ALD and e-beam evaporation .....	105
5.5 XPS analysis of the dielectrics' properties .....	108
5.6 Discussion .....	111
5.7 Dependence of graphene gating characteristics on sweeping range and speed .....	112
5.8 Gate-induced electron density measured with the help of FTIR spectroscopy.....	114
5.9 Hysteresis at non-continuous sweeps and temperature dependence.....	117
5.10 Conclusion .....	119
<b>Conclusions and outlook .....</b>	<b>121</b>
<b>Publications .....</b>	<b>125</b>
<b>Conferences .....</b>	<b>126</b>
<b>References.....</b>	<b>127</b>
<b>Word count (excluding references):</b>	<b>26623</b>

# List of Figures and Tables

<b>1.1</b>	Electronic band structure of graphene calculated by the tight-binding model.....	<b>22</b>
<b>1.2</b>	Ambipolar electric field effect in graphene on Si/300 nm SiO <sub>2</sub> . Positive/negative gate voltage $V_g$ induces electrons/holes in graphene, changing its resistivity.....	<b>22</b>
<b>1.3</b>	(a) Microscope image of an exfoliated graphene on Si/290 nm SiO <sub>2</sub> wafer (b) The corresponding Raman spectroscopy of graphene ( $\lambda_{exc}=532$ nm), measured by Horiba XploRA PLUS Raman spectrometer.....	<b>23</b>
<b>1.4</b>	Theoretical calculation of the optical conductivity of graphene at different Fermi energies 0.1 eV, 0.3 eV, and 0.6 eV.....	<b>24</b>
<b>1.5</b>	(a) Atomic structure of monolayer MoS <sub>2</sub> . (b) Bandgap transition of MoS <sub>2</sub> from indirect to direct for different layer numbers: bulk, quadra-layer, bilayer, and monolayer. ....	<b>25</b>
<b>1.6</b>	(a) Optical microscopy image of a MoS <sub>2</sub> monolayer with Si <sub>3</sub> N <sub>4</sub> underneath. (b) Raman spectrum of the monolayer MoS <sub>2</sub> measured with a Witec spectrometer and 632.8 nm laser.....	<b>26</b>
<b>1.7</b>	Different colors resulted from the interaction of light and metal nanoparticles in the Lycurgus cup.....	<b>32</b>
<b>1.8</b>	The boundary of dielectric and metal for surface plasmon polariton.....	<b>37</b>
<b>1.9</b>	The dispersion relations for surface plasmon polaritons (SPPs) and free-space photons.....	<b>40</b>
<b>1.10</b>	Field distribution of the fundamental waveguide mode in cylindrical (a) dielectric	

fiber and (b) metal nanowire with reducing diameters.....	41
<b>2.1</b> Schematic of the fishing process .....	45
<b>2.2</b> Optical image of a large piece of exfoliated graphene on a 290 nm SiO <sub>2</sub> /Si wafer with a 65 μm lateral length. ....	46
<b>2.3</b> Optical image of the sample after the exposure and development.....	47
<b>2.4</b> Optical image of the sample after etching by Ar/O <sub>2</sub> plasma.....	47
<b>2.5</b> Optical image of the patterned graphene on a 290 nm SiO <sub>2</sub> /Si wafer.....	48
<b>2.6</b> Optical image of the contacts connected to graphene after the electron beam exposure and development. ....	49
<b>2.7</b> Optical image of the final sample after the lift-off process.....	50
<b>2.8</b> Schematic of the lithography and lift-off process. For the exposure process, the beam could be either light or electrons with corresponding resist types.....	50
<b>2.9</b> Schematic of Stokes and anti-Stokes modes of Raman scattering.....	51
<b>2.10</b> Schematic of the atomic layer microscopy.....	53
<b>2.11</b> Simplified schematic of the scanning electron microscopy.....	54
<b>2.12</b> Schematic of the ellipsometer setup.....	55
<b>2.13</b> Schematic of a Fourier transform infrared spectrometer.....	56
<b>2.14</b> Electrical circuits of transport characteristic measurements of a simple graphene gating device. ....	58
<b>3.1</b> (a) The schematic of our modulator device. Polarized light emits on MoS <sub>2</sub> at an incident angle and transmits through. (b) Multiple internal reflections caused by	

Au/Si <sub>3</sub> N <sub>4</sub> /MoS <sub>2</sub> Fabry-Perot structure leads to the enhancement of the optical absorption of MoS <sub>2</sub> monolayer.....	<b>62</b>
<b>3.2</b> (a) Contact-mode AFM image of a MoS <sub>2</sub> monolayer with Si <sub>3</sub> N <sub>4</sub> underneath. (b) The measured thickness of the MoS <sub>2</sub> .....	<b>62</b>
<b>3.3</b> (a) Normal incident relative reflectance spectrum at different gate voltages over V <sub>g</sub> = 0 V. (b) Direct reflection spectrum at V <sub>g</sub> = 0 V of our device.....	<b>63</b>
<b>3.4</b> (a) The reflectivity change under different incident angles for (a) s-polarized light and (b) p-polarized light of our Au/Si <sub>3</sub> N <sub>4</sub> /MoS <sub>2</sub> device.....	<b>64</b>
<b>3.5</b> The gate voltage dependence (from -100 V to 100 V) of the reflection change for (a, b) s-polarized light and (c, d) p-polarized light of our Au/Si <sub>3</sub> N <sub>4</sub> /MoS <sub>2</sub> device.....	<b>66</b>
<b>3.6</b> Gate voltage dependence of the complex refractive index of monolayer MoS <sub>2</sub> , extracted from ellipsometric data.....	<b>68</b>
<b>3.7</b> Measured and fitted absorption coefficient of monolayer MoS <sub>2</sub> for different gate voltages.....	<b>69</b>
<b>3.8</b> The parameters of the Lorentzian dielectric function dependent on the gate voltage.....	<b>71</b>
<b>3.9</b> The simulated result of the gate voltage-dependent reflection of differently polarised light based on the transfer matrix method.....	<b>73</b>
<b>4.1</b> Schematics of the antenna-coupled plasmonic slot waveguide device.....	<b>78</b>
<b>4.2</b> (a) SEM image of the plasmonic waveguide device. (b) The microscope image of one device.....	<b>79</b>
<b>4.3</b> The experimental setup. A lamp and CCD camera were used to locate the sample.	

A NIR camera was used to detect input and output signals and measure the light modulation under gating. An optical chopper and lock-in was used to achieve electrical detection of light in the waveguide.....	<b>81</b>
<b>4.4</b> (a) Light transmitted by the waveguide imaged with an InGaAs camera. The waveguide design is superposed on the image for reference. (b) The average intensity of the output light for short and long waveguide structures.....	<b>82</b>
<b>4.5</b> The cross-section schematic of the plasmonic slot waveguide and the gate voltage connection for plasmonic modulation. ....	<b>84</b>
<b>4.6</b> (a) Normalized transmittance when applying a 1 Hz square modulation signal between 1 V and 7 V to both sides of the waveguide while graphene is grounded. (b) Broadband operation test from 1300 nm to 1630 nm.....	<b>85</b>
<b>4.7</b> Schematics of a p-n junction induced in graphene by gating of a plasmonic waveguide.....	<b>86</b>
<b>4.8</b> Lumerical simulation of the electrical intensity at the graphene area.....	<b>88</b>
<b>4.9</b> (a) Simulated electric field distribution excited by a laser beam (wavelength of 1550 nm) that falls onto the input antenna (taken in the plane of the waveguide at the half-height of the waveguide and calculated with the help of Lumerical FDTD solutions). (b) Simulated electric field distribution in the cross-section of the plasmonic slot waveguide calculated with the help of Comsol software.....	<b>89</b>
<b>4.10</b> (a) Fermi energy in initially doped graphene calculated in the presence of a gate voltage applied to one side of the waveguide. (b) A graphene p-n junction position as a function of the gate voltage applied to one side of a waveguide. (c) The electric field of a p-n junction induced in graphene.....	<b>92</b>



<b>4.11</b> (a) The resistance of graphene as a function of the gate voltage applied to both G1 and G2 contacts for a sample with a 30 nm HfO <sub>2</sub> dielectric layer. (b) A photovoltage measured between the source and drain of graphene as a function of the gate voltage G2 when the contact G1 is grounded. The photovoltage was measured with an optical chopper and lock-in amplifier.....	<b>93</b>
<b>4.12</b> (a) A photovoltage (drain voltage in an open circuit) and (b) a photocurrent (drain current in a short circuit) as a function of the gate voltage G2 with and without light input through the waveguide, measured directly with a source meter. Both the source and the G1 contact were connected to the ground.....	<b>95</b>
<b>4.13</b> The linear dependence of the photovoltage on the incident light power with a fixed gate voltage of 0.4 V applied to G2, and G1 contact is grounded.....	<b>95</b>
<b>4.14</b> Comparison of light field profiles with theory. (a) The line scan of the norm of electric field calculated at the graphene position. (b) Comparison of the simulated field profile in the plasmonic slot waveguide with the reconstructed profile obtained with a p-n junction moved in graphene by gating.....	<b>97</b>
<b>5.1</b> (a) The structure schematic of all measured graphene field-effect devices. (b) Optical image of our device: a piece of CVD graphene on the e-beam evaporated Al <sub>2</sub> O <sub>3</sub> above the Au stripe.....	<b>102</b>
<b>5.2</b> Gate voltage-dependent conductance hysteresis. (a) and (b) refers to positive and negative hysteresis, respectively. ....	<b>104</b>
<b>5.3</b> Conductance hysteresis of graphene devices with ALD dielectric material in respect of the gate voltage.....	<b>106</b>

<b>5.4</b> Hysteresis for graphene devices with e-beam dielectric material in respect of the gate voltage. ....	<b>107</b>
<b>5.5</b> X-ray Photoelectron Spectroscopy (XPS) result of ALD and e-beam fabricated HfO <sub>2</sub> and Al <sub>2</sub> O <sub>3</sub> in our experiments. ....	<b>109</b>
<b>5.6</b> Contrasting mechanisms for graphene conductance gating hysteresis effect with ALD or e-beam fabricated dielectric layers.....	<b>112</b>
<b>5.7</b> (a) Extractive data from Figures 5.3a, b, and 5.4b shows the dependence of gating hysteresis on the gate-sweeping range for graphene devices with ALD HfO <sub>2</sub> and ALD/e-beam Al <sub>2</sub> O <sub>3</sub> dielectrics. (b) Dependence of gating hysteresis on the gate-sweeping speed for graphene devices with ALD/e-beam Al <sub>2</sub> O <sub>3</sub> and HfO <sub>2</sub> dielectrics.	<b>114</b>
<b>5.8</b> Relative optical reflection spectra of graphene devices (normalized by the reflection at zero gate voltage) under different gate voltages with alumina dielectrics produced by (a) an e-beam method (b) an ALD method. The spectra were measured by FTIR spectroscopy with the help of a Bruker Vertex 80 system and a Hyperion 3000 microscope. Simulations of the relative reflection of our device at different Fermi energies for alumina produced by (c) the e-beam method (d) the ALD method.....	<b>116</b>
<b>5.9</b> Graphene gating effect measurement with ALD HfO <sub>2</sub> dielectric layer under different bottom gate voltages.....	<b>118</b>
<b>5.10</b> Temperature dependence of hysteresis for ALD Al <sub>2</sub> O <sub>3</sub> graphene device. Positive hysteresis was observed at all measured temperatures.....	<b>119</b>
<b>Table 1.</b> The Fitted multi-Lorentzian parameters for the complex refractive index of the CVD MoS <sub>2</sub> monolayer as a function of gate voltage.....	<b>69</b>

# Abstract

2D material is a perfect candidate for electro-optics with its small footprint, tunable optical properties achieved at low applied voltages, unique optical responses, and complementary metal-oxide-semiconductor (CMOS) compatibility. However, direct usage of 2D materials in this field is difficult due to their poor light absorption (less than 10% for graphene and TMDs).

It is possible to enhance the interaction of light and 2D material with the help of nanostructures. In this thesis, two different nanostructures have been studied (based on MoS<sub>2</sub> and graphene) for high optical modulation depth. A Fabry-Perot (FP) nanostructure was utilized to enhance the absorption of MoS<sub>2</sub>, which achieved a 6 dB visible light polarization-dependent modulation at a narrow range of the excitonic band of MoS<sub>2</sub>; Another plasmonic slot waveguide structure integrated with graphene was studied. Relying on the interaction between graphene and the gap surface plasmon (GSP) mode, a modulation depth of 0.12 dB/ $\mu\text{m}$  was yielded (12% absolute modulation depth) at the telecom wavelength range. The modulation depth of our devices is at the forefront of current optical modulators with the same 2D material.

On the other hand, our hybrid nanostructures offer new approaches to characterize the light-matter interactions in 2D materials. We were first to measure the dependence of the  $n(\lambda)$  and  $k(\lambda)$  spectra for a MoS<sub>2</sub> monolayer on the gate voltage with ellipsometry (see Figure 3.6). We found that the absorption coefficient  $k(\lambda)$  of monolayer MoS<sub>2</sub> is gate-dependent at the excitonic range, and a multi-Lorentzian dispersion model explained this result well; By integrating graphene into the plasmonic slot waveguide structure, we were able to realize a conceptually new method of nanoscale light field

imaging with a lateral resolution of  $\sim 20$  nm, based on the photoelectric effect in a p-n junction induced in graphene, which is not subject to the diffraction limited resolution. This new reliable nanoscale light field imaging method could be used for accurate and deterministic light field characterization in nano-optics.

Finally, to achieve robust operation of the fabricated devices based on a gated 2D material, the dielectric gate separator is essential as it needs to be stable in a relatively large electrical field. Our work found that the gating properties of the dielectric material strongly depend on the dielectric fabrication technique. The dielectric performance of two widely used dielectric materials, hafnia and alumina ( $\text{HfO}_2$  and  $\text{Al}_2\text{O}_3$ ), fabricated by two different methods (electron beam evaporation and atomic layer deposition), was studied, and we found a dramatic change in the hysteresis properties of graphene gating for these two fabrication methods. X-ray photoelectron spectroscopy (XPS) provided a clue that the gating properties strongly depend on the presence of oxygen vacancies.

# Declaration

No portion of the work referred to in the thesis has been submitted in support of an application for another degree or qualification of this or any other university or other institute of learning.

# Copyright Statement

1. The author of this thesis (including any appendices and/or schedules to this thesis) owns certain copyright or related rights in it (the “Copyright”) and s/he has given The University of Manchester certain rights to use such Copyright, including for administrative purposes.
2. Copies of this thesis, either in full or in extracts and whether in hard or electronic copy, may be made **only** in accordance with the Copyright, Designs and Patents Act 1988 (as amended) and regulations issued under it or, where appropriate, in accordance with licensing agreements which the University has from time to time. This page must form part of any such copies made.
3. The ownership of certain Copyright, patents, designs, trademarks and other intellectual property (the “Intellectual Property”) and any reproductions of copyright works in the thesis, for example graphs and tables (“Reproductions”), which may be described in this thesis, may not be owned by the author and may be owned by third parties. Such Intellectual Property and Reproductions cannot and must not be made available for use without the prior written permission of the owner(s) of the relevant Intellectual Property and/or Reproductions.
4. Further information on the conditions under which disclosure, publication and commercialisation of this thesis, the Copyright and any Intellectual Property and/or Reproductions described in it may take place is available in the University IP Policy (see <http://documents.manchester.ac.uk/DocuInfo.aspx?DocID=24420>), in any relevant Thesis restriction declarations deposited in the University Library, The University Library’s regulations (see <http://www.manchester.ac.uk/library/about/regulations>) and in The University’s Policy on Presentation of Theses.

# Acknowledgments

Time flies, and I am going to finish my PhD. I still remember the night when I came to UK for the first time, on the train to my address with my heavy luggage. Now I am on another train, from my student life to my career life. Four-year PhD time is a joyful journey with unforgettable memories, although there was some pain to suffer in the whole process. I have learned a lot along the way in my projects and life in the UK.

Firstly, I would like to thank my supervisor, Sasha Grigorenko. He is a patient, kind, experienced and gentle professor. He has given adequate advice on my projects, from the main direction to the experimental details. Apart from the projects, he always understands and cares about my life. I come from China, and there is an old Chinese saying that a supervisor is the one who preaches, teaches, and advises. Sasha is a perfect supervisor from this perspective. I am lucky to work in his group.

Next, I want to thank Vasyl Kravets. Vasyl is a humorous guy who brought fun to my PhD life, which is very important as research is not always fun. Vasyl is also well-experienced and strict in fabrication and measurements. He taught and helped a lot in my experiments.

Then, I would like to thank Fan, Shinji, Fred, Yapping, and everyone in the cleanroom who helped my experiments. I want to thank my friends Wenjun, Meizhi, Donnach, Kelly, Junhao, Thy, Maolin, Marco for bringing me happiness in my four-year PhD time. I also want to thank Artem, Patrick, and Irina for giving me advice on my projects.

I am grateful to have done some research at the University of Manchester as a PhD student. Finally, thanks to my parents, Xunjun and Yuanfeng.

# Chapter 1

## Introduction

*The first section of this chapter mainly introduces the background, research interests, and primary outcomes of this research (details demonstrated in Chapters 3 to 5). The following sections then briefly present the theoretical knowledge of this research. Basic information of two 2-dimensional (2D) materials (graphene and MoS<sub>2</sub>) used in my devices will be illustrated, and some simple characterization of their properties. The theory of electro-optical modulators and the advantages of 2D materials in this field will be investigated. Lastly, the necessary theory about plasmonics is elaborated, which will be involved in chapter 4, where we will introduce a graphene-based plasmonic waveguide device.*

### 1.1 Background and research interest

The isolation of graphene<sup>1</sup> 17 years ago stunned the field of material science. This ground-breaking material has led to the creation and development of a new field of investigations – 2D materials, which were not thought to exist before graphene was produced by a simple mechanical exfoliation method. Since then, numerous applications based on 2D materials have been studied and investigated, ranging from photodetectors to biosensing technology<sup>2-9</sup>, though they have not yet been widely used in practical applications. Probably, the most practical application of 2D materials is the exploitation of their mechanical properties such as stiffness and flexibility. For example, graphene soles and racquets have been manufactured and sold on the market. However, there are no well-known applications based on the unique optical and



electrical properties of 2D material yet, where there are many potentials. The significant advantage of 2D materials in optics is their tuneable optical properties, which could be easily and significantly modulated by electrical fields<sup>10</sup>, chemical doping<sup>11</sup>, or optical means<sup>12</sup>, including graphene and transition metal dichalcogenides (TMDs), which is particularly beneficial for optical modulation.

An optical modulator is a link between optical emitters and optoelectronic devices. For the electro-optical modulator which we studied in this thesis, it converts an electric signal to an optical signal, where the light intensity is usually modulated by a periodic electric field, which represents the 1/0 signals in digital circuits. An optical modulator aims to provide adequate modulation depth with minimal energy consumption. Particularly for electro-optics, it can be considered to offer the maximum change in the refractive or absorptive index with a minimum applied voltage.

In this case, 2D material is a perfect choice with its small footprint and tunable optical properties. For standard silicon or other semiconductors-based optical modulators, their footprints are usually at the scale of millimeters or even much larger<sup>13-15</sup>. With 2D material, the critical dimension of an optical modulator can be lowered down to micrometer or even nanometer. Besides, many 2D materials are compatible with CMOS technology and other 2D materials to form stacks<sup>2, 16</sup>, with no ‘lattice mismatch’ problem for most bulk semiconductors when integrating with current fabrication technology platforms, thus providing new opportunities for chip-based optical devices.

Furthermore, 2D material has a unique optical response and spectral range that differs from its bulk form. For example, compared to traditionally used mediums for most semiconductor electro-optical technologies, such as Lithium niobate ( $\text{LiNbO}_3$ , in the visible range) and Gallium arsenide (GaAs, in the infrared range), graphene has a

broadband response wavelength range, covering the entire visible and near-infrared range, which is perfectly designed for broadband optical modulation and detection. Besides, the melting point of graphene is at  $\sim 4000\text{ }^{\circ}\text{C}$ <sup>17</sup>, much higher than that of normal bulk semi-conductors<sup>18</sup>. Therefore, 2D materials with electrically tunable optical properties are becoming more popular for electro-optics<sup>2, 3, 19, 20</sup>. It is worth mentioning that the procedure of light generation, propagation, modulation, and detection could all be achieved with 2D material-based structures, pushing the development of ultra-small and ultra-fast photonic circuits<sup>21</sup> forward.

Nevertheless, direct use of 2D material for optical modulation is not a good decision. For example, direct modulation of the light absorption (visible range) of MoS<sub>2</sub> on a SiO<sub>2</sub>(280nm)/Si substrate has a poor performance of only 4% modulation depth with a high gate voltage range -70 V to 80 V<sup>22</sup>. Although the dielectric constant of SiO<sub>2</sub> is not high, the biggest weakness is the poor absorption of MoS<sub>2</sub>. Therefore, different structures have been designed to facilitate the interaction between light and 2D material, such as artificially designing 2D material<sup>23</sup> or coupling 2D material with metal structures<sup>24</sup>, nanoparticles<sup>25</sup>, or other 2D material<sup>26</sup>. In this project, we utilized novel nanostructures to promote the interaction between light and 2D material (including graphene and monolayer MoS<sub>2</sub>), aiming for a reliable optical modulation depth.

In Chapter 3, we used a nanoscale Fabry-Perot (FP) structure to enhance the interaction between light and monolayer MoS<sub>2</sub>. FP structure is made of two parallel reflecting surfaces, making a cavity inside, and optical waves could resonate between these two reflectors<sup>27</sup>. FP structure is widely used in lasers and spectroscopy due to the light intensity enhancement of the resonance-introduced interference in the cavity. In our device, due to the resonance introduced by the FP structure, the interaction between light and MoS<sub>2</sub> is enhanced as well as the optical absorption of MoS<sub>2</sub>. A reliably high

6 dB reflective modulation at the visible range is achieved with our device, which is among the best for MoS<sub>2</sub>-based optical modulators<sup>22,25</sup>. Except for the high modulation depth provided by our structure, we also studied the gating-controlled refractive index of monolayer MoS<sub>2</sub> with the help of ellipsometry (usually used for characterization of film properties by analyzing the ellipsometry parameters change) in Chapter 3. For this device, ellipsometry was utilized to obtain the reflection spectrum for differently polarized light. By applying different gate voltages on our nano-devices and analyzing the corresponding ellipsometric spectra, we obtained the evolution of the complex refractive index of MoS<sub>2</sub> with the gate voltage. A Lorentzian model was proposed to explain the gate voltage-dependent absorption in a MoS<sub>2</sub> monolayer.

In Chapter 4, we used a plasmonic waveguide structure to enhance the light field in graphene, which provides an alternative idea for optical modulation. Plasmonics is known for its sub-wavelength and local enhancement of the light field, which are predicted to be the core key of the next-generation technology<sup>28</sup>. In our structure, a plasmonic waveguide structure is hybridized with graphene. Relying on the interaction between graphene and gap surface plasmon (GSP) mode, we have successfully proposed and demonstrated a graphene plasmonic modulator, featuring a modulation depth of 0.12 dB/ $\mu$ m at the gate voltage amplitude of 6 V, at the telecom wavelength range.

A reliable and non-invasive nanoscale light field imaging is essential for the field of nano-optics, where accurate and deterministic light field characterization is indispensable for device operation as well as for revealing underlying physical mechanisms involved. The possibility to measure near-fields and map their distribution with nanometric precision would be extremely useful for nano-optics and nanotechnology. Light scattering has provided a reasonably good spatial resolution of

the fraction of the light wavelength used but restricted by the diffraction limit. In Chapter 4, with the low critical dimension of both the waveguide plasmonic mode and graphene, we have suggested and experimentally realized an electromagnetic field mapping and imaging based on the photo-detection with a p-n junction induced and moved inside graphene by an external gate voltage. The spatial resolution of our technique can reach 20 nm.

The research of MoS<sub>2</sub>-based FP devices and graphene-based plasmonic slot waveguide devices are two great examples of the integration of 2D material and nanostructures to study the light-matter interaction in 2D, which are promising for electro-optics and nanoscale optical characterization and future on-chip plasmonic devices.

On the other hand, for electro-optics, gating (applying an electric field) is the most practical and easiest method to control the properties of semiconductors or graphene in our research. This requires reasonably stable and relatively large fields on a dielectric gating material. Boron nitride (BN) is a popular material used to encapsulate graphene in nano-devices, especially for the exfoliated graphene. However, it is not practical in the industry where chemical vapor deposited (CVD) graphene is used and a large area of dielectric coverage is essential. Therefore, dielectric material with mass production is needed. Also, the dielectrics need to be transparent at our interest wavelength range. We investigated two dielectric materials, hafnia and alumina (HfO<sub>2</sub> and Al<sub>2</sub>O<sub>3</sub>), widely used in our interest wavelength range, and studied their gating performance. This research discovered an interesting result: the same material produced by different methods can exhibit significantly different gating properties. This result is helpful for the design and fabrication of the dielectric material in electro-optics.

## 1.2 Graphene

### 1.2.1 Band structure

Graphene, described by Andre Geim and Kostya Novoselov in 2004<sup>1</sup>, started the research interest into 2D materials. Graphene shows remarkable electron mobility, and even superconductivity is observed recently in twisted bilayer graphene<sup>29</sup>. Graphene is also the strongest material due to the high strength of its carbon-carbon bond. It is measured to be 200 times higher than steel but flexible and pliable at the same time<sup>30</sup>. Moreover, the mechanical and chemical properties can be tuned by intentional defects or functional groups<sup>30</sup>. Graphene still exhibits unique optical properties as it has a broad absorption spectrum from the visible to infrared range<sup>20</sup>. Moreover, the optical response of graphene can be tuned by changing its Fermi level with an external gate voltage<sup>31</sup>.

The unique electrical and optical properties of graphene are the outcomes of its special band structure. As shown in Figure 1.1, monolayer graphene has two conical points  $K$  and  $K'$  in the Brillouin zone, where the conduction band and valence band crosses<sup>32</sup>. Expanding the full band structure around  $K$  point by  $\mathbf{K} + \mathbf{q}$ , where  $\mathbf{q} \ll \mathbf{K}$  gives the linear dispersion relationship

$$E(\mathbf{q}) = \pm v_F \mathbf{q} \quad (1.1)$$

where  $v_F \approx 1 \times 10^6$  m/s is the Fermi velocity, and  $\mathbf{q}$  is the momentum relative to the  $\mathbf{K}$  point. Further derivation reveals that the charge carriers in graphene can be described by the Dirac equation, and these  $K$  and  $K'$  points are called Dirac points<sup>32</sup>. The zero-band gap structure makes graphene unique compared to metal or semiconductor.

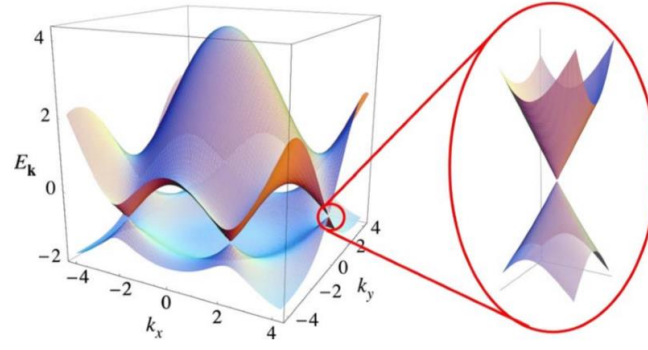


**Figure 1.1** Electronic band structure of graphene calculated by the tight-binding model. The right picture shows the linear dispersion close to the Dirac point. (From Ref. 32)

### 1.2.2 Electrical and optical property

Electric field tuning is a popular way to change the optical and electrical property of graphene by changing its carrier concentration. By applying a positive or negative gate voltage with a gating structure, the position of its Fermi level can be converted from the conduction band to the valence band<sup>33</sup>, as shown in Figure 1.2. At the same time, the resistance of graphene is changed, which is usually experimentally measured. The Fermi level of graphene is usually tuned to 0.4 eV for optical modulation<sup>34, 35</sup>.

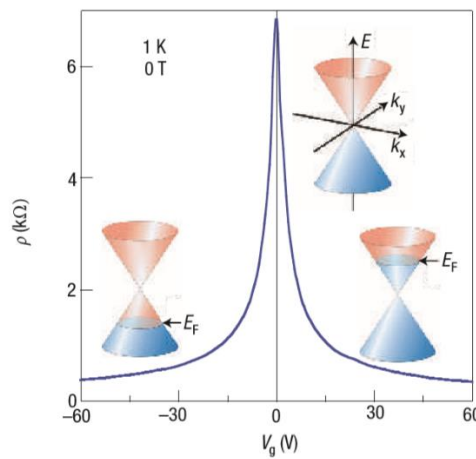


**Figure 1.2** Ambipolar electric field effect in graphene on Si/ 300 nm SiO<sub>2</sub>. Positive/negative gate voltage  $V_g$  induces electrons/holes in graphene, changing its resistivity. (From Ref. 33)

Figure 1.3a shows a piece of graphene on a SiO<sub>2</sub>(290 nm)/Si wafer I prepared with the traditional exfoliating method (see section 2.1.1 for the details of the method). The monolayer property is characterized by its Raman spectroscopy<sup>36</sup>, which shows a typical G peak at about 1580 cm<sup>-1</sup> and a 2D peak at about 2680 cm<sup>-1</sup> in Figure 1.3b. The intensity ratio I(2D)/I(G) is approximately 3. With the sharp 2D peak shape, the monolayer property of graphene is confirmed<sup>36</sup>. The exfoliated graphene here is measured to be p-doped, and its carrier mobility  $\mu$  is calculated to be 6090 cm<sup>2</sup>V<sup>-1</sup>s<sup>-1</sup> based on the model from Reference<sup>37</sup>.

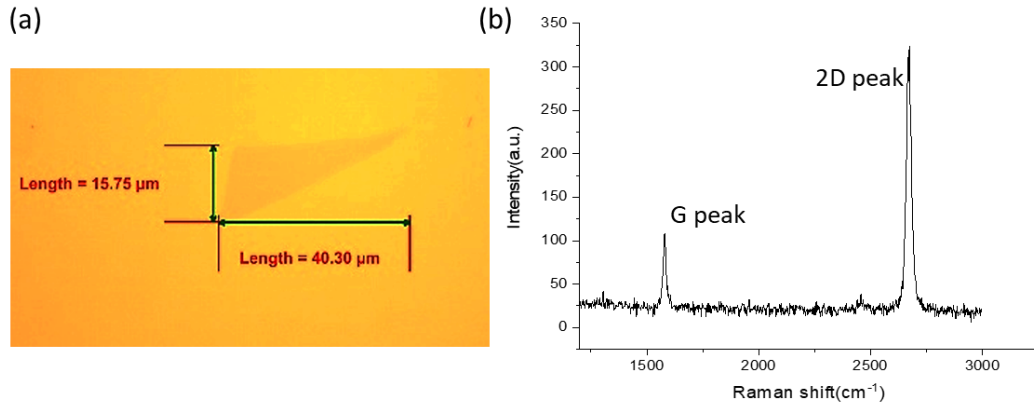


**Figure 1.3** (a) Microscope image of an exfoliated graphene on Si/290 nm SiO<sub>2</sub> wafer (b) The corresponding Raman spectroscopy of graphene ( $\lambda_{\text{exc}}=532$  nm), measured by Horiba XploRA PLUS Raman spectrometer.

For suspended graphene, the universal optical conductance  $G = \frac{e^2}{4h}$  was measured to hold from visible to the near-infrared range, which gives a constant light absorption of  $\pi\alpha \approx 2.3\%$  for graphene monolayer based on Fresnel's transmission equation in the thin-film limit<sup>38</sup>  $T = (1 + \frac{2\pi G}{c})^{-2}$ .

As mentioned in the first section, the Fermi level of graphene is tunable with a gate voltage. As a result, its light absorption can also be modulated, and many graphene optical modulators are based on this property. This can be explained by optical Pauli

blocking<sup>31, 34</sup>. With some doping of graphene, its Fermi level  $E_F$  is shifted to the conduction or valance band, and after the equilibrium of electron and hole distribution, the energy states between  $\pm E_F$  are filled, thus blocking the incoming electrons or holes (this consideration is valid for low temperatures). As a result, the interband transitions with photons' energy below  $|2E_F|$  will be prohibited. The Fermi level of graphene can be tuned up to 0.8 eV with a SiO<sub>2</sub> electrostatic gating structure<sup>39</sup> and 1 eV for with an electrolyte-based gating structure<sup>40</sup>. By changing the location of the Fermi level, we can control the light absorption of graphene. Figure 1.4 shows the Fermi level-dependent optical conductivity of graphene<sup>34</sup>, indicating the concept of Pauli blocking. Incident photons with an energy of 0.8 eV will be blocked for the case when  $E_F$  is 0.6 eV, leading to almost zero optical conductivity.

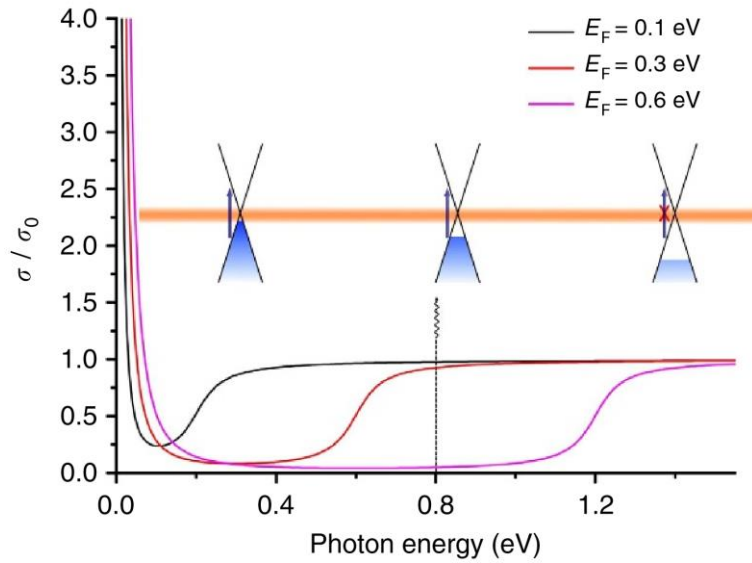


**Figure 1.4** Theoretical calculation of the optical conductivity of graphene at different Fermi energies 0.1 eV, 0.3 eV, and 0.6 eV. (From Ref. 34)

### 1.3 MoS<sub>2</sub>

The birth of graphene has aroused a huge interest in the research of 2D materials such as transition metal dichalcogenides (TMDs). Among them, MoS<sub>2</sub> is one of the most



studied. Bulk MoS<sub>2</sub> is widely used in dry lubricant<sup>41</sup>, catalysis<sup>42</sup>, and batteries<sup>43</sup>. Compared with its bulk form, monolayer MoS<sub>2</sub> has prompt applications in a new field of high-technology, which includes nano-circuits<sup>44</sup>, field-effect transistors<sup>45</sup>, and optoelectrics<sup>11, 46, 47</sup>. On the other hand, compared with graphene, MoS<sub>2</sub> is much more stable and uneasily oxidized by air, broadening its application field.

For bulk MoS<sub>2</sub>, each monolayer MoS<sub>2</sub> is held together by weak van der Waals forces, making it possible to produce monolayer through the mechanical exfoliation method. A monolayer MoS<sub>2</sub> is about 0.65 nm thick. The hexagonal planes of S and Mo atoms are bound together with a triangular prismatic arrangement through the ionic-covalent interaction<sup>22</sup>, as shown in Figure 1.5a. Bulk MoS<sub>2</sub> is an indirect bandgap semiconductor. However, when reducing the layer numbers of MoS<sub>2</sub> to one, its bandgap becomes direct.<sup>48, 49</sup> Figure 1.5b shows this transition as the number of layers decreases from bulk to monolayer. Besides, due to the spin-orbit band splitting between the valence band maxima and the conduction band minima, two prominent peaks, A (around 1.9 eV) and B (around 2 eV), usually appear in the absorption and photoluminescence spectrum for monolayer MoS<sub>2</sub> based devices.<sup>22, 49</sup>

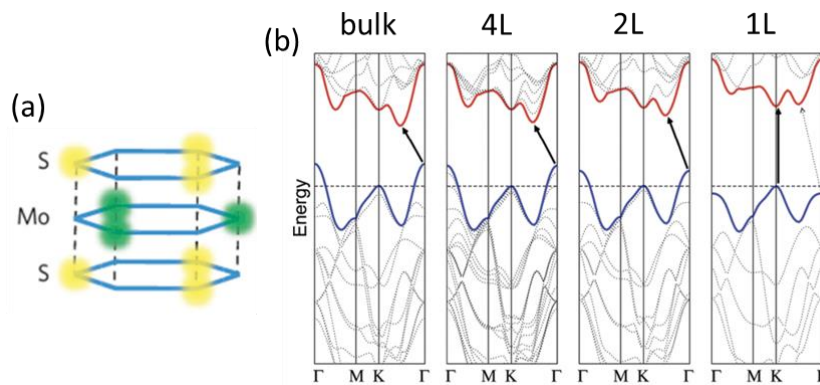


**Figure 1.5** (a) Atomic structure of monolayer MoS<sub>2</sub>. From Ref. 22 (b) Bandgap transition of MoS<sub>2</sub> from indirect to direct for different layer numbers: bulk, quadra-layer, bilayer, and monolayer. The black arrow indicates the lowest energy transition. Except for the bandgap

change from indirect to direct, the bandgap also enlarges when reducing layer numbers. This change leads to different physical properties for monolayer MoS<sub>2</sub> compared to the bulk one. From Ref. 49

Raman spectrum of monolayer MoS<sub>2</sub> usually depicts two typical peaks: E<sub>2g</sub><sup>1</sup> mode for the in-plane vibrational mode and A<sub>1g</sub> mode for the out-of-plane mode.<sup>50</sup> Figure 1.6b shows the Raman spectrum measured with 632.8 nm laser excitation for one of our monolayer MoS<sub>2</sub> devices. The spectrum exhibits two typical peaks at 386.7 cm<sup>-1</sup> and 403.4 cm<sup>-1</sup>, which corresponds to E<sub>2g</sub><sup>1</sup> and A<sub>1g</sub> mode separately. The position of the peaks is slightly shifted due to the gold substrate and 390 nm Si<sub>3</sub>N<sub>4</sub> dielectric layer, which is underneath monolayer MoS<sub>2</sub>.

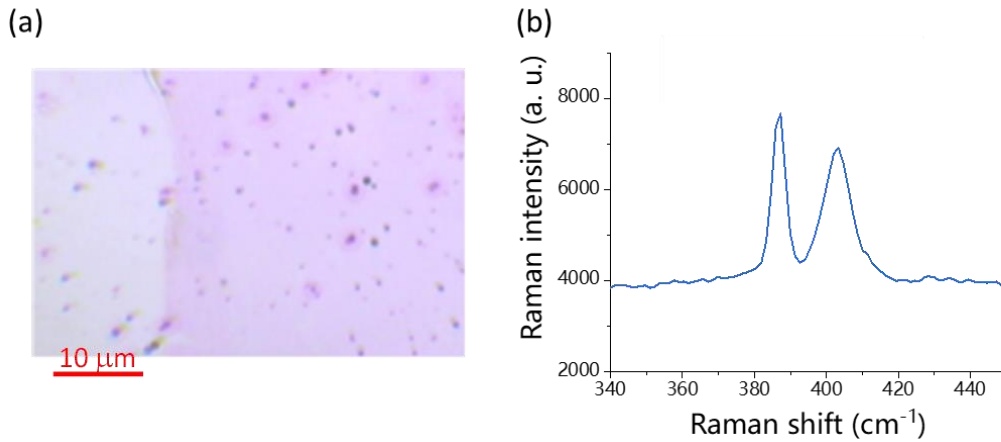


**Figure 1.6** (a) Optical microscopy image of a MoS<sub>2</sub> monolayer with Si<sub>3</sub>N<sub>4</sub> underneath. (b) Raman spectrum of the monolayer MoS<sub>2</sub> measured with a Witec spectrometer and 632.8 nm laser.

## 1.4 Electro-optical modulators

### 1.4.1 Basics of optical modulators

Optical modulation refers to the controlling of a light beam property where information is encoded. This can be achieved with a material whose optical properties can be

modulated. For example, in an electro-absorptive modulation, a periodic electric field could make a periodic output light intensity, then an electric signal is transferred to an optical signal.

In recent years, 2D materials have attracted increasing interest in the field of optical modulation. Despite the small size of 2D material, their optical properties could be easily and significantly modulated by tuning their carrier density, including graphene and transition metal dichalcogenides (TMDs).

In the process of optical communication, optical modulators are of crucial importance in converting the source information into an optical signal. Based on the modulation principle, optical modulators can be categorized as all-optical<sup>51</sup>, electro-optical<sup>52</sup>, thermo-optical<sup>53</sup>, acousto-optical<sup>54</sup>, magneto-optical<sup>55</sup>, mechanical-optical<sup>56</sup> modulators, with different types of modulation sources. Electro-optic modulation is one of the most developed, especially in the field of communications, which links the on-chip optical and electronic network components<sup>57</sup>. To clarify, this thesis focuses on electro-optical modulators (based on 2D material). For an electro-optical modulator, the modulation of a light beam is completed by controlling the modulation medium's reflection or absorption, primarily by changing its refractive index. For reflective modulators, the real part of the medium's refractive index is changed, which can be realized by Kerr effects<sup>58</sup> and Pockels effects<sup>59</sup>. For absorptive modulators, the imaginary part of the medium's refractive index (also called absorption coefficient) is changed, which can be realized by electro-absorption control and quantum-confined Stark effect<sup>60</sup>, etc.

A nanoscale optical modulator's performance can be evaluated by four performance metrics: operation wavelength range, modulation depth, modulation speed, and

insertion loss<sup>61</sup>. The operation wavelength range is the fundamental merit that directly decides the application of an optical modulator. A certain optical modulator usually works at a specific optical wavelength range based on the used modulation medium, which could vary from the ultraviolet to the visible<sup>62</sup>, infrared<sup>63</sup> (near-infrared, mid-infrared, and far-infrared), or even Tera-hertz band<sup>64</sup>. Therefore, depending on the needs, different optical modulators are chosen to work at different wavelength ranges. For example, optical fiber communication usually requires near-infrared optical modulators<sup>65</sup>. Modulation depth indicates the maximum change of the signal (either reflectance or transmittance) controlled by the external force. It is defined by the extinction ratio  $10 \times \log(T_{\max}/T_{\min})$  or  $10 \times \log(R_{\max}/R_{\min})$  for measuring transmittance and reflectance, respectively. A high modulation depth is commonly pursued with higher efficiency and less power-consuming when producing modulated signals. 4-5 dB is usually enough for normal communication applications<sup>2, 19, 61</sup>. Insertion loss refers to the power drop of the optical signal after passing through the optical modulator<sup>66</sup>. Modulation speed depends on the modulation medium's responsivity and the structure (e.g., time constant for an RC circuit). A faster modulation speed is usually preferred, especially for a data transmitting system, which also determines its operation bandwidth<sup>19, 61</sup>. Energy consumption is also an important performance parameter for optical modulators, which is related to the modulation efficiency and the loss. Low energy consumption is always preferred. Due to the research interest and experimental conditions, modulation speed and energy consumption of our optical modulators have not been studied and covered in this thesis.

#### **1.4.2 Electro-optical modulators based on 2D material**

An optical modulator's essence is the modulation medium whose optical property can be modulated by the external force. Compared with traditional bulk semiconductors for

optical modulation, 2D materials mainly possess three promising properties. First, 2D materials own numerous mechanical advantages. Except for the ultrasmall atomic layer thickness that can further minimize optical modulators' size, many of them hold good mechanical flexibility, robustness, and compatibility to other optical structures such as waveguides and fibers<sup>5, 67</sup>, which is needed for current complementary metal-oxide-semiconductor (CMOS) technology. Besides, stacks of 2D materials can be fabricated, which often offer unique properties<sup>68</sup>. Second, the optical properties of 2D materials could be easily and significantly modulated by electrical field<sup>10</sup> or chemical doping<sup>11</sup>, including graphene and transition metal dichalcogenides. For electro-optical modulation, this can be easily achieved by changing their Fermi level with an electrical gating. Optical Pauli blocking is an important factor where the energy state below the Fermi level is fully occupied. In this case, for the photons with energy below  $2E_f$ , the interband transition is forbidden<sup>12</sup>. Third, 2D materials have unique optical responses and spectral ranges. For graphene, it only absorbs 2.3% of the incident light but over a visible and near-infrared wide spectral range. In total, the optical response spectrum of current 2D materials has covered from ultraviolet to terahertz and even microwave regions, owing to their diverse electronic structures<sup>69</sup>.

Electro-optical control of the optical properties of 2D materials is relatively convenient than other means such as chemical doping, due to the strong confinements of the electrons in 2D materials, making a tunable band structure sensitive to the external electrical field. Most optical modulators are based on electro-optic effects in 2D materials, which a widely-used gating structure can easily realize. As a result, the refractive index of graphene can be controllable. Although experimental electro-refractive modulation in graphene has been reported<sup>70, 71</sup>, most of the current graphene modulators are based on its gate-tunable electro-absorption<sup>16, 72-76</sup>. Electro-optical

modulation based on 2D TMD materials (bandgap ranging from 1 to 2.5 eV) has also been reported, including MoS<sub>2</sub><sup>22</sup>, WS<sub>2</sub><sup>77</sup>, MoTe<sub>2</sub><sup>78</sup>. Compared to graphene, TMDs have relatively low carrier mobility at the level of 100 cm<sup>2</sup>V<sup>-1</sup>s<sup>-1</sup> at room temperature<sup>79, 80</sup>, though the theoretical value is much higher<sup>81, 82</sup>. However, compared to graphene, they have a much larger optical absorption, reaching ~10% level<sup>83</sup>.

On the other hand, due to the atomic layer property for graphene and monolayer MoS<sub>2</sub>, its optical absorption is relatively small, which leads to low modulation depth. For graphene with a 2.3% absorption, the modulation depth using graphene under normal illumination with no enhancement will be only 2.3%. Therefore, current electro-optical modulators with 2D material commonly need to be combined with designed structures to enhance the low absorption of 2D material<sup>16, 25, 34, 62, 74, 84</sup>. In recent years, another emerging material, black phosphorus (phosphorene for monolayer), has been studied for electro-optical modulation<sup>85, 86</sup>, which fills the gap between zero-gap graphene and large-gap TMDs with an unusual anisotropic optical absorption and photoluminescence<sup>87</sup>.

## **1.5 Surface plasmon polaritons (SPPs)**

### **1.5.1 Developments of plasmonics**

Utilizing nanoparticles to control the reflection and transmission of light can date back to the fourth century AD when the Lycurgus cup<sup>88</sup> (see Figure 1.7) was made, although this cup's production was possibly an accident at that time. It was not until the 20th century that the properties of nanoparticles were quantized and analyzed. In 1908, Mie developed his theory to explain the scattering of light with metallic nanoparticles, which started the research of nanoscale optics<sup>89</sup>. In 1902, R. M. Wood found the abnormal phenomenon in his metal grating diffraction experiment, where new diffraction peaks

appeared in the reflection spectrum<sup>90</sup>. Rayleigh tried to explain this phenomenon by his diffraction theory in 1907 and thought that the abnormality happens when the diffraction wave matches the grating's surface<sup>91</sup>, which could well explain most of Wood's experimental results. Later in 1941, U. Fano added a supplementary explanation to Rayleigh's theory with "a forced resonance"<sup>92</sup> based on the theory of electromagnetic surface wave proposed by Zenneck<sup>93</sup> and Sommerfeld<sup>94</sup>. He believed abnormal peaks in the diffraction spectrum are the coupling results between the diffraction mode and the metal surface waves. The word plasmon was coined by Pines<sup>95</sup> in 1956 to describe the quantization of the collective oscillation of free electrons in a study of electrons with high energy passing through metals, just as a photon is the quantization of lattice vibration. Powell and Swan firstly observed surface plasmons (SPs) in the energy-loss experiments in 1959<sup>96</sup>. One year later, in 1960, Stren and Farrel<sup>97</sup> further investigated the resonance conditions of this surface mode, confirming Ritchie's theory through their experiments. In 1968, Ritchie discussed the connection and similarity between the resonant surface waves in Wood anomaly and surface plasmons in energy loss experiments of electrons bombarding thin metal films<sup>98</sup>. At the same time, Otto<sup>99</sup>, Kretschmann and Reather<sup>100</sup> firstly observed the excitation of surface plasmons in metal films with visible light by prism coupling, making it much easier to study the property of surface plasmons. Kreibig and Zacharia<sup>101</sup> found that the light absorption and scattering by metallic nanoparticles can be explained by its surface plasmon resonances in 1970. It is in 1974 when the term surface plasmon polaritons (SPPs) was used by Cunningham<sup>102</sup> to describe surface plasmons modes on the metal surface. In 1982, Boardman published a book concluding the development of surface plasmons where it is comprehensively analyzed as electromagnetic surface modes<sup>103</sup>. After that, the theory and applications of surface plasmons got gradually developed.

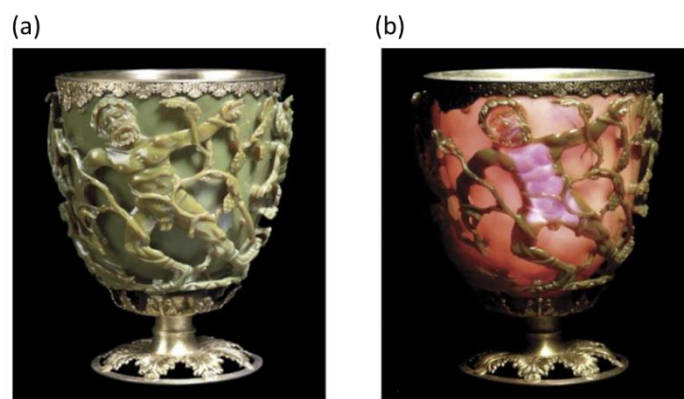


**Figure 1.7** Different colors resulted from the interaction of light and metal nanoparticles in the Lycurgus cup. (a) When the light emits from the outside, the glass presents jade green (b) When light shines from the inside, the glass presents ruby-red. From Ref. 88

In 1997, Nie made the first measurement of the Raman spectrum of single-molecule, which was proved to be the result of electromagnetic field enhancement<sup>101</sup> due to surface plasmons by Van Duyne, starting the application of surface-enhanced Raman spectroscopy (SERS)<sup>104</sup>. In 1998, Ebbesen discovered the enhanced transmission through hole arrays caused by surface plasmon resonance<sup>105</sup>. These two phenomena attracted immense interest into the field of surface plasmons. In the late 1990s, advanced nano-processing technology and electromagnetic simulation accelerated the development of surface plasmons. By fabricating nano-optical waveguides with nanolithography, light propagation can be limited in sub-wavelength size with the help of SPPs, which is predicted to be the next-generation chip technology. Under this circumstance, the term—plasmonics was created and became a research spot<sup>28, 106</sup>. In 2006, Stefan Maier<sup>107</sup> published the book "Plasmonics: Fundamentals and Applications" which gives a thorough introduction to the field of plasmonics and its developments and applications, including biosensing<sup>108</sup> and optoelectronics<sup>109</sup>.

More recently, along with the discovery of 2D material, integrated plasmonic structures with 2D material have been studied for electro-optics<sup>25, 34, 110</sup>. In chapter 4, we will



describe a plasmonic waveguide structure for on-chip optical modulation with a gate-controlled graphene stripe, which shows appreciable performance and could be used in nanoscale integrated circuits. Furthermore, we achieved a nanometer-scale control of the light field in our plasmonic waveguide device.

### 1.5.2 Maxwell's equations and Drude model for metals

Maxwell's equations in the matter are as follows:

$$\nabla \cdot \mathbf{D} = \rho_{\text{ext}} \quad (1.5a)$$

$$\nabla \cdot \mathbf{B} = 0 \quad (1.5b)$$

$$\nabla \times \mathbf{E} = -\frac{\partial \mathbf{B}}{\partial t} \quad (1.5c)$$

$$\nabla \times \mathbf{H} = \mathbf{j}_{\text{ext}} + \frac{\partial \mathbf{D}}{\partial t} \quad (1.5d)$$

where  $\mathbf{D}$  (unit:  $\text{C} \cdot \text{m}^{-2}$ ) is the electric displacement field,  $\mathbf{B}$  (unit: T) is the magnetic flux,  $\mathbf{E}$  ( $\text{V} \cdot \text{m}^{-1}$ ) and  $\mathbf{H}$  (unit:  $\text{A} \cdot \text{m}^{-1}$ ) refer to the electric and magnetic field respectively.  $\rho_{\text{ext}}$  (unit:  $\text{C} \cdot \text{m}^{-3}$ ) and  $\mathbf{j}_{\text{ext}}$  (unit:  $\text{A} \cdot \text{m}^{-2}$ ) are the external charge and current, respectively. The additional relations can be written as follows:

$$\mathbf{D} = \varepsilon_0 \mathbf{E} + \mathbf{P} \quad (1.6)$$

$$\mathbf{H} = \frac{1}{\mu_0} \mathbf{B} - \frac{\partial \mathbf{D}}{\partial t} \quad (1.7)$$

where  $\varepsilon_0 = 8.854 \times 10^{-12} \text{ F} \cdot \text{m}^{-1}$  is the electric permittivity of free space and  $\mu_0 = 4\pi \times 10^{-7} \text{ N} \cdot \text{A}^{-2}$  is the magnetic permeability of free space.  $\mathbf{P}$  and  $\mathbf{M}$  represent polarization and magnetization, respectively. For a linear and isotropic material, we have

$$\mathbf{D} = \varepsilon \mathbf{E} = \varepsilon_0 \varepsilon_r \mathbf{E} \quad (1.8)$$

$$\mathbf{H} = \frac{1}{\mu} \mathbf{B} = \frac{1}{\mu_0 \mu_r} \mathbf{B} \quad (1.9)$$

$\epsilon_r$  and  $\mu_r$  are relative electric permittivity and relative magnetic permeability. For nonmagnetic media,  $\mu_r = 1$ .

The oscillation of electrons in metal with a driving external electric field can be described with the following Drude model, where metal is considered as a collection of fixed positively charged ions with detached electrons surrounded.

$$\dot{\mathbf{p}} + \gamma \mathbf{p} = -e\mathbf{E} \quad (1.10)$$

$\mathbf{p}$  is the average momentum per electron,  $\gamma$  is the characteristic frequency of the collisions (elastic collisions between electrons and electrons, inelastic collisions between electrons and defects/phonons), which is defined by  $\gamma = 1/\tau$  and  $\tau$  is the relaxation time of the free electron gas (usually the order of  $10^{-14}$  s at room temperature), and  $e=1.602 \times 10^{-19}$  C is the elementary charge of an electron. As  $\mathbf{p} = m\mathbf{v} = m\dot{\mathbf{x}}$ , equation 1.10 could be written as

$$m\ddot{\mathbf{x}} + m\gamma\dot{\mathbf{x}} = -e\mathbf{E} \quad (1.11)$$

$\mathbf{x}$  is the displacements of electrons from the ions. Trying a solution  $\mathbf{x} = \mathbf{x}_0 e^{-i\omega t}$  for a harmonic electrical field  $\mathbf{E} = \mathbf{E}_0 e^{-i\omega t}$  yields

$$\mathbf{x} = \frac{e}{m} \frac{1}{\omega^2 + i\gamma\omega} \mathbf{E} \quad (1.11)$$

The macroscopic polarization induced by the displacement of the electrons by the electric field is

$$\mathbf{P} = -Nex = \epsilon_0(\epsilon_r - 1)\mathbf{E} \quad (1.12)$$

Considering formulas 1.11 and 1.12, we can get the dielectric function of the metal as equation 1.13, where a plasma frequency  $\omega_p = \sqrt{\frac{Ne^2}{m\epsilon_0}}$  of the electron gas in metals is introduced.

$$\epsilon_r = \epsilon_1 + i\epsilon_2 = 1 - \frac{\omega_p^2}{\omega(\omega + i\gamma)} \quad (1.13)$$

When the damping of electrons is negligible,  $\gamma = 0$ , the dielectric function becomes

$$\epsilon_r = 1 - \frac{\omega_p^2}{\omega^2}. \quad (1.14)$$

A more accurate equation is given with equation 1.15, where  $1 \leq \epsilon_\infty \leq 10$ , describing the contribution from the positive ion cores polarization in the external electrical field.

$$\epsilon_r = \epsilon_\infty - \frac{\omega_p^2}{\omega(\omega + i\gamma)}, \quad (1.15)$$

The Drude model can be improved at high frequencies where interband transitions should be considered, especially at the visible range for noble metals. A Drude-Lorentz model will be much more useful when describing the electron response of metals. In our situation of the telecom (near-infrared) range, the Drude model provides a good description of the metals' optical responses. We mainly focus on the situation where  $\omega < \omega_p$  and  $\text{Re}(\epsilon_r) < 0$ , and SPPs could exist at the interface of metal and dielectric at this time.

### 1.5.3 Surface plasmon polaritons (SPPs) and its waveguides

When the light wave is incident on the interface between the metal and dielectric, the free electrons at the metal surface vibrate collectively. At some conditions, the electromagnetic wave and the plasmon (quantization of the collective oscillation of free

electrons) on the metal surface are coupled to form a new surface mode called surface plasmons (SPs). Surface plasmons can be divided further into surface plasmon polaritons (SPPs) and localized surface plasmons (LSPs, usually related with metal nanoparticles and not studied in this thesis)<sup>107</sup>. SPPs is a propagating mode along the planar interface between a metal and a dielectric medium. It can be excited by both light and electron with proper initial parameters. Being an electromagnetic wave, SPPs satisfies Maxwell's equations, from which their properties can be defined. Compared to current optical devices restricted within the diffraction limit, SPPs contains unique properties such as subwavelength scale, strong field enhancement, and a high degree of tunability controlled by certain plasmonic material and structures<sup>111, 112</sup>, offering new opportunities for chip-based optical nano-devices. Since SPPs is the propagating wave at the interface of metal and dielectric,  $\mathbf{j}_{\text{ext}} = 0$  and  $\rho_{\text{ext}} = 0$  in this case. From equations 1.5c and d, we have

$$\nabla \times (\nabla \times \mathbf{E}) = \nabla \times \left( -\frac{\partial \mathbf{B}}{\partial t} \right) = -\frac{\partial (\nabla \times \mathbf{B})}{\partial t} = -\frac{\partial (\nabla \times \mu \mathbf{H})}{\partial t} = -\mu \frac{\partial^2 \mathbf{D}}{\partial t^2} = -\mu \epsilon \frac{\partial^2 \mathbf{E}}{\partial t^2}$$

Consider  $\nabla \times (\nabla \times \mathbf{E}) = \nabla(\nabla \cdot \mathbf{E}) - \nabla^2 \mathbf{E} = -\nabla^2 \mathbf{E}$ , by noting from equation 1.5a that  $\nabla \cdot \mathbf{E} = 0$ , we can obtain equation 1.15. Equation 1.16 can be derivated with the same method.

$$\nabla^2 \mathbf{E} = \mu \epsilon \frac{\partial^2 \mathbf{E}}{\partial t^2} \quad (1.15)$$

$$\nabla^2 \mathbf{B} = \mu \epsilon \frac{\partial^2 \mathbf{B}}{\partial t^2} \quad (1.16)$$

The solutions of equation 1.15 and 1.16 would be

$$\mathbf{E} = \mathbf{E}_0 e^{i(\mathbf{k} \cdot \mathbf{r} - \omega t)} \quad (1.17)$$

$$\mathbf{B} = \mathbf{B}_0 e^{i(\mathbf{k} \cdot \mathbf{r} - \omega t)} \quad (1.18)$$

and the propagating speed of light in the medium can be defined as  $c = \frac{1}{\sqrt{\mu\epsilon}}$ .

Suppose the position of the interface is  $z = 0$ . For  $z > 0$ , we have a dielectric layer with a dielectric function  $\epsilon_1$ . For  $z < 0$ , we have a metal with a dielectric function  $\epsilon_2$ . The electric field and magnetic field are expressed as  $\mathbf{E}_1$  and  $\mathbf{H}_1$  in the dielectric;  $\mathbf{E}_2$  and  $\mathbf{H}_2$  in the metal separately. We consider only transverse magnetic (TM, p-polarised) wave in this case because the transverse electric (TE, s-polarised) wave cannot excite surface modes, which can be proved by boundary conditions analysis. For the TM wave,  $\mathbf{E}_y = 0$  and  $\mathbf{H}_x = \mathbf{H}_z = 0$ . The rest of the components in the metal and dielectric are defined from equations 1.19 to 1.22.

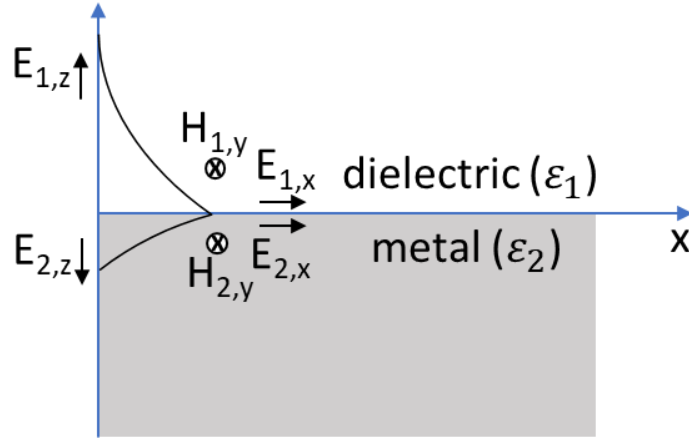


**Figure 1.8** The boundary of dielectric and metal for surface plasmon polariton.

$$\mathbf{E}_1 = \begin{pmatrix} E_{1,x} \\ 0 \\ E_{1,z} \end{pmatrix} e^{i(k_{1,x}x + k_{1,z}z - \omega t)} \quad (1.19)$$

$$\mathbf{H}_1 = \begin{pmatrix} 0 \\ H_{1,y} \\ 0 \end{pmatrix} e^{i(k_{1,x}x + k_{1,z}z - \omega t)} \quad (1.20)$$

$$\mathbf{E}_2 = \begin{pmatrix} E_{2,x} \\ 0 \\ E_{2,z} \end{pmatrix} e^{i(k_{2,x}x + k_{2,z}z - \omega t)} \quad (1.21)$$

$$\mathbf{H}_2 = \begin{pmatrix} 0 \\ H_{2,y} \\ 0 \end{pmatrix} e^{i(k_{2,x}x + k_{2,z}z - \omega t)} \quad (1.22)$$

From the boundary conditions,

$$E_{1,x} = E_{2,x} = E_x \quad (1.23)$$

$$H_{1,y} = H_{2,y} = H_y \quad (1.24)$$

$$D_{1,z} = D_{2,z} \quad (1.25)$$

Consider Maxwell equation 1.5d, we have

$$\nabla \times \mathbf{H}_1 = \frac{\partial \mathbf{D}_1}{\partial t} = \epsilon_1 \frac{\partial \mathbf{E}_1}{\partial t} \quad (1.26)$$

Combined equation 1.26 with equation 1.19 and 1.20, we have

$$\begin{pmatrix} -\frac{\partial H_{1,y}}{\partial z} \\ 0 \\ \frac{\partial H_{1,y}}{\partial x} \end{pmatrix} = -i\omega\epsilon_1 \begin{pmatrix} E_{1,x} \\ 0 \\ E_{1,z} \end{pmatrix}$$

Thus,

$$k_{1,z}H_{1,y} = i\omega\epsilon_1 E_{1,x} \quad (1.27)$$

$$k_{2,z}H_{2,y} = -i\omega\epsilon_2 E_{2,x} \quad (1.28)$$

Consider equations 1.23 and 1.24, and we arrive at the relationship of the dielectric function of metal and dielectric.

$$k_x = k_{1,x} = k_{2,x} \quad (1.29)$$

$$\frac{k_{1,z}}{k_{2,z}} = -\frac{\epsilon_1}{\epsilon_2} \quad (1.30)$$

Note that the real part of the dielectric function of two media should have opposite signs for surface plasmon polaritons (SPPs) at the interface, such as the case of metal and air.

On the other hand, through equation 1.15, we can obtain the dispersion relation for the TM wave in nonmagnetic material ( $\mu = 1$ ).

$$k_{1,x}^2 + k_{1,z}^2 = \epsilon_1 \frac{\omega^2}{c^2} \quad (1.31)$$

$$k_{2,x}^2 + k_{2,z}^2 = \epsilon_2 \frac{\omega^2}{c^2} \quad (1.32)$$

Considering formula 1.29, we can get the dispersion relation.

$$k_{sp} = k_x = \frac{\omega}{c} \sqrt{\frac{\epsilon_1 \epsilon_2}{\epsilon_1 + \epsilon_2}} \quad (1.33)$$

$$k_{1,z} = \frac{\omega}{c} \sqrt{\frac{\epsilon_1^2}{\epsilon_1 + \epsilon_2}} \quad (1.34)$$

$$k_{2,z} = \frac{\omega}{c} \sqrt{\frac{\epsilon_2^2}{\epsilon_1 + \epsilon_2}} \quad (1.35)$$

From the Drude model, when  $\omega < \omega_p$ ,  $\epsilon_2(\omega) < 0$ . When  $\text{Re}(\epsilon_2) < -\epsilon_1 < 0$ ,  $\text{Re}(k_{sp}) > \frac{\omega}{c} \sqrt{\epsilon_1}$ ,  $k_{1,z}$  and  $k_{2,z}$  are both imaginary. A new electromagnetic mode (SPPs) is restricted at the metal and dielectric interface, which is lossy (Ohmic losses) at the z-direction in both metal and dielectric. Figure 1.9 shows the dispersion relation for SPPs and photons for contrast. SPPs has a larger wave vector and shorter wavelength, which leads to stronger spatial constraint and higher local intensity. On the other hand, the mismatch between the wavevectors SPPs and photons reveals that SPPs

cannot be excited directly by photons from free space. Therefore, special methods need to be used to excite SPPs, such as prism coupling<sup>100</sup>, grating coupling<sup>113</sup>, highly focused optical beam excitation<sup>114, 115</sup>, near-field excitation with a tip<sup>111</sup>, and electron beam excitation<sup>116</sup>.

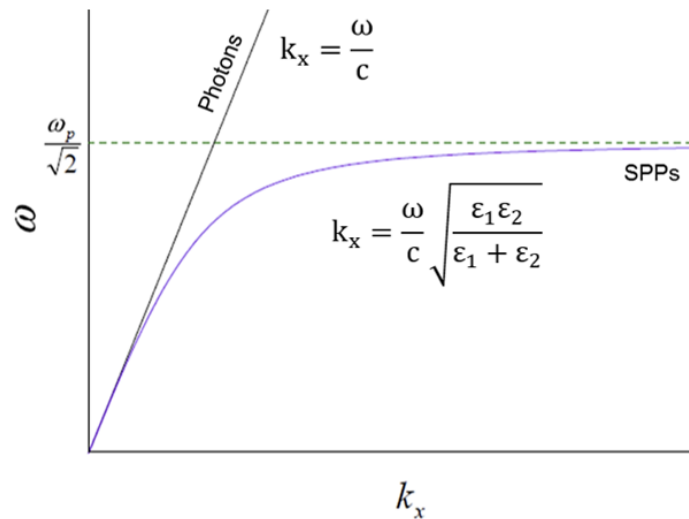


**Figure 1.9** The dispersion relations for surface plasmon polaritons (SPPs) and free-space photons.

Compared to current optical devices which are restricted by the diffraction limit, SPPs can reach subwavelength scale due to the confinement to the metal-dielectric interface, which offers new opportunities to miniaturize the chip-based technology. Furthermore, the unique optical property of SPPs propagating at the interface between metals and dielectrics inspires the development of plasmonic waveguide devices. Various structural plasmonic waveguides have been proposed, including nanoparticle chain<sup>117</sup>, metal stripes<sup>118</sup>, and gap/slot/groove channel waveguides<sup>114, 119, 120</sup>. Compared to traditional dielectric waveguides such as fiber waveguide, the most significant advantage of SPPs waveguide is the subwavelength spatial confinement of the wave energy. However, the propagation length decreased accordingly due to the loss in



metals. Therefore, there is usually a trade-off between the propagation length and the mode confinement in practice<sup>121</sup>.

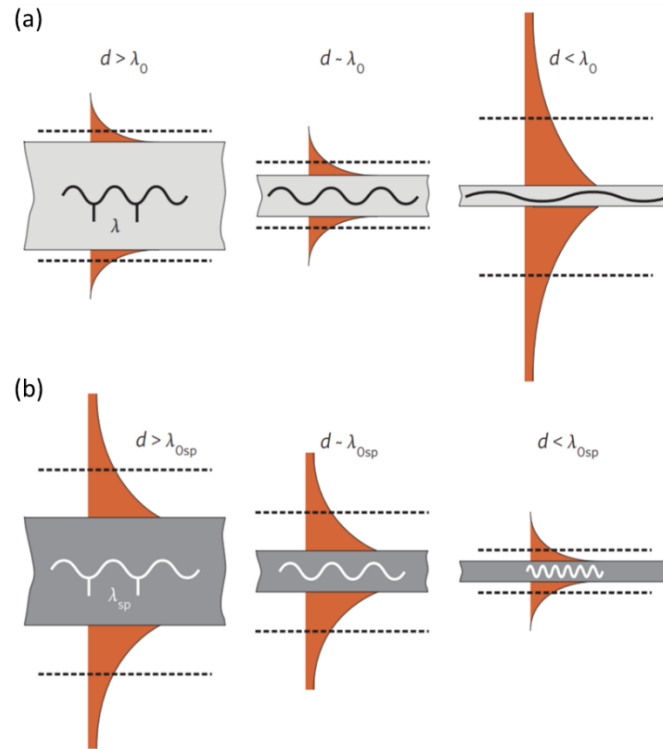


**Figure 1.10** Field distribution of the fundamental waveguide mode in a cylindrical (a) dielectric fiber and (b) metal nanowire with reducing diameters.  $\lambda_0$  and  $\lambda_{0sp}$  are the waveguide mode wavelength in bulk fiber dielectric and metal, respectively (infinite diameters). Dashed lines represent the size of the fields (1/e level). (From Ref. 106)

Figures 1.10a, b compares the waveguide modes in dielectric fibers and metal wires<sup>106</sup>. The fundamental waveguide mode penetrates into the medium surrounded when reducing the diameter of the dielectric, becoming a bulk plane wave when the diameter is close to zero. Hence, decreasing the diameter smaller to the subwavelength scale will reversely increase the mode size, limiting the miniaturization of optical devices. However, for a metal waveguided SPPs mode, the situation is entirely inverted. The reduced diameter of the (cylindrical) metal nanowire leads to strong localization of the waveguide mode at the metal and dielectric interface when the diameter is smaller than

the wavelength. Therefore, the dimensional size of the SPPs mode can reach subwavelength-scale, even a few nanometers, which brings the possibility for nano-optical devices. Different from the (insulator-metal-insulator) IMI waveguide structure shown in Figure 1.10b, another typical gap surface plasmon (GSP) waveguide with a metal-insulator-metal (MIM) structure will be illustrated in Chapter 4, where it is used for optical modulation and detection by interacting with graphene.

# Chapter 2

## Methods and techniques

*Lithography is a key technique in the nanoscale manufacturing industry with a resolution to a few nanometers<sup>122</sup>. This chapter mainly introduces the experimental method and techniques I have used for our researches, either for fabrication or measurements. The fabrication procedure (section 2.1) is introduced through a complete process of a simple graphene device (with no measurements on it), mainly consisting of the lithography process (optical and electron beam lithography). All nano-devices with much more complicated structures in Chapters 3 to 5 were made with a similar but repetitive process. The following section 2.2 then describes all the techniques I have used in this project for characterization of the samples and devices, whose background information is necessary to be displayed here for a better understanding of the discussed results in the following chapters.*

### 2.1 Fabrication

#### 2.1.1 Sample preparation: mechanical cleavage or wet transfer

2D materials for optical devices can be produced by mechanical exfoliation or by a chemical vapor deposition method. Taking graphene as an example, for the exfoliation method, a small piece of bulk graphite was first adhered to a tape by simply pressing the tape on graphite and peeling off. The tape is then folded and unfolded repeatedly until a number of graphite pieces are distributed widely on the tape. Then we pressed this tape (graphite underneath) evenly and tightly on the prepared substrate to make a strong adherence between graphene and the substrate so that the graphene piece can be

left on it when we finally remove this tape from the substrate, gently and slowly starting from the corner. For SiO<sub>2</sub> substrates used in our experiments, O<sub>2</sub>/Ar plasma etching was used on the substrate to remove the hydrocarbon contaminants on the surface, thus help with the production of “large” graphene but with a cost of degraded mobility<sup>123, 124</sup>.

Chemical vapor deposition (CVD) technology uses vapor (containing carbon compounds) deposition to produce graphene on the substrate surface by chemical reaction, which is the most effective method to produce graphene in industry. CVD method is beneficial for massive production, but the quality of graphene is not as good as the exfoliated one. For a standard CVD process, a copper film is placed in a sealed quartz tube and annealed at 1000°C for 30 minutes, with an H<sub>2</sub> flow at a rate of 20 cm<sup>3</sup>/min and a pressure of 200 mTorr. A CH<sub>4</sub> gas flow is then introduced into the chamber with a 40 cm<sup>3</sup>/min flow rate for 30 mins to perform the chemical deposition process at a pressure of 600 mTorr. C-H bonds break at high temperatures, and new C-C bonds form at the surface of the copper film to produce graphene. Finally, the chamber is cooled to room temperature in the H<sub>2</sub> atmosphere, and the CVD process is completed. For CVD graphene, we used the wet transfer method to prepare our samples.

Copper-based CVD graphene contains monolayer graphene on both sides of the copper. Hence, we used O<sub>2</sub>/Ar plasma etching first to remove graphene at one side of the copper film. Then, a layer of 8% 950K PMMA was spin-coated on the CVD graphene of the other side with copper foil underneath (spin speed 4000 rpm for one minute and then baked at around 170°C for 3 minutes). Then, we cut a small piece with a scissor and put it in the 25 g/L ammonium persulfate solution for 12 hours to etch the copper underneath. The size of graphene was approximately 1×1 cm<sup>2</sup> which is enough for our hybrid graphene devices. The floating membrane was then moved to the deionized water with a clean and smooth Si wafer to remove the ammonium persulfate residue.

The same process could be repeated several times to remove the residue deeply. Finally, the PMMA/graphene membrane was fished with a desired target substrate with graphene adhered to its surface.

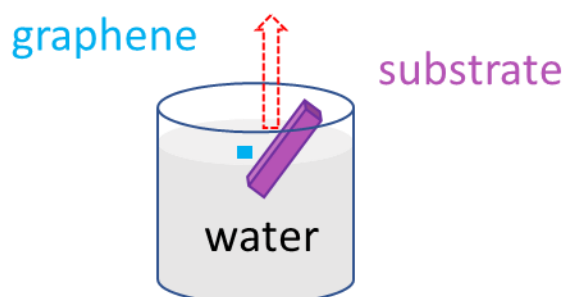


**Figure 2.1** Schematic of fishing graphene with the substrate

After that, it was left to dry for 24 hours, and after drying, the whole device was baked on a hot plate at 170°C for 15 minutes (further improving adhesion between graphene and substrate). Finally, the whole sample was bathed in acetone for 10 minutes to clean the PMMA. Then, it was put in isopropanol solvent (IPA) for 10 minutes to clean residual acetone and dried with an N<sub>2</sub> gun at last. After all these processes, a piece of CVD graphene was left on the substrate, and we used optical microscopy to inspect its quality and find suitable areas for the fabrication of the next step.

Figure 2.2 shows a typical example of exfoliated graphene fabricated on a 290 nm SiO<sub>2</sub>/Si wafer that I prepared. The exfoliated graphene's monolayer property can be checked directly by the contrast of the microscope image. To confirm the monolayer property, Raman spectroscopy, optical measurements with spectrometer or ellipsometer were used. It is worth noting again that the quality of an exfoliated graphene was usually better than the CVD one, with higher carrier mobility and fewer defects. However, its size and shape were uncontrollable, with a lateral length smaller than hundreds of micrometers<sup>125, 126</sup>, which is unreal for industrial applications. Sections 2.1.2 to 2.1.4

illustrate the fabrication procedure with this graphene sample. Although the final device is not helpful for my research, it gives a detailed picture of the lithography process for fabricating nanodevices.



**Figure 2.2** Optical image of a large piece of exfoliated graphene on a 290 nm SiO<sub>2</sub>/Si wafer with a 65  $\mu\text{m}$  lateral length. The color of the image depends on the filter of the microscope to give the best contrast<sup>127</sup>.

### 2.1.2 Photolithography and Patterning

Photolithography was used in our work to make a pattern on the graphene sample. First, a PMGI layer was spun on the substrate for 60 s with a speed of 4000 rpm and baked for 10 min at 160°C to 180°C. Then, photoresist Shipley S1805 was spun on the substrate for 60 s with a speed of 4000 rpm and then baked for 1 min at 110°C. A laser-writer (Microtech LW-405) was then used to expose the designed pattern on the photoresist at a power around 230 mJ/cm<sup>2</sup>. Then the exposed area was placed in an MF319 developer for 1 min. The exact development time depends on the laser power and resists types. A dose test before the final exposure was usually necessary. Finally,

we cleaned the sample with deionized water and dried it with N<sub>2</sub> gas. The developed sample is shown in Figure 2.3.



**Figure 2.3** Optical image of the sample after the exposure and development. The grey area is still covered with the undeveloped photoresist.

After the exposure, the designed area was protected by the photoresist. Then, we could remove the unneeded graphene (not covered by the photoresist) with an Ar/O<sub>2</sub> plasma etching for 5 min. O<sub>2</sub> plasma breaks the C-C bonding of the unprotected graphene and removes it from the surface by chemical reaction<sup>128</sup>. Figure 2.4 shows the sample after the plasma etching.

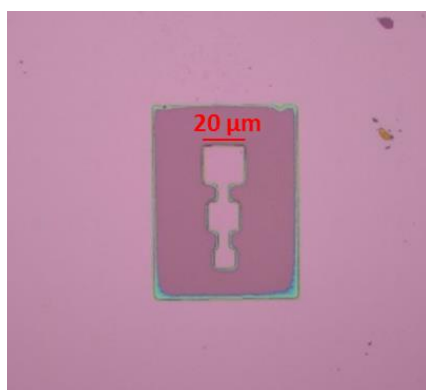


**Figure 2.4** Optical image of the sample after etching by Ar/O<sub>2</sub> plasma (Graphene not covered by resist has been removed.)

Part of the resist was also removed by oxygen plasma etching, but it was still thick enough to protect the patterned graphene underneath. After the plasma etching, the

remained photoresist was resolved by acetone and then cleaned with isopropanol solvent (IPA) to remove the residual acetone. The patterned graphene sample is shown in Figure 2.5, which consists of three squares of different sizes.

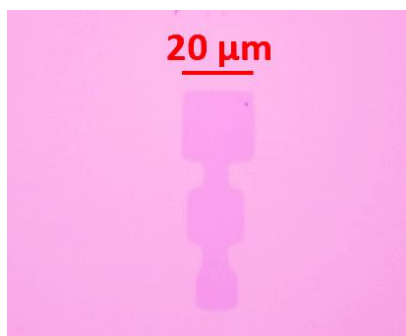


**Figure 2.5** Optical image of the patterned graphene on a 290 nm SiO<sub>2</sub>/Si wafer.

### **2.1.3 Electron beam lithography**

After the graphene pattern was obtained, designed structures can be added to the sample for research interest. For this device, thin metal contacts were connected to the graphene sample for electrical measurements. Photolithography (5 μm resolution for Microtech LW-405 laser writer) is suitable for large-area exposure to make the large graphene pattern. To make the thin contacts pattern, e-beam lithography with 100 nm resolution was used here, which is more precise and time-consuming. In this case, PMMA (3% concentrate) was first spun on the sample for 60 s with a speed of 3000 rpm and then baked for 10 minutes at 170°C, which gave a final thickness around 210 nm. Then we used a 10 kV electron beam (Zeiss EVO MA10 electron) for the exposure process. A higher energy of the electron beam gives a higher resolution. For e-beam lithography, a pattern of masks and coordinates is usually made first to help locate the sample. After the exposure, the sample was developed in MIBK: IPA (1:3) for 40 s at room temperature and then IPA for 1 min, where the solvent removed the exposed PMMA.



Finally, we cleaned the samples with deionized water and dried them with an N<sub>2</sub> gun, which gave the typical contact pattern shown in Figure 2.6.

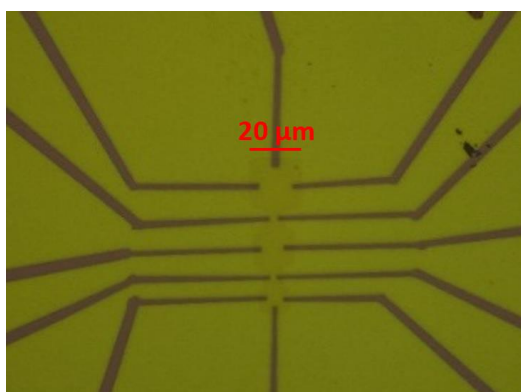


**Figure 2.6** Optical image of the contacts connected to graphene after the electron beam exposure and development. The green area is still covered with PMMA.

#### 2.1.4 Deposition and lift-off

After the development, the darker areas in Figure 2.6 are bare, with no resist adhering to the substrate surface. Then, we deposited the necessary materials (Au in this case) to make contacts. The deposition process can be done using several techniques, such as electron beam evaporation, atomic layer deposition, and sputtering. For an electron beam evaporation process, the electron beam is oriented on the target material that is usually put in a crucible. The high energy of the electron beam directly evaporates the target material to form a thin film at our substrate, which is put above the crucible<sup>129</sup>. The deposition rate can be controlled by the size and location of the electron beam. Another popular technique for making films is atomic layer deposition (ALD), a much more complicated method that coats the substrate layer by layer in the form of a single atomic film. The chemical reaction of a new atomic film layer is directly related to the previous layer. In this way, only one layer is deposited in each reaction, and this chemical reaction repeats, fabricating the final film layer by layer<sup>130</sup>.

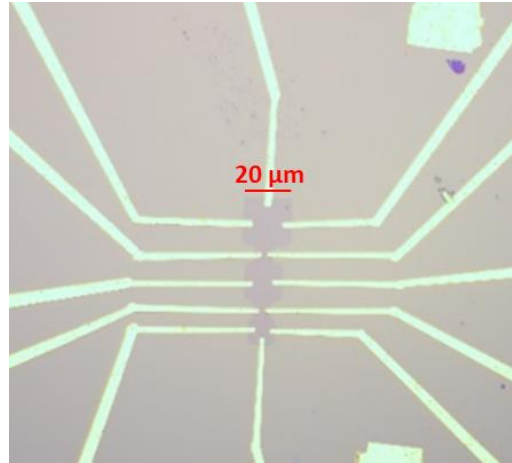


**Figure 2.7** Optical image of the final sample after the lift-off process. (Purple area means graphene, and the yellow area represents gold contacts.)

After the deposition, the final step of the procedure was the lift-off process. The whole sample was put in acetone for 12 hours or in hot acetone (usually 45°C) for a shorter time. All PMMA was dissolved by acetone. For our device, the gold adhered to the substrate surface in the gap will remain, and the one above PMMA will be taken away in the solution, which made the final pattern of the contacts. Finally, we cleaned the residual acetone with IPA and dried the sample with an N<sub>2</sub> gun. Figure 2.7 shows the final device's image after electron beam evaporation with 3 nm Cr and 80 nm Au (Cr helps strengthen the adhesion between Au and the substrate.) and lift-off process. Figure 2.8 concludes the whole process of the lithography process, which has been explained thoroughly in this section.

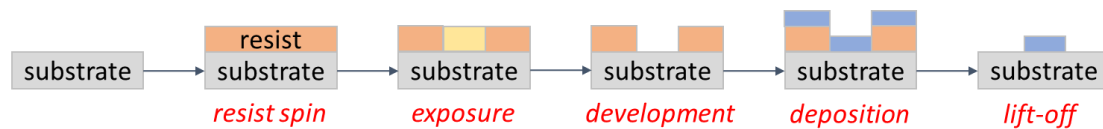


**Figure 2.8** Schematic of the lithography and lift-off process. For the exposure process, the beam could be either light or electrons with corresponding resist types.

## 2.2 Characterisation techniques

### 2.2.1 Raman spectroscopy

Raman spectroscopy was invented by Raman and Krishnan in 1928<sup>131</sup>. Raman spectrum measures the energy shift between the incident and scattered photon when the incident light is scattered inelastically by the atoms or molecules of the sample. Raman scattering contains two modes: Stokes and anti-Stokes, shown in Figure 2.9. For Stokes scattering, the incident photon excites the electron to a virtual state, and then the electron returns to its vibrational state. Therefore, the scattered photon has lower energy than the incident one. For anti-Stokes scattering, the electron is already at the vibrational state and then excited to a virtual state and transits to the ground state. Therefore, the scattered photon has higher energy than the incident photons. Usually, Stokes scattering is stronger because more electrons are located at the ground state. Different materials have unique Raman shifts, which can be used to characterize different samples.

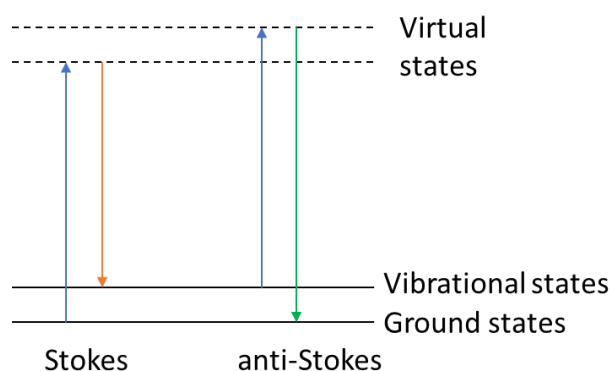


**Figure 2.9** Schematic of Stokes and anti-Stokes modes of Raman scattering

Raman spectrum is a reliable technique to distinguish the monolayer property of 2D material<sup>36</sup>, which has been shown in Chapter 1 (Figure 1.3b and Figure 1.7 for the Raman spectrum of monolayer graphene and MoS<sub>2</sub>). For graphene, except for detecting

the layer numbers, the Raman spectrum can even be able to tell its doping level by the ratio of 2D and G peak intensities and the full-width at half-maximum (FWHM) of the G peak<sup>39</sup>.

### **2.2.2 Atomic force microscopy**

Atomic force microscopy (AFM) was invented in 1980 by Binnig, Quate, and Gerber<sup>132</sup>. AFM detects the interaction between a cantilever tip and the sample surface, from which the morphology information of the sample surface can be deduced. Compared with scanning tunneling microscopy (STM) developed earlier by Binnig and Rohrer<sup>133</sup>, there is no requirement for the sample's conductivity, so its application is greatly expanded.

Atomic force microscopy (AFM) contains three parts: laser, detector, and cantilever tip, shown in Figure 2.10. A low-power laser spot irradiates on the back of the cantilever tip, and the reflected signal is projected on the photodetector. The curvature radius of the probe tip is about several nanometers. When the tip sweeps on the sample's surface, the interaction force between the tip and the sample will lead to the deflection and vibration change of the cantilever. As a result, the reflected beam spot's position on the photodetector screen is also changed. By analyzing the signal information from the photodetector, the surface morphology of the sample can be deduced. In this thesis, AFM (Bruker Dimension Icon) is used to measure the thickness and roughness of 2D material and thin films. Tapping mode is used where the cantilever vibrates at its resonant frequency and regularly taps the sample surface.

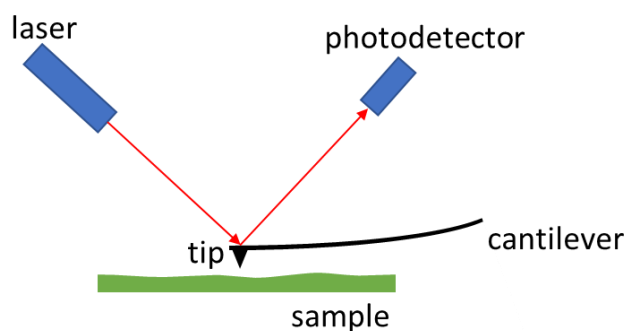


**Figure 2.10** Schematic of the atomic layer microscopy

### 2.2.3 Scanning electron microscopy

Although Max Knoll<sup>134</sup> produced a photo using an electron beam scanner two years earlier, scanning electron microscopy (SEM) was firstly presented by Manfred von Ardenne<sup>135</sup> in 1937 by scanning a small raster with a focused electron beam. The principle of SEM is using a narrow-focused high-energy electron beam to scan the sample point by point, with the help of the scanning foil. Due to the interaction between the incident electron and the sample, secondary electrons will be excited. By collecting, amplifying, and re-imaging these secondary electrons' information, the morphology of the material can be characterized. The simplified structure of a scanning electron microscope is shown in Fig. 2.11. The electron beam from the electron gun is focused with a group of magnetic lenses, and the beam size is selected by a shielding aperture. After passing through a set of scanning coils (controlled by the sweeping circuit to scan on the sample with a certain order) and an objective lens, the electrons are emitted on the sample. Detectors are installed above the sample to collect the secondary electrons and other particles. The collected electrons then form the final image at the image module, which contains a photomultiplier tube, video amplifier, and screen. The scanning electron microscope used in this thesis is the Zeiss EVO MA10 electron microscope, with a resolution of 100 nm.

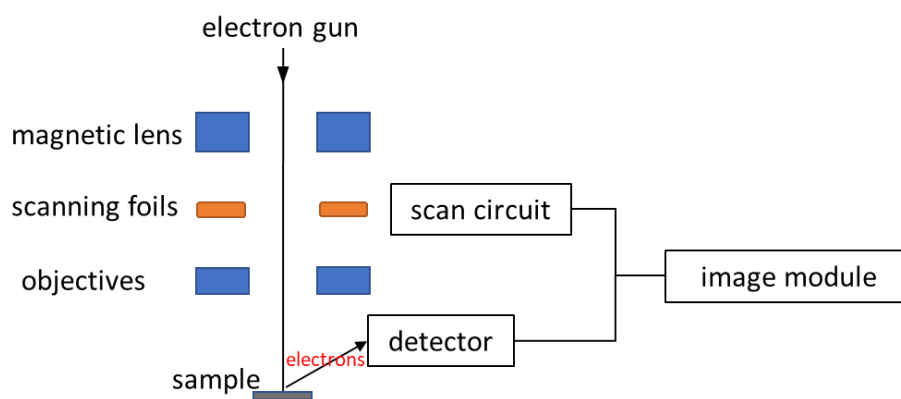


**Figure 2.11** Simplified schematic of the scanning electron microscope

### 2.2.4 X-ray photoelectron spectroscopy

X-ray photoelectron spectroscopy (XPS) is a surface analysis method. Similar to SEM where secondary electrons are excited, in an XPS measurement, X-ray irradiates on the sample, and the inner electrons or valence electrons of the sample atoms are excited and emitted out<sup>136, 137</sup>. These excited electrons by X-ray are called photoelectrons. The energy and quantity of these excited photoelectrons are then measured, which are determined by their binding energies, therefore the element composition and chemical state of the sample surface could be identified, including the molecular structure and atomic valence state and chemical bonds of various compounds. For XPS measurement, the excited photoelectrons only come from the surface of the sample (usually 10 nm analysis depth), and could analyze a small area and has tiny damage to the sample.

### 2.2.5 Ellipsometry

Ellipsometry measures the ratio of light reflection for two different polarization when the light is reflected by the measured material (usually thin films). In this way, the thickness and optical properties of the material can be determined<sup>138, 139</sup>. P. Drude<sup>140</sup> firstly built this instrument, while Rothen<sup>141</sup> named it ellipsometry in 1945. An ellipsometer contains four parts: a lamp, polarizer, analyzer, and detector, which is

shown in Figure 2.12. The incident light becomes polarized after passing through the polarizer. An optional compensator is sometimes used here to modify the polarization state further. Then, the incident polarized light emits on the sample, partly transmitting into the sample and partly reflected at the surface. The reflected light passes an analyzer and is collected by the detector. The detector measures two ellipsometry parameters  $\Psi$  and  $\Delta$ , which are related to the Fresnel reflection coefficients  $r_p$  and  $r_s$  (p- and s- refer to the polarization direction) by the following equation.

$$\rho = \frac{r_p}{r_s} = \tan\Psi e^{i\Delta} \quad (2.1)$$

By taking a group of reflection spectra at different incident angles, the thickness and refractive index of the films involved can be restored using Fresnel's equations and mathematical modeling. Except for the characterization of the film properties, the spectroscopic ellipsometry can also be directly utilized to obtain the reflection spectra for polarized light (see chapter 3). Furthermore, ellipsometry can also measure the transmission spectra (not included in this thesis). The ellipsometer used in this thesis was J. A. Woollam M-2000F variable-angle spectroscopic ellipsometer.

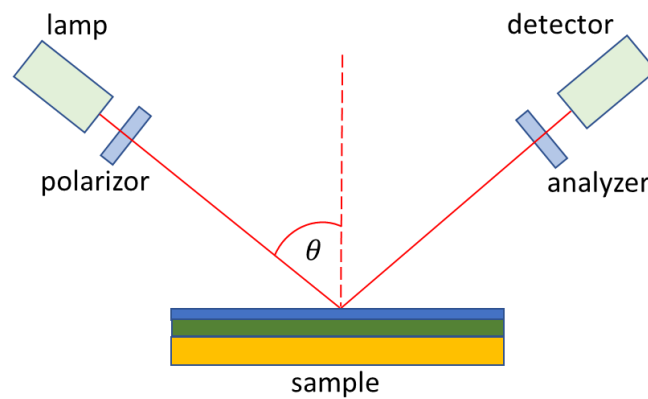


**Figure 2.12** Schematic of the ellipsometer set-up, working at the reflection mode. Ellipsometry usually needs at least four groups of data measured at different incident angles to get the accurate parameters of the film properties.

### 2.2.6 Fourier transform infrared spectroscopy

The principle of Fourier transform infrared (FTIR) spectroscopy is to use Fourier transform to decompose the interference pattern obtained by the interferometer<sup>142</sup> structure to produce the wavelength-dependent spectrum. Fellgett presented the first idea of this technology in 1951 in his thesis<sup>143</sup>. Compared to traditional dispersive spectroscopy (mostly relying on an optical grating structure), FTIR has a higher spectral resolution, faster detection speed, and a more substantial signal-to-noise ratio.

Figure 2.13 displays the structure of FTIR, which consists of four parts: multiple light sources to determine the spectrum of different ranges; a Michelson interferometer structure with two reflection mirrors. The movable mirror makes a specific optical path difference between the two split beams; then the composite beam can form the constructive or destructive interference; Detector which is similar to dispersive infrared spectrometers; Data processing system which performs the Fourier transform to obtain the frequency spectrum from the time domain interferogram (with all frequencies information combined). In this thesis, FTIR spectroscopy is performed with a Bruker Vertex 80 system and a Hyperion 3000 microscope.

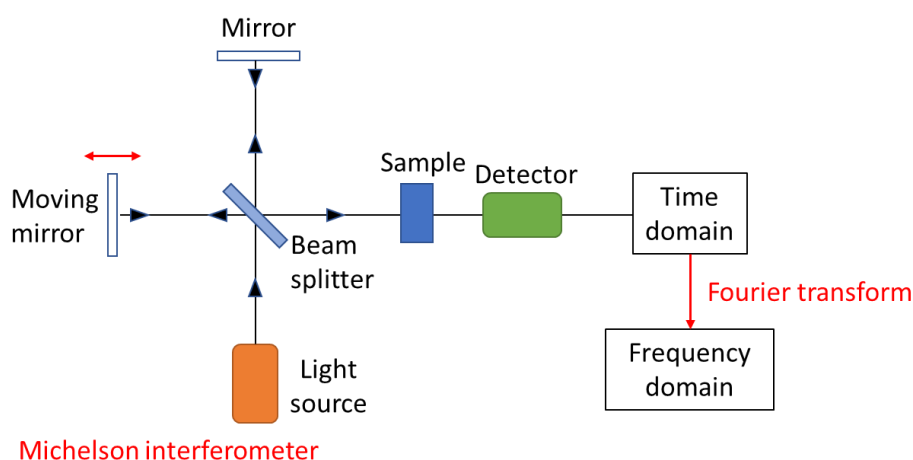


**Figure 2.13** Schematic of a Fourier transform infrared spectrometer, mainly containing a Michelson interferometer and a Fourier transform calculating module.



### 2.2.7 Electronic transport measurements

To measure the transport characteristics of graphene, two probe measurements were conducted in this thesis. The circuit diagram is shown in Figure 2.14. A lock-in amplifier (SR830, Stanford) provides an a.c. source and the voltmeter. For the lock-in amplifier, the alternating current (AC) power source generates the electrical signal at a specific frequency, and the voltmeter only measures the signal at that frequency, therefore highly reducing the noise, which is very useful for small signal measurements.

The resistance of graphene was at the kilo-ohms scale. The load resistance  $R_s$  was usually set as a  $\sim M\Omega$  scale in our measurement, significantly larger than the graphene resistance  $R_g$ . If the source voltage is  $V_s$ , the current flowing through graphene would be  $\frac{V_s}{R_s}$ . Usually, the current is controlled at less than  $1 \mu A$  to protect the nanodevices.

Then, another gate voltage  $V_{gate}$  was applied (with the help of a Keithley 2400 Source meter) to change the graphene carrier density, which leads to its resistance change. As a result, the measured value from the voltmeter was monitored. Using a Labview program, we swept the gate voltage at a certain range/speed and recorded the measured voltage from the lock-in amplifier. While applying the gate voltage, the leakage current was also recorded at the same time. Usually, a  $\sim nA$  scale leakage current assures the stability of the nano-devices. If the leakage current was too large or reached the set value, it implied that the gate voltage possibly reached a breakdown value for a specific dielectric layer.

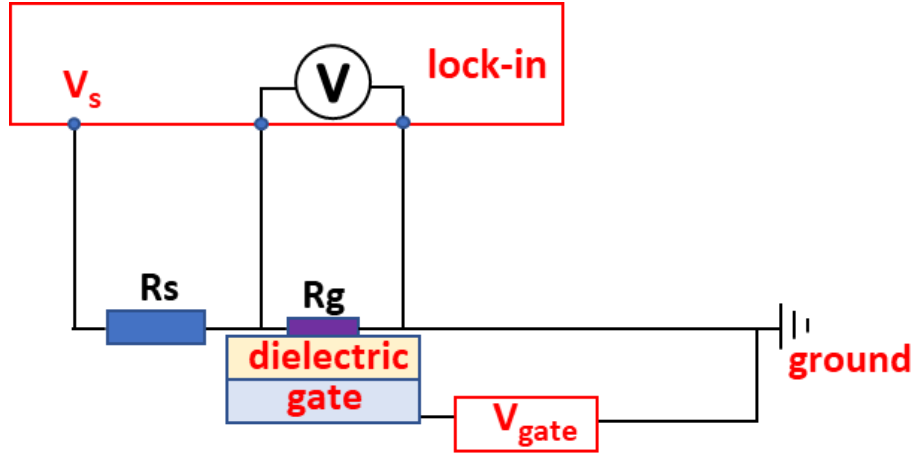


**Figure 2.14** Electrical circuits of transport characteristic measurements of a simple graphene gating device. The purple rectangle refers to graphene (or other measured samples) with resistance  $R_g$ .

### 2.2.8 Finite-Difference Time-Domain simulation

Finite-difference time-domain (FDTD) is an important method in the field of electromagnetic field simulation. Currently, there are two famous software on the market Lumerical FDTD solutions and Comsol Multiphysics. FDTD method was proposed by K. S. Yee in 1966<sup>144</sup>, based on Maxwell equations. In an FDTD simulation, the analysis space is grided. Given an initial setting, the electrical field and magnetic field can be calculated step by step with time. Therefore, we can obtain the steady-state result from the time-domain signal. By building the dispersion characteristics of the material and device structure, wide-band multi-wavelength results could be obtained at one time. With the development of computer technology, the FDTD method has made great progress in electromagnetics, electricity and optics. In Chapter 4, we used FDTD solutions and Comsol multiphysics to simulate the electrical field inside a plasmonic waveguide structure.

# Chapter 3

## A MoS<sub>2</sub> electro-optical modulator based on Fabry-Perot structure

*This chapter describes an electro-optical modulator that consists of a CMOS-compatible silicon nitride (Si<sub>3</sub>N<sub>4</sub>) dielectric layer sandwiched between a gold (Au) film and a molybdenum disulfide (MoS<sub>2</sub>) monolayer to enhance the electrooptical absorption of MoS<sub>2</sub> with the help of the Fabry-Perot structure. Our modulator achieves a polarization-selective modulation at a narrow wavelength range near the MoS<sub>2</sub> energy of excitons, reaching a 6 dB maximum visible light modulation depth. The possibility of using two-dimensional materials to modulate visible light by our device and the reasonably large modulation depth achieved with MoS<sub>2</sub> may contribute to the manufacture of reliable electro-optical visible-range optical modulators. We also extracted the gate dependence of the optical constants of MoS<sub>2</sub> and model it with a Lorentzian function (describing frequency-dependent dielectric constant) for the first time. The work is published in NPJ 2D Materials Applications<sup>62</sup>. In this work, I helped build the transmission matrix model of the device and did the simulation of the nanodevice's reflection at different incident angles. I measured the AFM images of the samples, performed ellipsometry and FTIR measurements.*

### 3.1 Introduction

The birth of 2D materials has brought new blood for various applications from tiny electro-optic and optoelectronic devices<sup>3, 5, 19</sup>, to bio-sensing<sup>6</sup>, and data-storage devices<sup>7</sup>,

etc. As illustrated in section 1.3, compared to the bulk semiconductor material, 2D materials offer promising properties in the field of optical modulation which needs the manipulation of light-matter interaction, especially with its easily controllable optical properties. Electrical control is one of the feasible methods for tuning the optical constants of 2D material. Multiple electro-optical modulators based on 2D material have been reported<sup>19</sup>, which also provided new insights into properties of 2D materials and the working mechanisms. Monolayer molybdenum disulphide (MoS<sub>2</sub>) has attracted large interest in electro-optics in recent years due to its unique band structure and excitonic excitations<sup>11, 47, 48</sup>. Monolayer MoS<sub>2</sub> is composed of S and Mo atoms planes with an ionic-covalent interaction. Unlike the indirect bandgap of bulk MoS<sub>2</sub> semiconductor, its monolayer has a direct bandgap of  $E_g \approx 1.9$  eV, which is specially located at the visible range (details illustrated in section 1.3.1). Compared to graphene, MoS<sub>2</sub> is much more chemically and electrically stable, which provides feasibility for practical optoelectronic devcies.

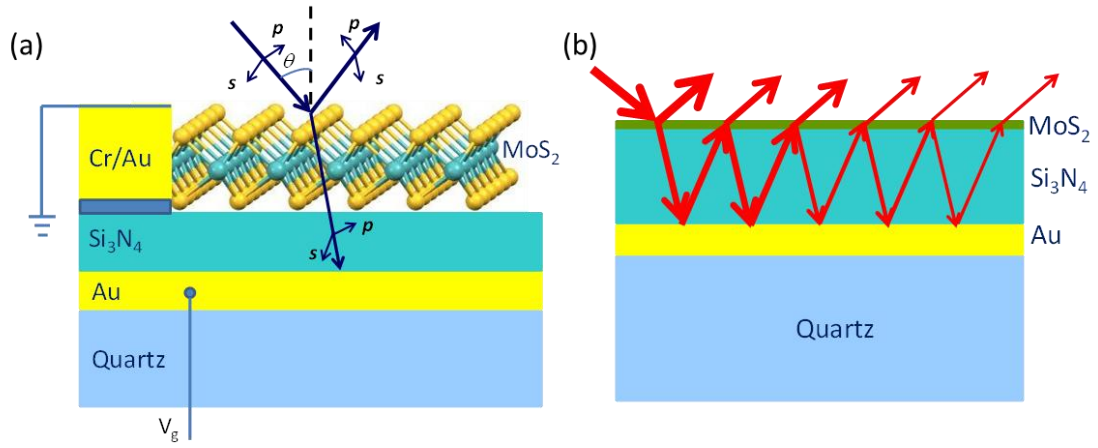
Compared to other 2D materials, MoS<sub>2</sub> has a relatively large absorption of visible light at the level of up to 10%<sup>83</sup>, produced by the dipole transition between localized d-orbitals. However, this is still not enough for the application of a practical optical modulator with an adequate modulation depth. Previous reported MoS<sub>2</sub> optical modulator has a light modulation at the level of only 4% with a 280 nm SiO<sub>2</sub> electrical-gating dielectric layer at a relatively large gate voltage range from -70 V to 80 V<sup>22</sup>. Therefore, to make an effectively working optical device, different structures are usually designed to promote the interaction between light and MoS<sub>2</sub>. It is reported that by coupling MoS<sub>2</sub> with metamaterial structures<sup>145</sup> or plasmonic nano-particles<sup>25, 146</sup>, the light-matter interaction between MoS<sub>2</sub> and light can be enhanced. Optical cavities were

also used to increase the absorption of monolayer MoS<sub>2</sub> by coupling atomic-thick MoS<sub>2</sub> to the cavity structure<sup>147</sup>.

Here we describe a hybrid planar metal-dielectric-2D material nanostructure, combining MoS<sub>2</sub> monolayer, silicon nitride (Si<sub>3</sub>N<sub>4</sub>) dielectric, and the bottom gate Au. These three components make up a Fabry-Perot structure, which effectively enhanced the absorption of MoS<sub>2</sub> for absorptive optical modulation. Our device demonstrated a 6 dB (440%) visible light modulation depth at a large incident angle by controlling the bottom gate voltage. The modulation is mainly located at a narrow range of the excitonic band of MoS<sub>2</sub>, whose optical constants are controlled by the electrical field. Our device offers a practical and straightforward solution for visible light modulation.

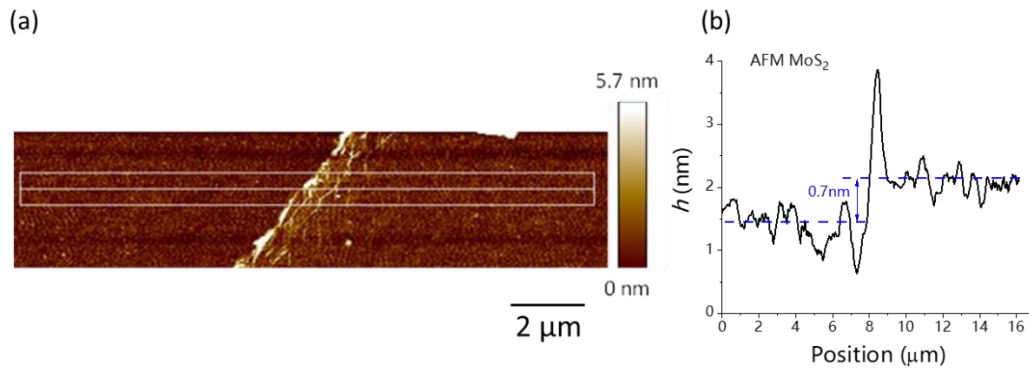
### 3.2 Sample preparation

Figure 3.1a shows the schematics of our device and light propagation in it. A silicon nitride (Si<sub>3</sub>N<sub>4</sub>,  $\epsilon = 8.5$ ) layer is sandwiched between MoS<sub>2</sub> monolayer and bottom gold film. Ellipsometry was used to measure the optical reflection with s- and p- polarized light. The gold film works as a gate contact and a reflecting mirror; see Figure 3.1. To fabricate the device, a 65 nm Au film was first evaporated by electron beam on a 1 mm thick quartz substrate with a 3 nm Cr adhesive layer underneath. A 390 nm thin Si<sub>3</sub>N<sub>4</sub> dielectric layer was then deposited on the substrate by chemical vapor deposition (CVD). A CVD MoS<sub>2</sub> monolayer (from 2D semiconductor company) on PMMA was transferred (facing down) on the substrate through a micromanipulator. Then the whole sample was baked, and PMMA was dissolved by acetone. Finally, Au contacts were connected to the top monolayer MoS<sub>2</sub>, making the final device.



**Figure 3.1** (a) The schematic of our modulator device. Polarized light emits on monolayer MoS<sub>2</sub> at an incident angle and transmits through. (b) Multiple internal reflections caused by Au/Si<sub>3</sub>N<sub>4</sub>/MoS<sub>2</sub> Fabry-Perot structure lead to the enhancement of the optical absorption of the MoS<sub>2</sub> monolayer. (From Ref. 62)

The property of MoS<sub>2</sub> monolayer has been characterized by AFM. A microscope image of MoS<sub>2</sub> monolayer on Si<sub>3</sub>N<sub>4</sub> and the corresponding AFM image captured with the tapping mode is shown in Figure 3.2. The measured thickness was around 0.7 nm, proving the monolayer property of MoS<sub>2</sub>.



**Figure 3.2** (a) Contact-mode AFM image of a MoS<sub>2</sub> monolayer with Si<sub>3</sub>N<sub>4</sub> underneath. (b) The measured thickness of monolayer MoS<sub>2</sub>. The jump in the plot is caused by the rolls at the edge of the MoS<sub>2</sub> monolayer and the fluctuations are mainly caused by the surface roughness of Si<sub>3</sub>N<sub>4</sub> and Au.

### 3.3 Normal reflection

We found that the intensity modulation of the reflected light with the gate voltage at the normal incident angle was not a good choice. Figure 3.3 shows the reflection spectra at different gate voltages normalized at the reflection spectrum at zero gate voltage  $R(V_g)/R(V_g=0V)$  for our device measured with the help of FTIR. The applied gate voltage changes the carrier density in  $\text{MoS}_2$ <sup>48</sup>, affecting its interaction with light at the excitonic band. From the analysis in section 3.5, we could know that the absorption coefficient of monolayer  $\text{MoS}_2$  decreases when the gate voltage increases from -100 V to 100 V, which causes less absorption and more reflection. We measured a maximum reflection modulation of 3% at the maximum positive and negative voltages applied. The relative reflection spectrum in Figure 3.3 shows typical peaks at 665 nm while the positive/negative gate voltage increases/decreases. The leakage current for our device at  $V_g=100$  V was only 1 nA, which suggests good dielectric quality of the dielectric  $\text{Si}_3\text{N}_4$  layer.

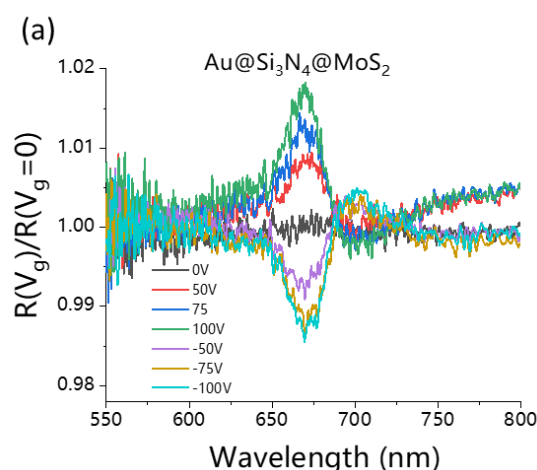


**Figure 3.3** (a) Normal incident relative reflectance spectra at different gate voltages normalized by the spectrum with  $V_g = 0$  V.

### 3.4 Reflection modulation with gate voltage at oblique incidence

For a normal incidence, the reflected light intensity change is only 3% with gate voltages, shown in Figure 3.3. However, at a large incident angle, due to the multi internal reflections of monolayer MoS<sub>2</sub> and light, we achieved close to 13% s-polarized light reflection change, measured with an ellipsometer (VASE, J.A. Woollam Co., Inc.) with a 50  $\mu\text{m}$  focal spot on MoS<sub>2</sub>. Figure 3.4 shows the reflectivity of our Au/Si<sub>3</sub>N<sub>4</sub>/MoS<sub>2</sub> nanostructure under differently polarized light as a function of the incident angle. We observed two pronounced and deep Fabry-Perot resonances near 480 nm and 630 nm for s-polarized light, Fig. 3.4(a). The resonance minima for p-polarized light were less pronounced and weaker, see Fig. 3.4(b).

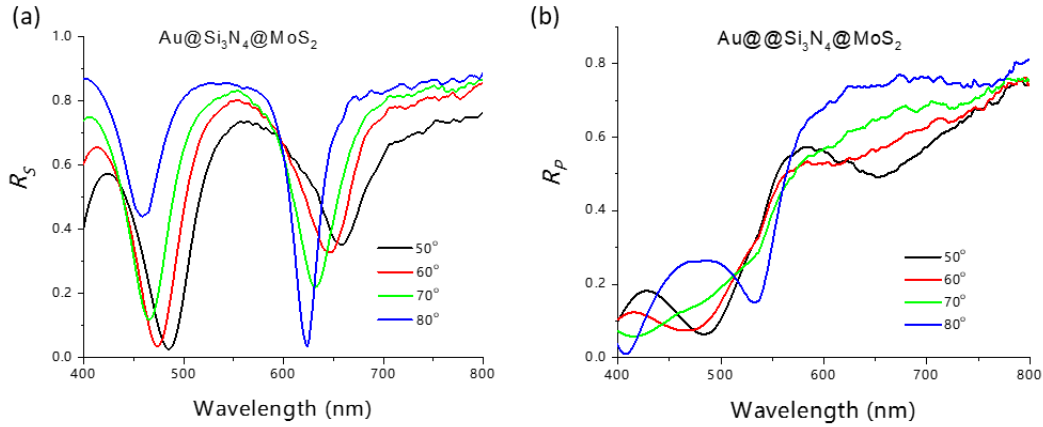


**Figure 3.4** (a) The reflectivity change under different incident angles for (a) s-polarized light and (b) p-polarized light of our Au/Si<sub>3</sub>N<sub>4</sub>/MoS<sub>2</sub> device

One can see that larger incident angles resulted in a narrower and deeper minima in the reflection spectrum for s-polarized light observed in the range of 550-700 nm. Therefore, we measured the gate voltage-dependent modulation at an incident angle of 80° for s-polarised reflectance  $R(V_g)$ . Figures 3.5a, b display the results. The absolute value of  $R_s(V_g)$  changes more than 10% in the gate voltage range between 0 and 100V,



with a relative ratio of  $R_s(V_g)/R_s(0\text{ V})$  up to 440%, which gives a modulation depth of 6 dB with an insertion loss of 15 dB. The modulation enhancement is mainly caused by the multi-interactions between light and monolayer  $\text{MoS}_2$  and the FP resonance property located at the excitonic band of monolayer  $\text{MoS}_2$ . When a gate voltage is applied, the excitonic absorption of monolayer  $\text{MoS}_2$  is decreased, which leads to the reflection increment. With a modulated gate voltage, we could have a modulated reflective light intensity. Researchers have achieved a 15 dB modulation depth with graphene in the near-infrared range<sup>72, 74</sup>.  $\text{MoS}_2$  is a good material for modulators working at the visible range. We also measured the gate voltage-induced modulation for p-polarised light, which shows a much more broadband modulation beyond the resonance peaks area (Figures 3.5c, d). We consider that the special gating response for p-polarized light is related to the out-of-plane dipoles of  $\text{MoS}_2$ , therefore showing a different spectrum compared to the s-light response. The in-plane and out-of-plane photo-luminescence have been reported in  $\text{MoS}_2$  monolayer where the out-of-plane dipole photo-luminescence emission was much smaller than that of the in-plane dipole photo-luminescence<sup>148</sup>.

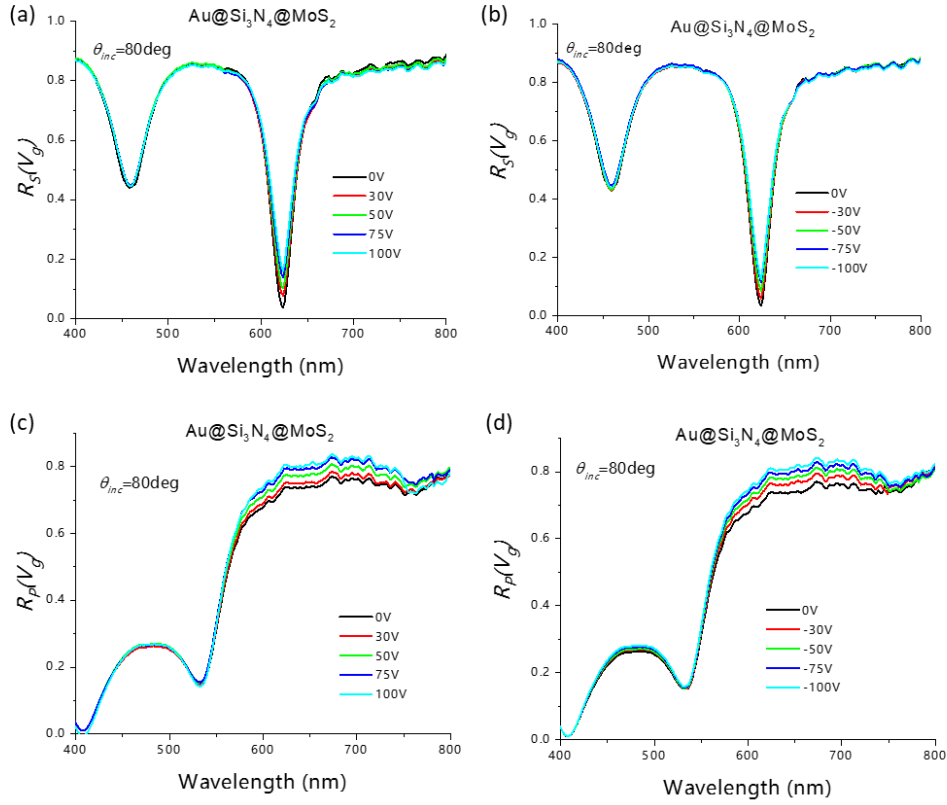


**Figure 3.5** The gate voltage dependence (from -100 V to 100 V) of the reflection change for (a, b) s-polarized light and (c, d) p-polarized light of our Au/Si<sub>3</sub>N<sub>4</sub>/MoS<sub>2</sub> device.

### 3.5 Optical constant analysis from ellipsometry

One of the advantages of ellipsometry is that it can provide the optical constant information by modeling the ellipsometric spectra  $\Psi$  and  $\Delta$  (see section 2.2.4 for theory about ellipsometry). This method can be used to directly characterize the complex refractive index of a MoS<sub>2</sub> monolayer and its dependence on the electrical field. To this end, we used a Fresnel multilayer model that contains a quartz substrate, an Au layer, a Si<sub>3</sub>N<sub>4</sub> dielectric, and a 0.7 nm MoS<sub>2</sub> monolayer. Our work provides the first detailed analysis of the dependence of the refractive constants of MoS<sub>2</sub> on the applied gate voltage.

The spectrum of the gate voltage-dependent optical constants  $n(\lambda)$  and  $k(\lambda)$  are shown in Figure 3.6, extracted from the variable incident angle ellipsometry measurements. We observed two significant peaks at the wavelength range of 550-700 nm in both  $n$  and  $k$  spectrum. The A and B exciton transitions between the valence band and the conduction band result from the spin-orbit interaction splitting, as mentioned in section 1.3<sup>22</sup>.

The optical constants for positive and negative gate voltages shown in Figure 3.6 are symmetric with respect to the gate voltage 0 V, which reveals that the change of optical constants near the exciton band is mainly caused by the gate voltage induced change of charge carrier density of MoS<sub>2</sub> monolayer. The refractive index real part  $n$  and imaginary part  $k$  both decrease with the increase of gate voltage (from -100 V to +75 V) in the range of 600-700 nm. With the increment of the gate voltage from -100 V to 75 V, the number of induced electrons in MoS<sub>2</sub> is increased, which reveals that the contribution from A and B exciton transitions are suppressed by the induced electrons, which can be explained by the Pauli blocking effect when the electrons influence the optical absorption from the excitons in MoS<sub>2</sub>. However, the exact effect could be much more complicated, as both the refractive index  $n$  and extinction coefficient  $k$  of MoS<sub>2</sub> has a dependence on the gate voltage, and both of them have slight peaks shifts, and the initial doping of monolayer MoS<sub>2</sub> should also be considered. We will use a multi-Lorentzian dispersion model in the next section to investigate the gate-voltage-dependent dielectric constant of monolayer MoS<sub>2</sub>.

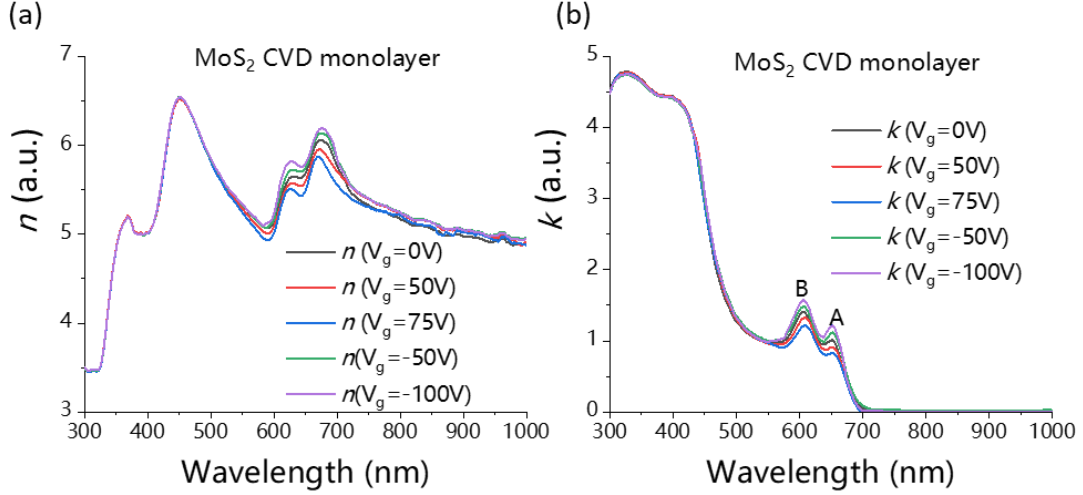


**Figure 3.6** Gate voltage dependence of the complex refractive index of monolayer MoS<sub>2</sub>, extracted from ellipsometric data: real part  $n$  (a) and imaginary part  $k$  (b).

### 3.6 Lorentzian dispersion model

Compared to the Drude model, which describes the dielectric constant of metal (see section 1.5.2), a Lorentzian model is widely used to describe the dielectric constant of a semi-conductor. A multi-Lorentzian function<sup>149</sup> can be used to model the extracted dielectric function of the CVD MoS<sub>2</sub> monolayer from the ellipsometric data

$$\varepsilon(\omega) = 1 + \sum_{m=1}^N \frac{f_m}{E_m^2 - E^2 - iE\gamma_m} \quad (3.1)$$

where  $f_m$  is the oscillator strength,  $E_m$  is spectral resonance energy, and  $\gamma_m$  is the spectral width, for the  $m$ -th oscillator. By fitting the multi-Lorentzian function to the measured refractive index data shown in Figure 3.6 through the equation  $\varepsilon(\omega) = (n+ik)^2$ , we get the evaluated numbers for the corresponding parameters of the Lorentzian function to describe the dielectric constant of a MoS<sub>2</sub> monolayer. It needs to be noted that several batches of ellipsometric data at different incident angles and gate voltages are used for this fitting process. The analytical parameters obtained of the  $f_m$ ,  $E_m$ , and  $\gamma_m$  parameters

are presented in Table 1, and Figure 3.7 compares the fitted result with the measured one for 0 V and 75 V gate voltage.

**Table 1.** The fitted multi-Lorentzian parameters for the complex refractive index of MoS<sub>2</sub> monolayer as a function of the gate voltage.

$m$	MoS <sub>2</sub> monolayer					
	$V_g = 0 \text{ V}$			$V_g = 75 \text{ V (-100 V)}$		
	$E_m \text{ (eV)}$	$f_m \text{ (eV}^2\text{)}$	$\gamma_m \text{ (eV)}$	$E_m \text{ (eV)}$	$f_m \text{ (eV}^2\text{)}$	$\gamma_m \text{ (eV)}$
1 (A)	1.89	0.4	0.059	1.89	0.15 (0.57)	0.068 (0.073)
2 (B)	2.03	1.75	0.12	2.03	1.15 (2.03)	0.17 (0.15)
3	2.877	42.5	0.37	2.87	42.5	0.37
4	2.275	5.0	1.2	2.275	5.0	1.2
5	3.745	160	1.3	3.77	160	1.3

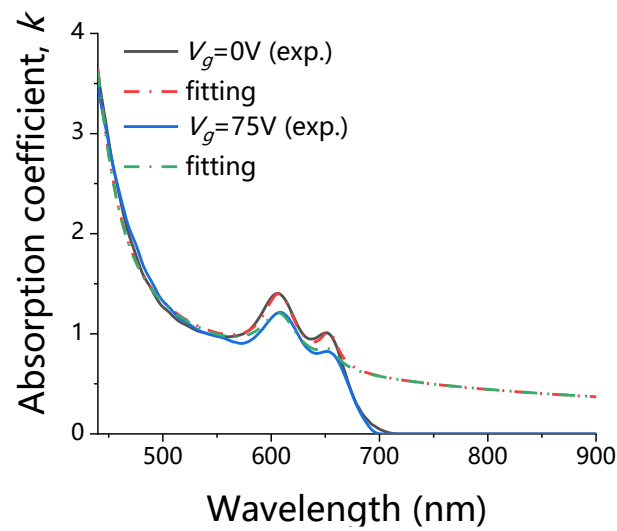


**Figure 3.7** Measured and fitted absorption coefficient of monolayer MoS<sub>2</sub> for different gate voltages.

For A and B excitonic transitions, which correspond to the first and second k-th oscillator in the multi-Lorentzian function, the fitting results in table 1 show that only

oscillator strengths  $f_m$  and widths  $\gamma_m$  display significant change under the external electrical gate voltage  $V_g$ , while the excitonic transition energies  $E_m$  do not change significantly with the change of  $V_g$ . This is in good agreement with the theory where the screening effects on the bandgap renormalization and the exciton binding energy could cancel out<sup>150</sup>. Therefore, the refractive index changes with different gate voltages are mainly contributed by changing the oscillator strength  $f_{A,B}$  and spectral width  $\gamma_{A,B}$ , while the former one has a negative correlation with the gate voltage  $V_g$ .

The induced carrier density in MoS<sub>2</sub> through the geometrical capacitance is

$$n = \frac{\varepsilon_0 \varepsilon_{st} V_g}{de} \quad (3.2)$$

where  $\varepsilon_0$  is the free space permittivity,  $\varepsilon_{st}$  is the static dielectric constant of the Si<sub>3</sub>N<sub>4</sub> film which is extracted from our FTIR measurement,  $d$  is the thickness of the Si<sub>3</sub>N<sub>4</sub> layer, and  $e$  means the electron charge. We plotted the dependence of the oscillator strength and spectral width at different gate voltages (with different carrier densities), with results shown in Figure 3.8. The original carrier density in monolayer MoS<sub>2</sub> is about  $n_0 = 2 \left( \frac{2\pi m_0 kT}{h^2} \right)^{\frac{3}{2}} = 4.32 \times 10^{12} \text{ cm}^{-2}$ , where  $m_0 = 0.5m_e$  is the effective electron mass for MoS<sub>2</sub> bulk,  $k$  is the Boltzmann's constant,  $T$  is the temperature set at 300 K, and  $h$  is Plank's constant.

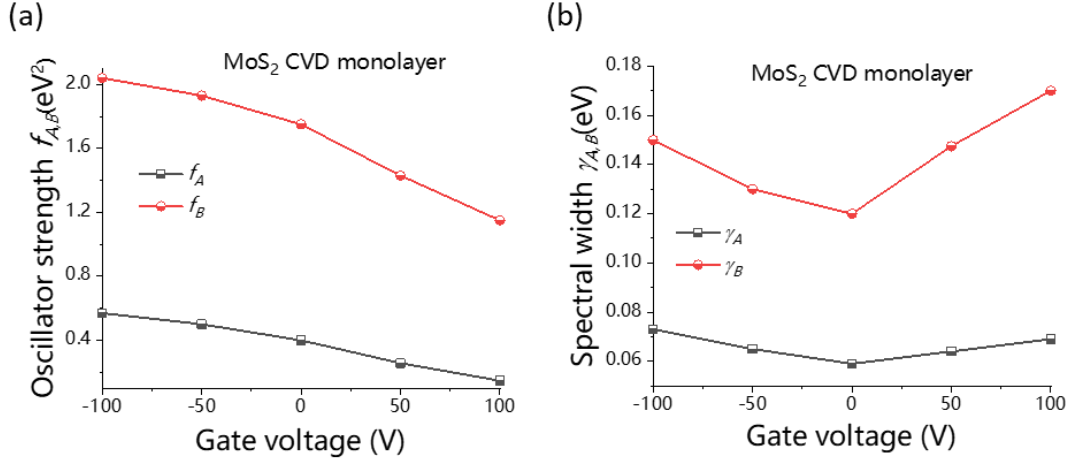


**Figure 3.8** The parameters of the multi-Lorentzian dielectric function dependent on the gate voltage. (a) oscillator strengths,  $f_A$ , and  $f_B$  and (b) spectral width  $\gamma_A$  and  $\gamma_B$  of A and B excitonic absorption bands on the gate voltage.

Consider the gate voltage  $V_g$  range from 0 to 100 V; the carrier density would increase as the gate voltage increases, which witnessed a broadening of the spectral width at the A and B excitonic absorption bands (increment of  $\gamma_{A,B}$ ). The situation is the same for the negative gate voltages. To explain  $f_{A,B}$ 's dependence on the gate voltage, we proposed a possible mechanism for the gate voltage-dependent absorption at the excitonic band of a MoS<sub>2</sub> monolayer—the Pauli blocking effect<sup>31, 151</sup>. As mentioned in section 1.2.2, due to the Pauli exclusion principle, an increment of the carrier density will make part of the phase space unavailable for the new formation of excitons, which can be described with an applicable multiexciton Wannier formalism for MoS<sub>2</sub> monolayer in our case<sup>152, 153</sup>. We suggest that the excitons and conduction electrons occupy different regions of the phase space for MoS<sub>2</sub> monolayer and the induced electron density  $n = \frac{C_{Si_3N_4} V_{gate}}{e}$  causes the reduction of the exciton oscillator strength  $f_{A,B}$ . We proposed a rough equation to describe the relationship between the oscillator strength and the induced electron density as below.

$$f_{A,B} = f_{A,B}^0 \left( 1 - \frac{n}{n_{eff}} \right) \approx f_{A,B}^0 (1 - n \cdot \pi a_B^2) \quad (3.3)$$

where  $a_B$  refers to the effective Bohr radius. Therefore, we could fit the oscillator strengths  $f_{A,B}$  as a function of the induced electron density through a linear correlation and obtain the effective Bohr radius of an exciton through equation 3.3. The estimated  $a_B$  is 1.4 nm and 1.1 nm for A and B excitons, respectively.

For our device, the MoS<sub>2</sub> monolayer is sandwiched between air ( $\epsilon_{air}=1$ ) and a Si<sub>3</sub>N<sub>4</sub> dielectric layer ( $\epsilon_{st}(\text{Si}_3\text{N}_4)=8.5$ ), evaluated from FTIR measurement and could be found in<sup>62</sup>). Hence, an average dielectric constant of the MoS<sub>2</sub> during the ellipsometry measurement process can be calculated in a simple approximation<sup>110, 154</sup>:  $\epsilon_{st} = \frac{\epsilon_{air} + \epsilon_{Si_3N_4}}{2} = 4.75$ . Using  $m_e=0.35m_0$  for electron mass and  $m_h=0.428m_0$  for hole mass, in units of bare electron mass  $m_0$ , we can estimate the effective Bohr radius of an exciton in monolayer MoS<sub>2</sub> to be  $a_B \approx 1.3$  nm through the equation  $a_B = \frac{4\pi\epsilon_{st}\hbar^2}{e^2} \left( \frac{1}{m_e} + \frac{1}{m_h} \right)$ , which is close to the analyzed effective Bohr radius from the fitting results in Figure 3.7.

### 3.7 Transfer matrix modeling

Transfer matrix method<sup>155</sup> is widely used in optics and acoustics. In this method, the change of an electromagnetic wave or acoustic wave after propagating through a medium could be mathematically described by a matrix applied on the original matrix, which contains the wave information before the propagation through the medium. Each medium could be treated as a matrix. Therefore, through the matrix operation, we could get the electromagnetic field at any medium.



The Fabry-Perot resonance formed at a large incident angle leads to the multi-interactions of light and monolayer MoS<sub>2</sub>. Besides, the interference increases the local electrical field, thus increasing the optical absorption and modulation induced by the gate voltage. The gate-voltage reflection can be simulated qualitatively by the transfer matrix method based on the thickness information of structural components and the extracted complex refractive index of MoS<sub>2</sub> monolayer from Figure 3.6. The refractive index of CVD Si<sub>3</sub>N<sub>4</sub> film is modeled with a Cauchy function

$$n_d = 1.988 + \frac{0.02}{\lambda^2} + \frac{0.0003}{\lambda^4} \quad (3.1)$$

where  $\lambda$  is the wavelength of the incident light. The simulated reflection of s- and p-polarization are shown in Figures 3.9a and b, with a good agreement with the experimental results shown in Figure 3.5. The slight difference may be caused by surface roughness and impurities.

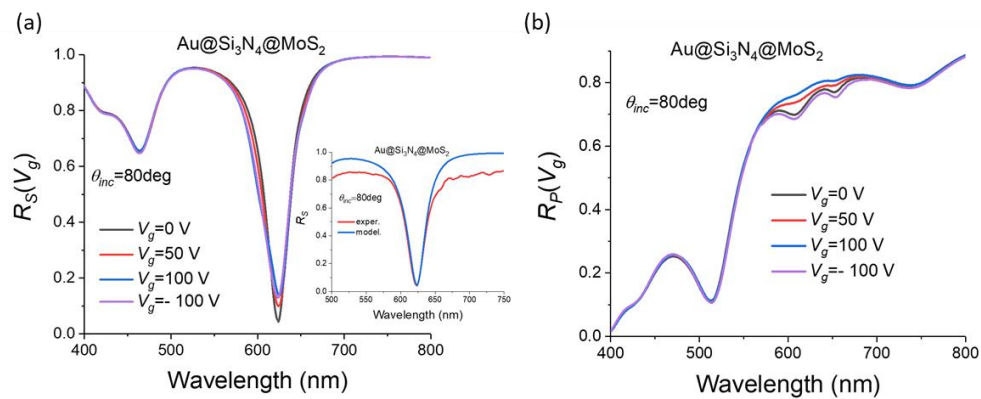


**Figure 3.9** The simulated result of the gate voltage-dependent reflection of differently polarised light based on the transfer matrix method. Inset of Figure a: Comparison of experimental and simulated s-polarization reflectivity at 0 gate voltage.

### 3.8 Conclusion

We fabricated an electro-optical modulator based on monolayer MoS<sub>2</sub> and a simple Fabry-Perot structure. With the help of Fabry-Perot resonance, the optical modulation can be enhanced to 6 dB for visible light at an 80-degree incident angle for s-polarized light, whose modulation depth is among the best for MoS<sub>2</sub> based optical modulators<sup>22, 25, 156</sup>. The modulation induced by the applied gate voltage is located in the excitonic band of the MoS<sub>2</sub> monolayer. Besides, we extracted the gate voltage-dependent complex refractive index of MoS<sub>2</sub> monolayer by ellipsometry and modelled it with a Lorentzian model. The absorption coefficient  $k$  is only gate-dependent in the excitonic range of MoS<sub>2</sub> (about 550-700 nm). A simple Fresnel model based on the transfer matrix fits our experimental data well. Due to the good stability of MoS<sub>2</sub>, our device still works after a couple of years. With a high modulation depth, our device shows promising applications in the field of visible light modulators.

# Chapter 4

## A graphene plasmonic slot waveguide modulator

*Plasmonic devices enable electrooptical control of light inside subwavelength regions, providing new opportunities for chip-based industry, such as signal-processing components in integrated computational network devices. In this chapter, we demonstrate a hybrid graphene modulator based on a plasmonic slot waveguide structure. This modulator works at 1550 nm, performing a 0.13 dB/ $\mu\text{m}$  modulation depth (12% absorption modulation for a 4  $\mu\text{m}$  graphene piece) by modulating the amplitude of the gap surface plasmon mode via the gate-controlled absorption of graphene. In addition to the modulation, our novel structure could be utilized for nanoscale light field imaging with a  $\sim 20$  nm spatial resolution with the help of graphene, determined by the p-n junction width induced in the graphene sheet by gating. This is much better than the resolution of optical detection subject to the Rayleigh criterium, and hence our work pushes forward the development of nanoscale integrated circuits and technology. In this work, Fran Rodriguez and I fabricated and measured all devices with the help of Vasyl Kravets and Fred Schedin. I did the simulation of the light field distribution. The theoretical model for the light field distribution based on the p-n junction was built by Vladimir Zenin, Sergey Bozhevolnyi, Konstantin Novoselov, and Alexander Grigorenko. The manuscript is under the second review in Nature Photonics.*

## 4.1 Introduction

Integration of electronic and photonic components on the same chip could highly reduce the industrial cost and promote the performance of the chip. However, there remains a critical mismatch between the electronic and photonic components introduced by the different dimensions of electrons and photons. Plasmonic devices paved the way for the next chip generation, which confines optical modes to the subwavelength scale. It could interconnect high-speed photonic and nanoscale electronic components, producing a nanoscale communication system<sup>28</sup>. Moreover, the large electromagnetic fields produced by the plasmonic resonance could enhance nonlinear optical effects<sup>157</sup>. Initially, prisms or gratings were indispensable to excite surface plasmon polariton (SPP) due to the  $k$  vector mismatch between SPP and the incident light (see section 1.5.2), limiting the miniaturization of plasmonic devices. This was overcome by various structural plasmonic devices reported in recent years, including stripes array devices<sup>118</sup>, metal grooves channel devices<sup>119, 158, 159</sup>, waveguide slot(gap) devices<sup>35, 114, 120, 160</sup> and nanodots arrays-based plasmonic surface lattice resonances devices<sup>161</sup>. The plasmonic slot waveguide with a metal-insulator-metal (MIM) structure is an attractive candidate with highly confined plasmonic modes and a relatively simple fabrication process.

Graphene has emerged as a promising material in photoelectronic devices because of its broadband and gate-controllable light absorption and high carrier mobility<sup>16, 84, 162, 163</sup>. Moreover, graphene is compatible with virtually any substrate, perfect for monolithic nanoscale integrated circuits and CMOS technology<sup>164</sup>. Graphene-based optical modulators and detectors have been widely studied, with excellent modulation depth/speed and photo-responsivity<sup>16, 20, 165, 166</sup>. However, graphene-based plasmonic devices have not been comprehensively investigated in this field yet. Many applications

focus on the biosensing area, utilizing the high sensitivity of the surface plasmon change based on the interaction between graphene and biomolecules<sup>167, 168</sup>. Several hybrid graphene plasmonic modulators have been reported, which work at the infrared range. A graphene plasmonic slot waveguide electro-optical modulator that uses the leaky mode of SPP showed modulation of 0.13 dB/ $\mu\text{m}$  and low insertion loss<sup>169</sup>. Another mid-infrared graphene plasmonic modulator based on the high-quality collective plasmon resonances possessed a high reflection modulation depth of 20%, which is the largest measured so far<sup>118</sup>.

In this work, we integrated graphene with a plasmonic slot waveguide structure and successfully used graphene to modulate the gap surface plasmon (GSP) mode in the waveguide slot, reaching a 0.13 dB/ $\mu\text{m}$  modulation depth (12% absorption change), which is comparable with the latest results<sup>169</sup>. Except for the optical modulation, we proposed a novel method for nanoscale light field imaging with the help of graphene, with a 20 nm spatial resolution determined by the p-n junction width introduced by our waveguide structure, whose details will be illustrated in sections 4.4 to 4.6.

## **4.2 Device structure and fabrication methods**

The plasmonic slot waveguide configuration is shown in Figure 4.1. The waveguide was designed to operate at telecom wavelengths. Two 4  $\mu\text{m}$  wide graphene pieces were wet transferred on the silicon substrate, which has a 1500 nm oxide layer on the top. As we used incident laser signal at 1500 nm, the thick dielectric silicon oxide layer can minimize the penetration and leakage of the plasmonic signal to the impure silicon underneath, which effectively decreased the loss. A 30 nm thick high  $\kappa$  constant hafnium oxide dielectric layer is sandwiched between the waveguide structure and graphene stripes. The 100 nm- thick waveguides with a 300 nm slot between two sides

were deposited with silver. Silver contacts to the graphene flakes and the waveguide legs were also fabricated during this process with the same thickness. Besides, a 1.5  $\mu\text{m}$  thick layer of PMMA covers the whole device, including the slot, which avoids the oxidization of silver.

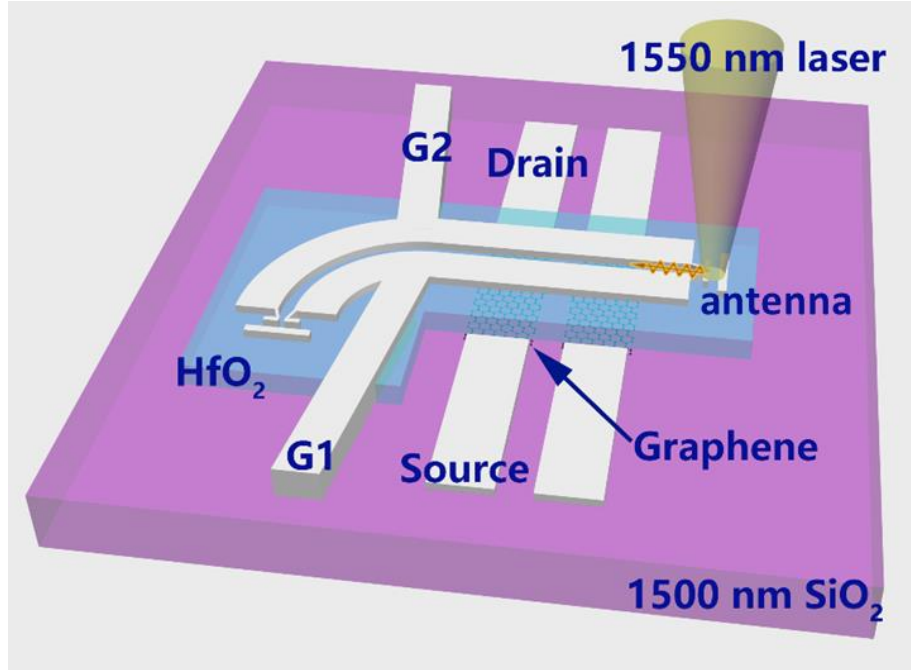


**Figure 4.1** Schematics of the antenna-coupled plasmonic waveguide device. Two pieces of graphene were fabricated in our device. Two antennas (with reflectors) are fabricated separately at the input and output of the waveguide for coupling and decoupling of the incident and waveguide mode.

Light confinement and power loss are two essential indicators for lightwave communication devices. Although the local field is enhanced and better confined, plasmonic waveguides possess increasing total propagation loss caused by the field overlap with the metal, compared to nanoscale photonic waveguide devices with the same MIM structure<sup>120, 170, 171</sup>. Besides, the insertion loss caused by the mismatch between the fiber-transmitted incident light and the excited plasmonic mode field is another problem. Different antenna structures have been developed under such

circumstances to diminish the insertion loss, such as tapered waveguide antenna<sup>169</sup>, bottom reflectors around antenna<sup>172</sup>, and Yagi-Uda style nano-antenna<sup>114, 173</sup>. Two 100 nm-severed dipole nano-antennas are used in our device at both ends to efficiently couple/decouple normally incident free-space propagating radiation into the GSP mode supported by the plasmonic slot waveguide. The incident wave normally emits on one antenna and is then coupled to the waveguide slot. Furthermore, the slot waveguide (produced by two metal stripes) had a 90° bend designed to change the polarization of the output beam by 90° with respect to the polarization of the input beam. This design could enhance the visibility of the out-coupled (relatively weak) radiation as compared to that specular-reflected at the input coupler by using crossed polarizers (see Figure 4.3).

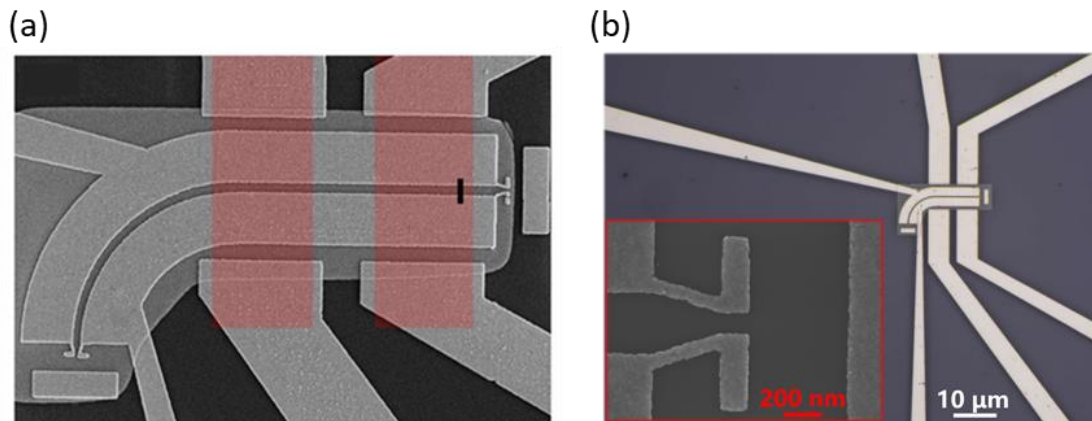


**Figure 4.2** (a) SEM image of the device. The white areas correspond to the silver waveguide and electric contacts. The slightly darker area corresponds to the hafnium oxide dielectric. The positions of graphene stripes are marked with a red color. The black scale bar across the waveguide slot corresponds to 1  $\mu\text{m}$ . (b) A microscope image of one device. Inset shows an enlarged picture of the nano-antenna and the reflector taken by scanning electron microscope.

To fabricate the device, a piece of graphene grown on copper by a chemical vapor deposition (CVD) process was transferred on a Si substrate with a top 1.5  $\mu\text{m}$  thick

SiO<sub>2</sub> layer using a standard wet-transfer method (see section 2.1.1 for details of the wet-transfer process). The area with good graphene quality was then defined by optical microscopy. Electron beam lithography and O<sub>2</sub>:Ar plasma etching were used to pattern two graphene stripes on the substrate. The dielectric layer pattern was made by electron beam lithography, and 30 nm hafnium oxide was deposited on the substrate above two graphene stripes by electron beam evaporation, which was performed by Moorfield deposition system at a speed of 0.6 Å/s. After the lift-off process, the sample was cleaned with IPA and deionized water. Then the waveguide structure and contacts pattern were again defined by a third electron beam lithography, using a 210 nm thick layer of PMMA and a high-resolution 100 kV beam. The exposed areas were developed at 5°C in MIBK: IPA 3:1 for 40 s and then IPA for 20 s. 1 nm Cr as an adhesion layer and 100 nm Ag were evaporated with a Moorfield electron beam deposition system, with a high deposition rate of 0.9 nm/s for the silver deposition. After the final lift-off, the waveguide structures were imaged with a scanning electron microscope (SEM). Then, the whole device was spin-coated by a 1.5 µm thick PMMA layer to protect silver from oxidation.

Exposure is the most difficult part of the whole fabrication process. To find the best dose to make the waveguide structure, we fabricated more than ten devices and compared their performances. In our results, 1900 µC/cm<sup>2</sup> of the high electron beam exposure gives the best performance (highest light transmission ratio through the waveguide), which corresponds to a roughly 300 nm wide waveguide gap.

### **4.3 Experimental setup and transmission modulation**

The experimental setup is shown in Figure 4.3. A 40x microscope objective with a 0.65 numerical aperture (NA) was used to focus 1550 nm light from a laser diode at the input



antenna and collect the emitted light at the output antenna. The incident light was polarized parallel to the input antenna by a polarizer for efficient coupling. As the output light will be orthogonally polarized from the incident one, another polarizer orthogonal to the input polarizer in front of the detecting camera can filter the output and the reflected light emitted from two antennas after collimation with the objective, as well as diminishing the scattered light signal. Using an InGaAs SWIR camera, we were able to check the excitation of the waveguide mode and detect the input and output light intensities, which can also help find the tiny sample on the substrate.

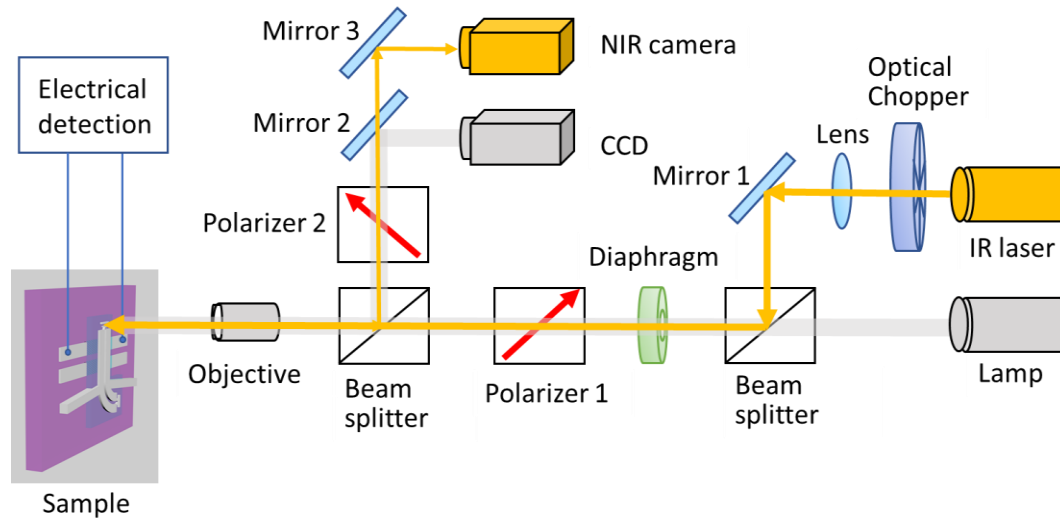


**Figure 4.3** The experimental setup. A lamp and CCD camera were used to observe the sample. A NIR camera was used to detect input and output signals and measure the light modulation with the gate voltage. An optical chopper and lock-in were used to achieve electrical detection between the source and drain of graphene, which will be illustrated in section 4.5.

First, the gating characteristics of graphene were determined by applying the same gate voltage to both waveguide sides G1 and G2, with the graphene strip being grounded (corresponding transport characteristic shown in Figure 4.11a). The ratio of the maximum and minimum values of the graphene sheet resistance was above 4, which suggests good quality of the CVD graphene used. We also checked that the graphene

strips interacts with the GSP waveguide mode by realizing modulation of output light intensity where graphene was gated to achieve the Pauli blocking effect.<sup>84, 174</sup> An image of the output light taken with the SWIR camera is shown in Figure 4.4a. The SWIR camera was also used to measure the light intensities. The total waveguide losses were estimated as the ratio of the average light intensity emitted from the output antenna over the average intensity of the incident light. To measure the intensity of the incident light, the laser spot was focused on a metal pad, and its reflected intensity was measured with the two polarizers set to be parallel.

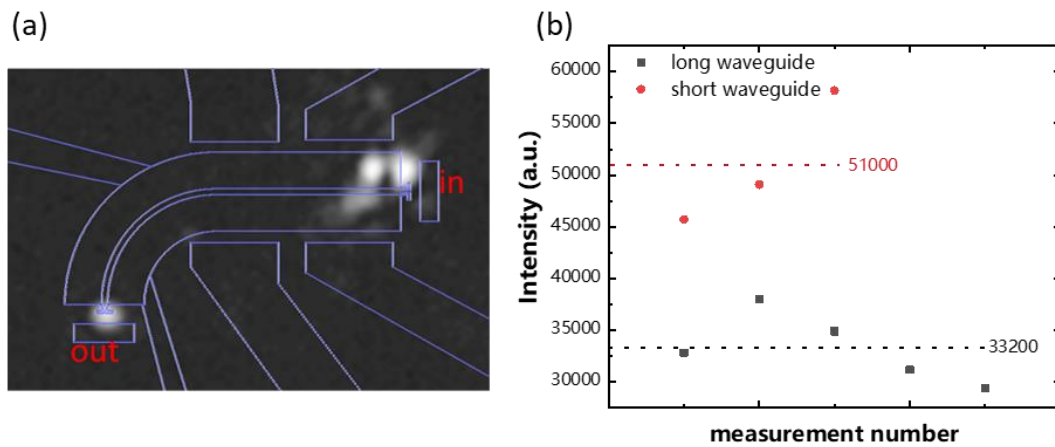


**Figure 4.4** (a) Light transmitted by the waveguide imaged with an InGaAs camera. The waveguide design is superposed on the image for reference. (b) The average intensity of the output light for short and long waveguide structures. We measured 3 short waveguide devices and 5 long waveguide devices from the same batch of fabrication. The red and black dash lines represent the measured average intensity for 3 short waveguides and 5 long waveguides, respectively.

To separate coupling and transmission losses, we fabricated two devices with different waveguide lengths of 20.8  $\mu\text{m}$  and 14.8  $\mu\text{m}$  (the coupling antennas and the bends were the same). The total losses for each waveguide were measured at the same input laser power (with no gating applied) in Figure 4.4b. The total light losses for the device can

be written as  $T_{tot} = K_{in}T(l)K_{out}$ , where  $K_{in}$  is the coupling coefficient for the input antenna,  $K_{out}$  is the coupling coefficient for the output antenna and  $T(l) = \exp(-\alpha l)$  is the losses in the waveguide defined by the loss factor,  $\alpha$ . Since the input and output antennas were identical, we assume that  $K_{in} = K_{out}$ . From the measured transmission for short and long waveguides, we have evaluated the coupling efficiency  $K_{in} = K_{out} = 7\%$  while the loss factor in the waveguide was found to be  $\alpha = 10 \text{ dB}/\mu\text{m}$ .

The mechanism of light modulation in our hybrid plasmonic slot waveguide was achieved by graphene gating. With a gate voltage, we could control the Fermi level in graphene in order to control its optical absorption by optical Pauli blocking as illustrated in section 1.2.2. By switching the absorption of graphene on and off, we could achieve a modulation of the waveguide light<sup>175</sup>. To achieve maximum light modulation, both stripes of the graphene were connected to the ground while both sides of waveguide G1 and G2 were connected to the modulation signal (simple schematic shown in Figure 4.5).

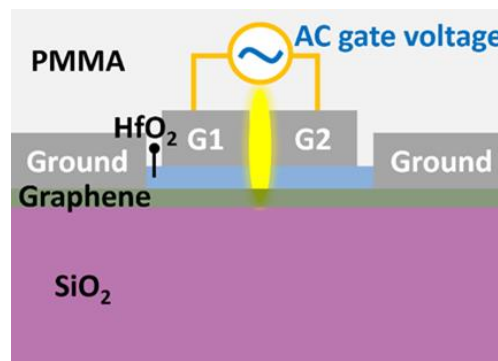


**Figure 4.5** The cross-section schematic of the plasmonic slot waveguide and the gate voltage connection for plasmonic modulation. An AC voltage is applied on both sides of the waveguide slots while graphene is grounded.

Figure 4.6a shows the modulation of the output light intensity under the application of a 1 Hz square-wave modulation signal with 6 V amplitude and 1 V offset to control the

absorption of graphene. The offset voltage was necessary to offset the Fermi level of graphene closer to the position where Pauli blocking<sup>84</sup> occurs at the wavelength of interest graphene (see section 1.2.2). In this case, when the gate voltage is 0 V, graphene is at the charge neutral point, having the maximum absorption. When the gate voltage is switched to 6 V (6 V AC gate voltage is the highest value we can apply on our device with 30 nm e-beam HfO<sub>2</sub> dielectric layer), the Fermi level reaches to the maximum, where graphene has a minimum absorption. Therefore, by applying a square wave electrical signal (AC gate voltage) from 0V to 6V, the maximum modulation of the transmitted output light (from the output antenna) in the plasmonic slot waveguide was achieved, close to 12% at 10 mW incident laser power for a 4  $\mu\text{m}$  graphene piece, which corresponds to the modulation depth of 0.12 dB/ $\mu\text{m}$ . The dark noise has been considered when calculating transmittance. The modulation result is reasonably good for the studied geometry<sup>175</sup>. On the other hand, the slot plasmonic waveguide and coupling antennas used in our work were designed for a broadband operation. We have tested our devices' optical properties using several laser diodes with wavelengths from 1300 nm to 1630 nm and observed similar modulation depths, shown in Figure 4.6b. We have also checked that our devices retained their modulation properties up to the modulation frequency of 100 kHz, which was the maximal frequency we can apply in our installation. The operation frequencies in similar graphene waveguide structures could reach 65 GHz.<sup>176</sup>

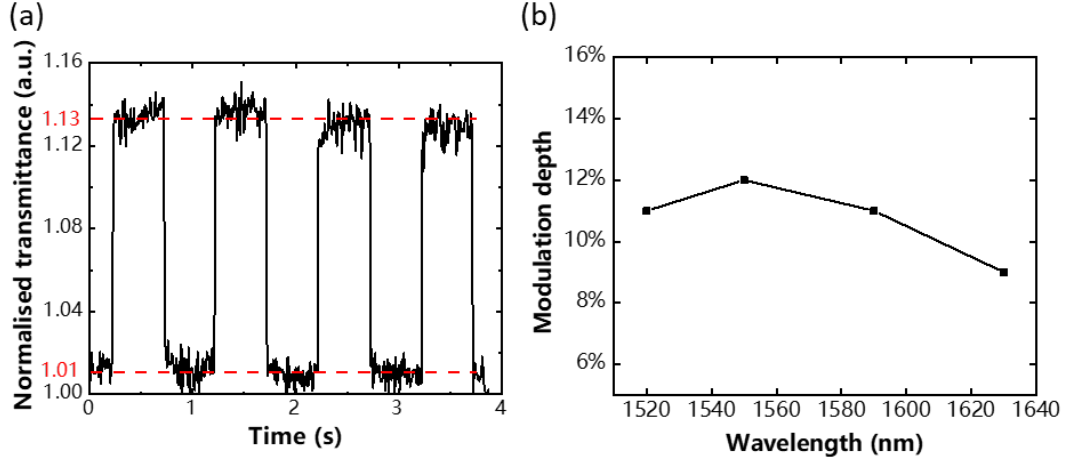


**Figure 4.6** (a) Normalized transmittance when applying a 1 Hz square modulation signal between 1 V and 7 V to both sides of the waveguide while graphene is grounded. (b) Broadband operation tests from 1300 nm to 1630 nm, which gives a reliable and scalable modulation.

#### 4.4 Concept of light field imaging in 2D

Recently, the developments of plasmonic structures<sup>107</sup>, plasmonic waveguides<sup>106</sup>, graphene plasmonics<sup>110, 177</sup>, optical phononics<sup>178</sup> and superlenses<sup>179, 180</sup> have significantly promoted the field of nanoscale light manipulation and characterization. However, due to the diffraction limit, the spatial resolution with an optical method is still limited to a fraction of the light wavelength light field, relying on the detection of the scattered optical fields<sup>181</sup>.

In this section, we will describe a new method of nanoscale light field imaging where we image the light but not the object with a lateral resolution of  $\sim 20$  nm by controlling the position of a  $p$ - $n$  junction induced in graphene with an external gate voltage, based on the photoelectric effect in the  $p$ - $n$  junction in our plasmonic waveguide sample. The optical field imaging was defined in the graphene plane by measuring the electric field profile of a strongly confined plasmonic slot-waveguide mode at telecom wavelengths, whose result was in excellent agreement with the numerically simulated mode profile.

Our method provides another way of nanoscale light field imaging with high spatial resolution and precision.

The concept of nanoscale light field mapping is illustrated in Figure 4.7, which is also based on our plasmonic waveguide structure discussed in this chapter. A graphene sheet is placed in the region of interest and electrically connected with source and drain contacts, which are made from the same material (Ag for our device) and are kept at the same temperature to avoid thermopower parasitic signals. A gate dielectric is deposited on top of graphene, and two parallel metallic gates are fabricated on top of the dielectric, which defines the orientation of the  $p$ - $n$  junction and the scanning direction. Two-dimensional light imaging with this concept is principally feasible but would require a more complex gating arrangement, with scanning directions parallel and perpendicular to the gate electrodes, respectively.

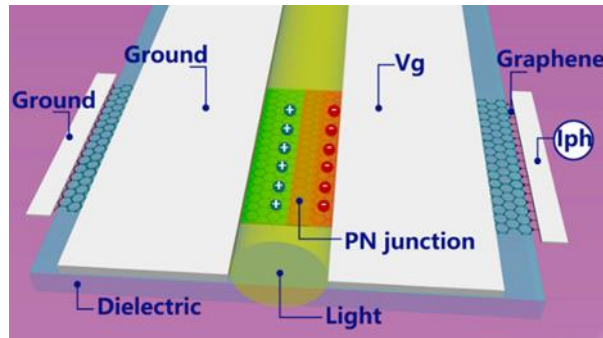


**Figure 4.7** Schematics of a  $p$ - $n$  junction induced in graphene by gating of a plasmonic waveguide.

When the area between the two gating contacts of graphene is exposed to light, an additional electrical signal could be observed between the source and the drain contacts, which can be contributed from several phenomena: the photoelectric<sup>182</sup>, thermoelectric<sup>183</sup>, and bolometric<sup>184</sup> effects, while bolometric effect should be zero in non-biased graphene<sup>184</sup>. It is worth mentioning that graphene absorbs  $\sim 2.3\%$  visible

and near-infrared light at normal incidence<sup>38</sup> and has the level of 0.01 – 0.1 dB/ $\mu\text{m}$  for confined plasmonic modes propagating along the graphene layer<sup>34</sup>. Therefore, the influence of graphene on light field distributions can be neglected.

The thermoelectric effect usually yields the largest contribution<sup>184</sup>. However, the thermoelectric contribution from the Seebeck effect should be zero where the source and the drain are made of the same material and are kept at the same temperature in our geometry. It needs to be mentioned that the thermoelectric Seebeck effect could have singular contributions when there is a discontinuity in the temperature derivative<sup>185</sup> or dependence of the mean free path of electrons on the wavevector<sup>186</sup>. Therefore, the main contribution to the electrical signal should come from the photoelectric effect for our geometry, which requires the presence of a *p-n* junction in graphene to separate electrons and holes produced during light absorption.

## **4.5 Light propagation in plasmonic slot waveguides**

The light propagation and field distribution in our device was modeled firstly with finite difference time domain (FDTD) simulations (Lumerical) for our experimental geometry and conditions. Figure 4.8 shows the simulated electric field components at the plane where graphene is located (graphene is not considered for the facilitation of simulation) with a 1550 nm excitation light at the input antenna with no applied gate voltage and graphene. All electrical field components are mostly symmetric concerning the middle of the waveguide, except for the asymmetry at the waveguide bend area.

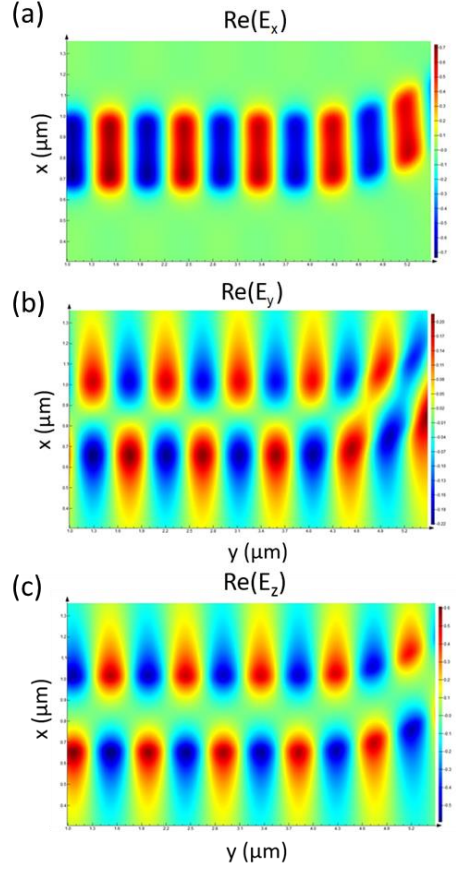


**Figure 4.8** Simulation of the electrical intensity at the plane graphene should be located at. (a) The 2D map of the real part of  $E_x$ . (b) The 2D map of the real part of  $E_y$ . (c) The 2D map of the real part of  $E_z$ .

Figure 4.9a reveals a detailed propagation and attenuation of the GSP mode in the slot waveguide. The simulated power transmission ratio  $P_{out}/P_{in}$  at the output and input antennas was 0.12%, close to the experimentally measured result in section 1.3. We further employed the two-dimensional (2D) mode analysis using the finite-element method (FEM) implemented in COMSOL software to get more accurate information of the studied GSP mode (FDTD solutions gives a 3D simulation for entire field distribution, and Comsol is better to deal with 2D simulation for better accuracy of the electric fields). The 2D distribution of electric field magnitude in the waveguide cross-section shown in Fig. 4.9b represents a typical GSP mode field profile in a slot



waveguide. The electric field component  $E_x$  is strong and weakly varies across the slot in the graphene plane, resembling the electrostatic field distribution in a capacitor.

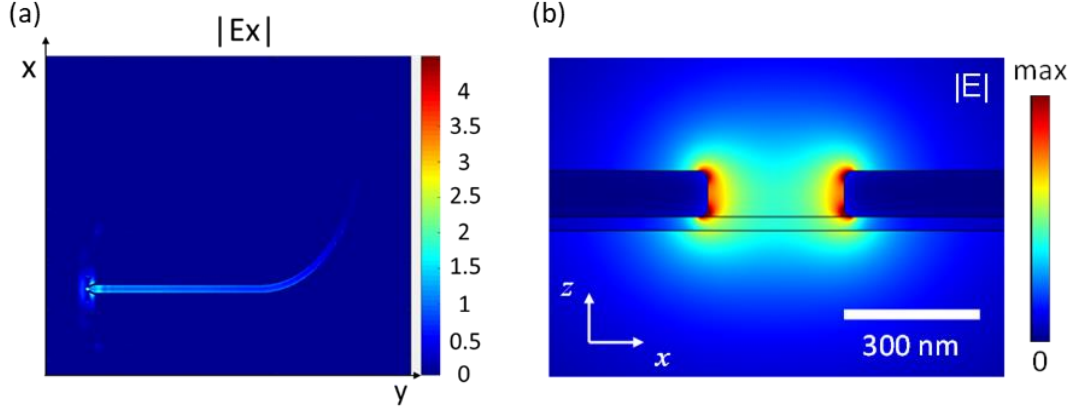


**Figure 4.9** (a) Simulated electric field distribution excited by a laser beam (wavelength of 1550 nm) that falls onto the input antenna (taken in the plane of the waveguide at the half-height of the waveguide and calculated with the help of Lumerical FDTD solutions). (b) Simulated electric field distribution in the cross-section of the plasmonic slot waveguide calculated with the help of Comsol software.

#### 4.6 Nanoscale light field imaging in graphene

Now we can suggest a conceptually new method of nanoscale light field imaging. Initially doped graphene is gated with a positively applied voltage  $V_{G2}$  while the other end is connected to the ground ( $V_{G1} = 0$ ). A  $p$ - $n$  junction is formed in the area where light is present in the waveguide slot, as shown in Figure 4.7. A non-zero photoelectric current is generated, proportional to the electric field intensity at the  $p$ - $n$  junction position, where the light-generated electron-hole pairs are separated due to the electric field applied.

To calculate the Fermi energy across the  $p$ - $n$  junction in graphene in our structure under the gate voltage shown in Figure 4.10a, we used the established methodology described

in<sup>187, 188</sup>, with a 30-nm-thin hafnia dielectric separator. The electrostatic problem can be addressed by solving the Poisson equation (cgs system) as

$$-\nabla(\varepsilon\nabla\varphi) = 4\pi\rho_{free}(\varphi) \quad (4.6)$$

where  $\varphi$  is the electric potential,  $\varepsilon$  is the dielectric permittivity of the materials involved,  $\rho_{free}(\varphi)$  is the density of the free charges with proper boundary conditions.

The density of free changes in graphene is  $\rho_{free}(\varphi) = \frac{\sigma(\varphi)}{t_{gr}}$ , where  $\sigma(\varphi) = e(p(\varphi) - n(\varphi))$  is the surface charge density,  $p(\varphi)$  and  $n(\varphi)$  are the graphene surface density of holes and electrons, and  $t_{gr}$  is the graphene thickness.

The surface density of holes and electrons for undoped graphene can be found as

$$p(\varphi) = N_G F_1\left(\frac{e\varphi}{k_B T}\right) \text{ and } n(\varphi) = N_G F_1\left(-\frac{e\varphi}{k_B T}\right),$$

where  $k_B$  is the Boltzmann constant,  $T$  is the temperature,  $N_G = \frac{2}{\pi} \left(\frac{k_B T}{\hbar v_F}\right)^2$  ( $v_F$  is the Fermi speed of the electrons in graphene

and  $\hbar$  is the Plank constant), and  $F_1(x) = \int_0^\infty \frac{u}{1+\exp(u-x)} du$ . The absence of the

current in graphene when there is no illumination implies that  $\varphi' = \varphi + \xi(x, T(x))/e = Const$ , which allows one to calculate the electric field inside the p-n junction. The free charges at the metal interface can be calculated using the mirror method.

In this case, a change in the gate voltage causes a lateral displacement of the  $p$ - $n$  junction location within the graphene sheet (see Figure 4.10b). The photoelectrical signal intensity depends on the light field intensity at the  $p$ - $n$  junction location. By moving the  $p$ - $n$  junction where the photoelectric signal is generated, we could accurately map the light field distribution across the gap between the gating electrodes. In contrast to scanning near-field microscopy<sup>189</sup>, this field mapping method does not involve any moving parts and is therefore amenable to precise control of the scanning coordinate.

The lateral size of the  $p$ - $n$  junction can be estimated from the built-in electric field distribution, shown in Figure 4.10c). For a 30-nm-thin hafnia separator, this value is around 20 nm, close to the previously reported values<sup>187, 188</sup>. This lateral size of the  $p$ - $n$  junction in graphene determines the spatial resolution (for one direction) of our described light field mapping approach, which can further be improved by decreasing the thickness of a dielectric layer or lowering the temperature.

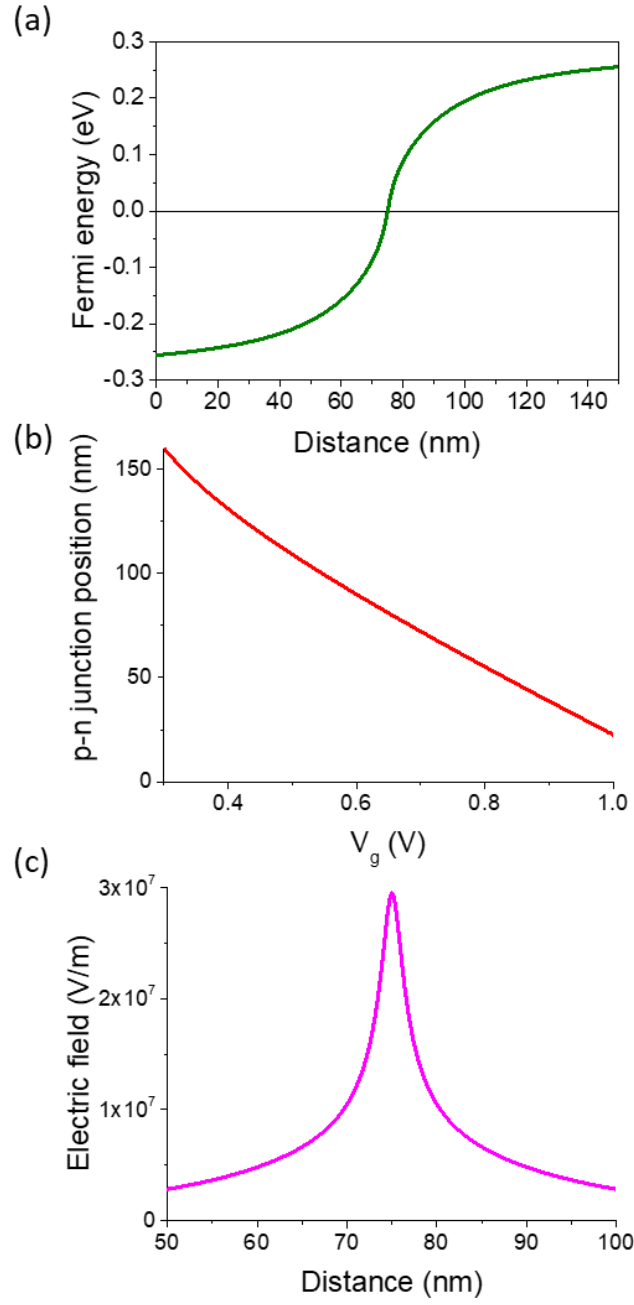


**Figure 4.10** (a) Fermi energy in initially doped graphene (x-axis refers to the position in the considered direction) calculated in the presence of a gate voltage applied to one side of the waveguide, (b) A graphene p-n junction position as a function of the gate voltage applied to one side of a waveguide (G2) while there other side (G1) is grounded. (c) The electric field of a p-n junction induced in graphene.

We conducted the nanoscale electric field mapping of the gap surface plasmon (GSP) mode supported with our plasmonic slot waveguide device shown in Figure 4.1. As

mentioned in section 1.5.3, plasmonic slot waveguides have been widely used in plasmon-empowered nanophotonics for demonstrating diverse ultra-compact components. In section 4.3, we could monitor the excitation of the waveguide mode with an InGaAs short-wave infrared (SWIR) camera and modulation of output light intensity was realized with gating graphene to achieve the Pauli blocking effect.<sup>84, 174</sup> Simultaneously, an induced gate voltage-dependent photoelectrical signal could be measured between the source and drain contacts, in the presence/absence of light. This measurement process was performed by either light modulation with an optical chopper and lock-in detection (photocurrent response due to the GSP mode absorption by graphene) or direct measurements of the photocurrent with a source meter (dark and light responses).

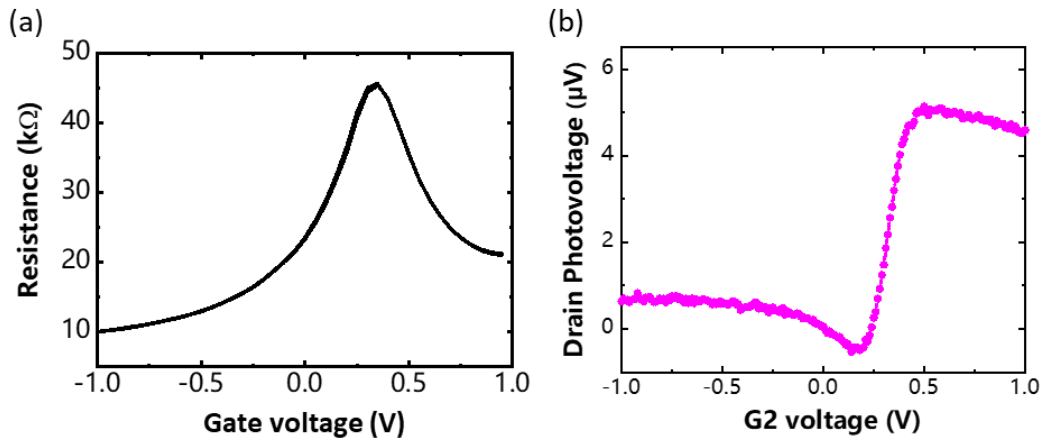


**Figure 4.11** (a) The resistance of graphene as a function of the gate voltage applied to both G1 and G2 contacts for a sample with a 30 nm HfO<sub>2</sub> dielectric layer. (b) A photovoltage measured between the source and drain of graphene as a function of the gate voltage G2 when the contact G1 is grounded. The photovoltage was measured with an optical chopper and lock-in amplifier.

We obtained the electrical mapping of light intensity with graphene by applying the gate voltage to contact G2 while G1 was grounded to form a *p-n* junction in graphene underneath, which could then be moved by adjusting the gate voltage on G2 (Fig. 4.10b).

Figure 4.11b shows the photovoltage measured with a lock-in detection (chopping rate at 800 Hz) as a function of the G2 gate voltage at zero applied bias between the source and drain contacts, with a 1550 nm and 0.5 mW input laser light. The photovoltage was close to zero for the gate voltages below 0.2 V, which is not large enough to induce enough electrons to make a p-n junction in graphene (as shown in Figure 4.11a in the left region of the charge-neutral point). This value increased sharply for larger gate voltages, reaching the maximum of  $\sim 5 \mu\text{V}$  at 0.4 V gate voltage.

We also measured the dependencies of the photovoltage and photocurrent on the gate voltage directly with a source meter under the light and dark conditions (i.e., with and without the incident light), while no bias voltage was applied between the source and drain (For this measurement, we measured several devices and Figure 4.11 shows the best results from one device). Both photovoltages (Fig. 4.12a) and photocurrents (Fig. 4.12b) in either light and dark conditions showed a non-zero limit at negative voltages, which is associated with the contact voltages. The difference between the dark and light photovoltages (yellow curve in Fig. 4.12a) and photocurrents (yellow curve in Fig. 4.12b) follow the same behavior as that observed in the lock-in measurements (Fig. 4.11b), which proved the repeatability of our results. The dark current and voltage dependencies are measured to be connected by Ohm's law, reflecting the gating characteristics of graphene stripes.

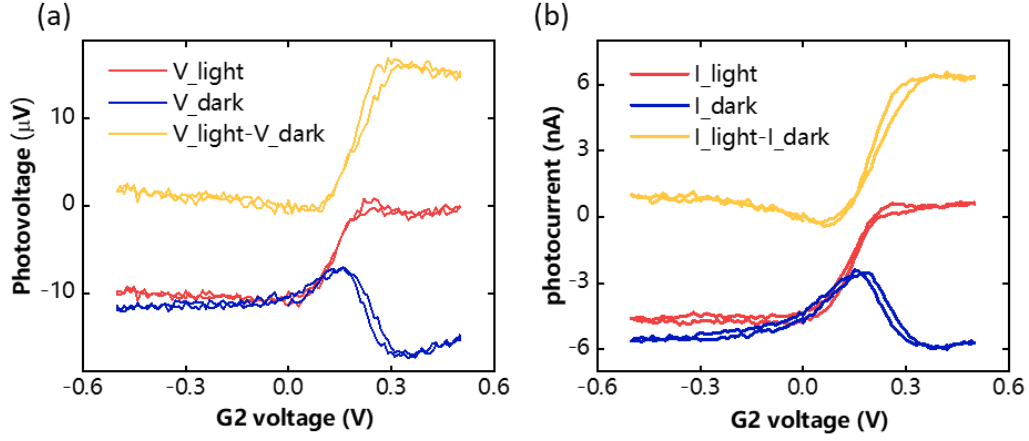


**Figure 4.12** (a) A photovoltage (drain voltage in an open circuit) and (b) a photocurrent (drain current in a short circuit) as a function of the gate voltage  $G2$  with and without light input through the waveguide, measured directly with a source meter. Both the source and the  $G1$  contact were connected to the ground.

Finally, the photovoltage showed a linear dependence on the incident light power (Fig. 4.13) as one would expect for the photo-response governed by the photoelectric effect, thus ruling out the influence of the thermoelectric effect with a non-linear dependence of the photo-response on the light power.

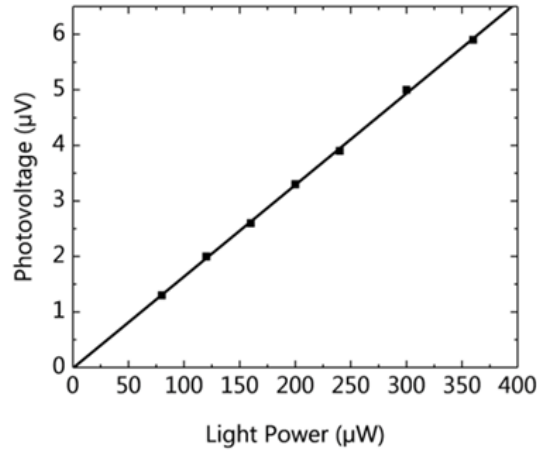


**Figure 4.13** The linear dependence of the photovoltage on the incident light power with a fixed gate voltage of 0.4 V applied to  $G2$ , and  $G1$  contact is grounded.

As discussed above, the photoelectric effect in the  $p$ - $n$  junction induced in graphene by the gate voltage contributed to the photo-response in our geometry. It is possible to plot the intensity of the electric field component in the graphene plane as a function of the  $p$ - $n$  junction position, thereby obtaining the gap surface plasmon (GSP) mode field profile in the plasmonic slot waveguide with the corresponding photo-response. Basically, the biased gate voltage determined both the position of  $p$ - $n$  junction (Figure 4.10b) and the photovoltage between the source and drain in graphene (Figure 4.11b). Then we could obtain the corresponding photovoltage for a specific position of the  $p$ - $n$  junction. Due to the low light intensity at graphene, we assume the induced photovoltage is linear dependent on the light intensity at graphene, which is also proved by Figure 4.13 and provides another direct evidence of the absence of significant thermoelectric contribution. Therefore, we could obtain the corresponding light intensity for a specific position of the  $p$ - $n$  junction, which is the reconstructed light intensity profile. Figure 4.14a shows the simulated field intensity inside graphene, and Figure 4.14b shows the excellent agreement between the calculated and reconstructed light intensity profile in graphene, which demonstrates the success of our electrical mapping method of optical field intensity using graphene. The spatial resolution of this mapping method depends on the properties of the  $p$ - $n$  junction induced in graphene. The graphene  $p$ - $n$  junction in our geometry (Fig. 4.8c) has a lateral size of  $\sim 20$  nm, determined at 30% of the electric field width in the  $p$ - $n$  junction, with an applied gate voltage at the level of  $\sim 1$  V.



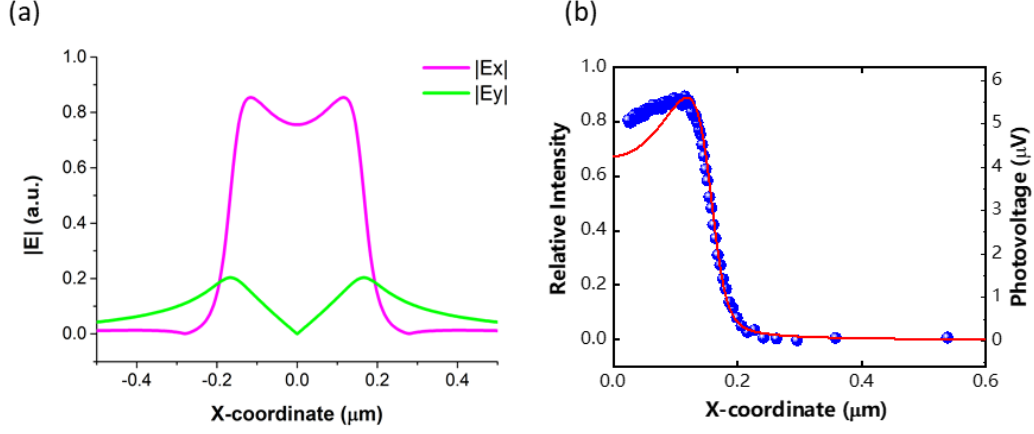


**Figure 4.14** Comparison of light field profiles with theory. (a) The line scan of the norm of electric field calculated at the graphene position. (b) Comparison of the simulated field intensity ( $E_x^2 + E_y^2$ ) profile in the plasmonic slot waveguide (the solid red line) with the reconstructed profile obtained with a p-n junction moved in graphene by gating (the blue circles).

The maximal photo-current produced in the graphene  $p$ - $n$  junction from FDTD modelling from section 4.5. To evaluate the photocurrent, the intrinsic quantum efficiency (the number of electrons produced by one photon) of graphene (in addition to the light power in the graphene  $p$ - $n$  junction) is necessary to be obtained. It is well established that at low light intensities, the graphene intrinsic quantum efficiency is equal to one<sup>38</sup>. This implies that the photocurrent can be estimated using the expression

$$I = \frac{P_{gr}}{\hbar\omega} e \text{ where } P_{gr} \text{ is the light power absorbed in the graphene } p\text{-}n \text{ junction, } e \text{ is the}$$

electron charge and  $\omega$  is the light frequency. Lumerical FDTD simulations give the power absorbed the in graphene  $p$ - $n$  junction at the position of the maximum field as  $P_{gr} \approx 2.2 \text{ nW}$ , which yields a photocurrent at the level  $I \approx 2.8 \text{ nA}$ , close to the measured values.

## 4.7 Conclusion

Relying on the interaction between graphene and plasmonic slot waveguide mode, we successfully demonstrated a graphene plasmonic modulator, featuring a modulation depth of 0.12 dB/ $\mu\text{m}$  at the gate voltage amplitude of 6 V. The operation speed of our device can be improved by optimizing the RC parameter of the device, which was not considered in our experiment. On the other hand, we have suggested and experimentally realized the electromagnetic field mapping based on the photo-detection with a  $p$ - $n$  junction induced and moved inside graphene by an external gate voltage. The spatial resolution of this electrical, rather than mechanical, scanning technique is determined by the  $p$ - $n$  junction width of  $\sim 20$  nm that can further be improved by decreasing the thickness of the gating dielectric or decreasing the temperature. The developed approach is demonstrated by mapping the electric field distribution of a strongly confined plasmonic slot-waveguide mode at telecom wavelengths, and the constructed mode profile with our approach was found in excellent agreement with numerical simulations. Our light mapping method could be used in nanoscale optical characterization that ensures extremely high spatial resolution and precision, offering at the same time promising opportunities for nanoscale plasmonic on-chip devices.

# Chapter 5

## An effect of dielectric fabrication techniques on graphene gating

*Gate hysteresis is one of the biggest challenges for achieving good performance of current graphene field-effect devices, including electro-optical modulators. The vast surface area of graphene gives it high sensitivity to the ambient surroundings and controllable electronic transport property, which at the same time leads to the high contact area between graphene and the dielectric layer. Could the gating dielectric have some effect on the gating hysteresis? What is the best dielectric to gate graphene for electro-optics? Based on this thought, we conducted our experiments in this chapter and obtained an interesting result. The related work<sup>190</sup> has been published in the Journal of Physical Chemistry C. I conducted most devices' fabrication and measurements work. Vasyl G. Kravets and Shinji Imaizumi helped with the XPS measurement and analysis. Shinji Imaizumi fabricated one of the devices and measured its transport characteristic. Alexander Grigorenko and I built the theoretical model of the positive and negative gate hysteresis process.*

### 5.1 Introduction

Graphene related science and technology has experienced dramatic progress since the first discovery of graphene in 2004<sup>1</sup>, due to its unique and inherent properties such as massless Dirac electrons<sup>191</sup> with high mobility, strong interaction with light<sup>38</sup>, and the possibility to firmly control its electrical<sup>191</sup>, optical<sup>192</sup>, plasmonic<sup>110, 193</sup>, and chemical<sup>194</sup>

properties by applying an electric field, which a simple electrical gating structure can achieve. Intrinsic graphene possesses naturally low carrier density, and a reasonably large electric field (at the level of 1 V/nm) on a gating dielectric material is essential to control graphene property if a gating structure is applied. Indeed, some dielectrics show a certain degree of conduction at a high electric field<sup>195</sup>. For electro-optics and optoelectrics such as graphene-based optical modulators<sup>196</sup> and photodetectors<sup>20</sup>, this issue becomes much more difficult, where the dielectric materials need to be transparent in the interest wavelength band. Therefore, an important question is raised: what is the best dielectric to gate graphene, especially for my research where a transparent material is needed?

The easiest way to apply an electric field on graphene is using an electrical gating structure, which has been widely investigated for graphene field-effect devices (GFETs)<sup>197, 198</sup>. One challenge for a graphene field-effect device's performance is the gating hysteresis, a frequent phenomenon when measuring graphene's transport characteristics. Electrical conduction of dielectric medium in graphene field-effect devices causes two types of hysteresis: positive and negative ones.<sup>199</sup> Charge transfer between trap sites in the dielectric layer and graphene caused the positive gating hysteresis in SiO<sub>2</sub> dielectric layer-based GFETs<sup>199</sup>. In electrolyte-gated GFETs, the negative gating hysteresis was observed, caused by the electrolyte's charge conduction.<sup>199</sup> A temperature dependence on the gate hysteresis direction was observed with a SiO<sub>2</sub> dielectric layer, explained by electrons and holes trapping.<sup>200</sup> The doping property of graphene and gating hysteresis of SiO<sub>2</sub> based GFETs was measured by in-situ Raman spectroscopy, revealing that the H<sub>2</sub>O/O<sub>2</sub> redox couple at the interface of graphene and the dielectric layer could become the charge trap source<sup>201</sup>.

Considering the hysteresis effect: what is the best material to gate graphene electro-optical devices for our projects? In this chapter, we demonstrate that this question is inaccurate because a dielectric material produced by different manufacturing methods shows significantly different gating characteristics, resulting in different gating hysteresis. We show this effect by using two widely-used dielectric materials, hafnia ( $\text{HfO}_2$ ) and alumina ( $\text{Al}_2\text{O}_3$ ), which are transparent for telecom bands. We found that the gating dielectric fabrication method can profoundly influence its gating properties. Oxide dielectrics (hafnia and alumina) prepared by atomic layer deposition (ALD) show a positive gate hysteresis, but the same medium prepared by electron beam (e-beam) evaporation exhibits a negative hysteresis of the graphene gating characteristics. Based on the X-ray photoelectron spectroscopy (XPS) and our modeling, we attribute this phenomenon to the stoichiometry difference and oxygen ion migration inside the dielectric samples. Both two hystereses are undesirable in actual practice, indicating that oxide dielectrics better be avoided for practical room temperature-based graphene gating devices.

## 5.2 Device structure and fabrication methods

Figure 5.1a displays our sample's general structure. A piece of contacted CVD graphene is located on a dielectric layer, fabricated on top of a narrow (300  $\mu\text{m}$  wide) gold strip with a 50 nm thickness, which is the bottom gate contact. Quartz works as the substrate for our structure, which is transparent for optical measurements. The bottom gold stripe has a much smaller thickness than that of the dielectric layer, about 200 nm, which avoids the leakage from the cracks at the edge of the bottom gold stripe to the top contacts<sup>202</sup>. We used Raman spectroscopy to check our graphene's monolayer property (purchased from 2D semiconductor company). We tested two different oxide

dielectrics ( $\text{HfO}_2$  and  $\text{Al}_2\text{O}_3$ ) in our gating experiment, fabricated by two different manufacturing methods: atomic layer deposition (ALD) and electron beam (e-beam) evaporation. Figure 5.1b shows an optical image of a device.

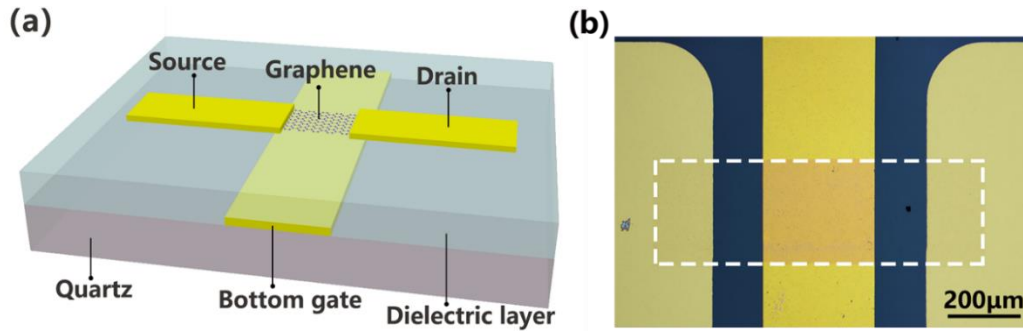


**Figure 5.1** (a) The structure schematic of all measured graphene field-effect devices. (b) Optical image of our device: a piece of CVD graphene on the e-beam evaporated  $\text{Al}_2\text{O}_3$  above the Au stripe. The white dashed rectangle refers to the piece of CVD graphene.

To fabricate our device, we first performed photolithography and electron beam evaporation of 3 nm Cr and 50 nm Au to deposit 300  $\mu\text{m}$  wide thick Au stripes on the quartz substrate. Plasma etching proved helpful in enhancing the adhesion between the photoresist and quartz substrate. Then 200 nm thick dielectric material was deposited on the substrate by either ALD or e-beam evaporation. Section 2.1.4 explained electron beam evaporation (e-beam) and atomic layer deposition (ALD). For this device, e-beam evaporations were carried out in the Moorfield system at a deposition speed of about 0.6  $\text{\AA}/\text{s}$ . For the ALD process,  $\text{Al}_2\text{O}_3$  or  $\text{HfO}_2$  dielectrics were fabricated at 300°C in the ALD chamber (Oxford Instruments Inc.), using trimethylaluminum (TMA) and  $\text{H}_2\text{O}$  as precursors (for  $\text{Al}_2\text{O}_3$ ) or Tetrakis(ethylmethlamido)hafnium (TEMAH) and  $\text{O}_2$  - precursors at 300°C for  $\text{HfO}_2$  without post-deposition annealing.

CVD graphene was then wet-transferred on the dielectric material (see section 2.1.1 for details of the wet-transfer process). Photolithography with a negative photoresist and

oxygen plasma (to remove graphene uncovered by the photoresist) was used to pattern graphene. After removing the photoresist, only graphene stripes that were patterned remained above the Au stripe. Final processes of photolithography, e-beam evaporation, and lift-off were used to make 50 nm thick Au contacts to graphene, working as the electrical source and drain. During the whole process, 2 nm titanium was always deposited before the deposition of gold film, which improves the adhesion of thin gold to the substrate.

### 5.3 Positive and negative gating hysteresis

Previous works devoted to the gating of graphene devices demonstrated two archetypal gating hysteresis behaviors: positive and negative ones, defined by the displacement of the induced charge-neutral point (CNP) during the sweeping process of the gate voltage<sup>199, 203</sup>. Positive hysteresis is displayed in Figure 5.2a. Suppose the graphene sample is originally undoped with  $V_{\text{CNP}} = 0$ . The forward sweeping (from negative to positive voltages) will cause the shift of CNP to negative voltages. Meanwhile, the backward sweeping (from positive to negative voltages) will display the shift of CNP to the positive voltages. Figure 5.2b explains the negative hysteresis of undoped graphene, where the situation is exactly the opposite. The forward sweeping (from negative to positive voltages) will cause the shift of the CNP to positive voltages, and the backward sweeping (from positive to negative voltages) will show the shift of CNP to the negative voltages.

For a positive hysteresis, the CNP voltage of the backward sweeping is always greater than that of the forward sweeping, while the CNP voltage of the backward sweeping in a negative hysteresis is smaller than that of the forward sweeping. This indicates that in a positive hysteresis, graphene loses the charge generated by the applied gate voltage

during the sweeping process (shifting the CNP voltage closer to the applied voltage position). Therefore, the positive hysteresis of undoped graphene samples can be described by the decrease of the dielectric layer capacitance during the sweeping process.

Respectively, for a negative hysteresis, graphene increases the charge induced by the gate voltage during the sweeping process (shifting the CNP voltage further away from the applied voltage position). Therefore, the negative hysteresis of undoped graphene samples can be described by the increase of the dielectric layer capacitance during the sweeping process<sup>204</sup>.

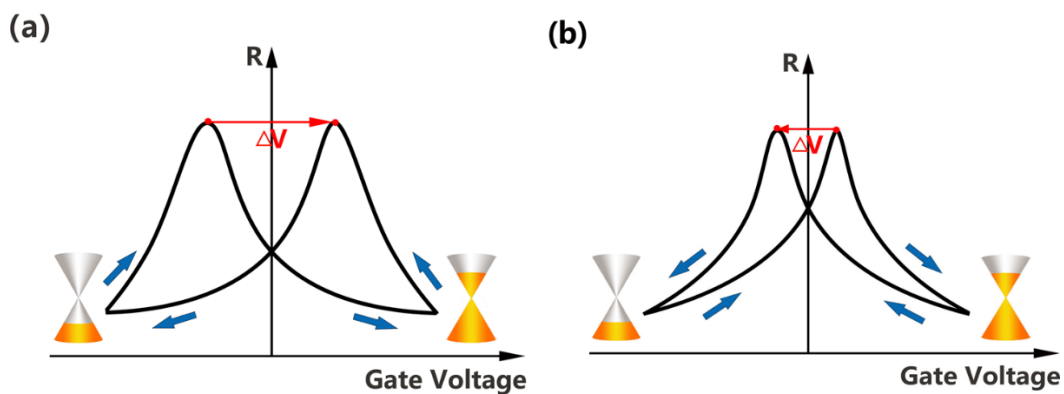


**Figure 5.2** Schematics of the gate voltage-dependent conductance hysteresis suppose graphene is undoped originally. (a) and (b) refers to positive and negative hysteresis, respectively. The Blue arrow points to the direction of the gate voltage sweeping process. Arrow pointing right indicates a forward sweeping, and pointing left indicates a backward sweeping. The highest redpoint with the largest resistance value is the charge neutral point (CNP) of graphene, where it is undoped. Graphene is p-doped in the left region of CNP and n-doped in the right region of CNP.



## **5.4 Dependence of graphene gating characteristics for four samples with dielectrics fabricated by ALD and e-beam evaporation**

The dependence of graphene gating properties on the dielectric layer manufacturing method was shown in Figs. 5.3 and 5.4, which are our main experimental results. Namely, graphene devices' conductance characteristic with atomic layer deposited (ALD) oxide dielectric shows obvious positive gating hysteresis while it exhibits negative hysteresis when the same dielectric material is deposited by electron beam evaporation (e-beam) method. For all the measurements, the gate voltage was applied to the bottom Au while graphene was grounded. To limit water absorption's influence during the whole measurement process, the device was either placed in vacuum or the air while graphene was protected with a thick PMMA layer ( about 200 nm). Therefore, the hysteresis effect mainly resulted from the interaction between graphene and the dielectric, except for the original residues' impact on graphene<sup>205</sup>.

The gating hysteresis of graphene devices with dielectric  $\text{HfO}_2$  and  $\text{Al}_2\text{O}_3$  is plotted in Figs. 5.3a and b, with both atomic layer deposition (ALD) made separators in the gating structure. We can see that the CNP voltage of the backward sweeping is much larger than that of the forward sweeping with a pronounced positive hysteresis of the graphene gating. The CNP values shift closer to the maximal applied voltage, which is similar to previously reported hysteresis effects in similar graphene field-effect devcies<sup>199, 202</sup>. For the thorough process, we have a sweeping speed at several V/min. For both ALD  $\text{HfO}_2$  and  $\text{Al}_2\text{O}_3$  graphene devices, we observed the saturation of the “distance” between the maximal applied voltage and CNP voltage, which saturation of the induced charge in graphene no matter how large the gate voltage is (10 V for ALD  $\text{HfO}_2$  and 18 V for ALD  $\text{Al}_2\text{O}_3$ ). Besides, we observed a resistance increase at a fixed applied gate voltage

with time for both graphene devices with ALD dielectrics, as another proof of the positive hysteresis. This implies that the gate voltage-induced charge in graphene decreases with time to the value below the expected one determined by the geometrical capacitance (see Figure 5.9, measured at non-continuous sweeps), which is also revealed by the discontinuity in Figure 5.3a at the ends of the sweep. We observed an obvious decrement of the graphene resistance, where we stopped for several minutes when it is stable before the next forward and backward sweeping.

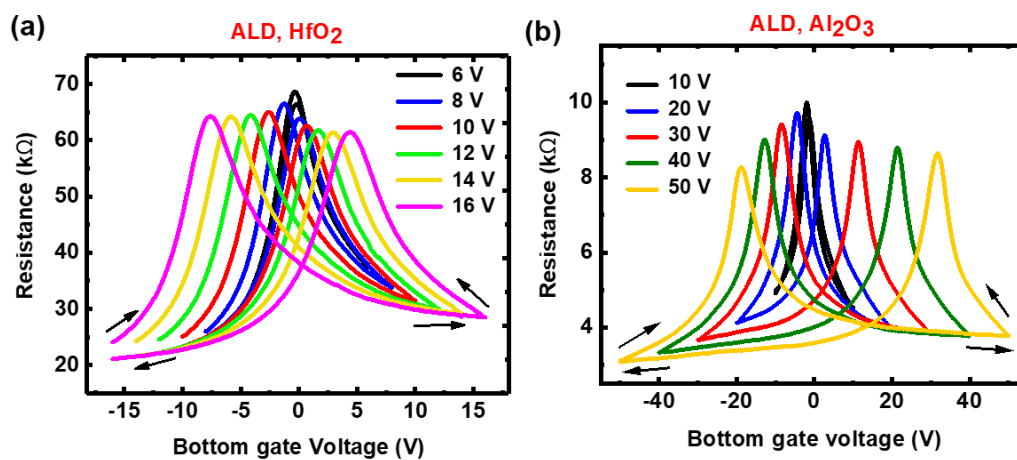


**Figure 5.3** Conductance hysteresis of graphene devices with ALD dielectric material in respect of the gate voltage. The legend value inside means the sweeping range of the gate voltage (maximal gate voltage value during the sweeping process). For each sweeping loop, the gate voltage starts from a maximal negative voltage to the maximal positive voltage and then comes back. (a) Positive hysteresis measured in vacuum with ALD HfO<sub>2</sub>. The thickness of HfO<sub>2</sub> is 200 nm. The sweeping speed is 3 V/min. (b) Positive hysteresis measured in vacuum with ALD Al<sub>2</sub>O<sub>3</sub>. The thickness of Al<sub>2</sub>O<sub>3</sub> is 170 nm. The sweeping speed is 1.8 V/min. The dependence of the hysteresis on the sweeping speed will be discussed in section 5.7.

Contrary to the positive hysteresis shown in graphene devices with ALD dielectric layers, graphene devices with e-beam evaporated dielectrics displayed distinct negative hysteresis (see Figures 5.4a and b). Figures 5.4a and 5.4b present the hysteresis curves

of graphene devices with dielectric  $\text{HfO}_2$  and  $\text{Al}_2\text{O}_3$ , fabricated by e-beam evaporation, respectively. In both cases, the negative hysteresis of graphene devices with e-beam dielectric samples was less pronounced than the positive hysteresis of ALD hafnia and alumina. For e-beam fabricated samples, this value was not large compared to ALD samples (see the gate voltage sweeping range in Figures 5.3 and 5.4). Indeed, in our experiments, the dielectric films produced by the ALD method were more electrically stable than e-beam fabricated dielectrics and had a longer service life with larger gate voltages applied. The maximal gate voltages shown in Figures 5.3 and 5.4 were close to the breakdown thresholds of the dielectrics to obtain the maximum hysteresis performance for each device. For all measurements, the leakage current through the dielectrics kept less than 1 nA, which ensures the typical dielectric performance. The resistance value in each graph is different with different graphene geometry in each device. In addition, although the CVD graphene for all samples comes from the same batch, distinct p-doping of graphene was observed in devices with e-beam samples, compared to the relatively undoped situation in graphene devices with ALD samples.

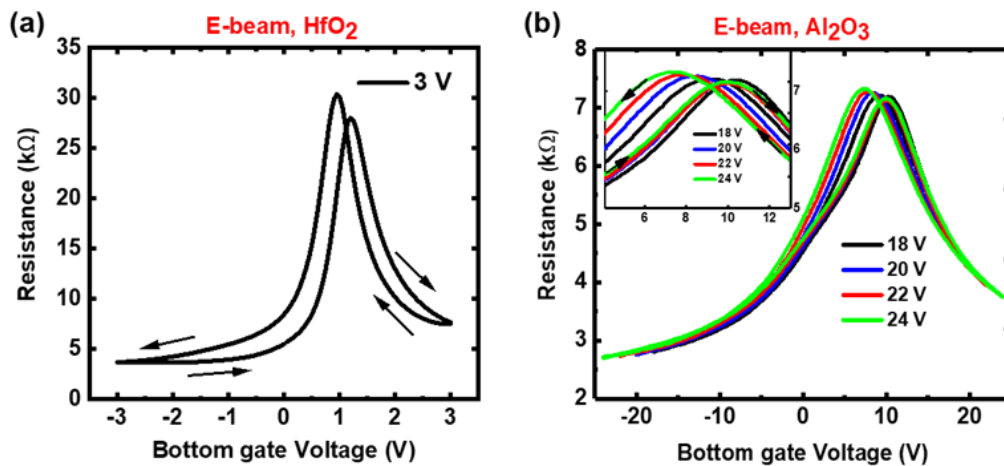


**Figure 5.4** Hysteresis for graphene devices with e-beam dielectric material in respect of the gate voltage. The legend value inside means the gate voltage sweeping range (maximal gate voltage value during the sweeping process). For each sweeping loop, the gate voltage starts

from a maximal negative one to a maximal positive one and then comes back. (a) Negative hysteresis for graphene device with e-beam  $\text{HfO}_2$ <sup>84</sup>. The thickness of  $\text{HfO}_2$  is 175 nm. The sweeping speed is 3 V/min. (b) Negative hysteresis measured in vacuum for graphene device with e-beam  $\text{Al}_2\text{O}_3$ . The thickness of  $\text{Al}_2\text{O}_3$  is 230 nm. The sweeping speed is 3 V/min. The inset picture shows a manifested CNP region.

## 5.5 XPS analysis of the dielectrics' properties

As mentioned in section 5.1, a positive hysteresis usually exists in the gating effect of graphene field-effect device with an oxide dielectric layer<sup>199, 206, 207</sup>, and the negative hysteresis is usually measured in the electrolyte-gated graphene field-effect devices<sup>199</sup>. However, our investigation in section 5.4 shows that the specific result of gating hysteresis in graphene field-effect devices depends on the dielectrics' fabrication method, where a positive hysteresis was measured in ALD fabricated graphene devices and a negative hysteresis was observed in e-beam fabricated graphene devices with the same dielectric material. Therefore, we conducted X-ray photoelectron spectroscopy (XPS, see section 2.2.4 for details) to analyze the elemental composition of our fabricated dielectric materials, with results shown in Figures 5.5a-h, in order to further understand the unusual dependence of graphene gating characteristics on the fabrication methods and study the intrinsic difference of the dielectric films deposited by ALD and e-beam methods.

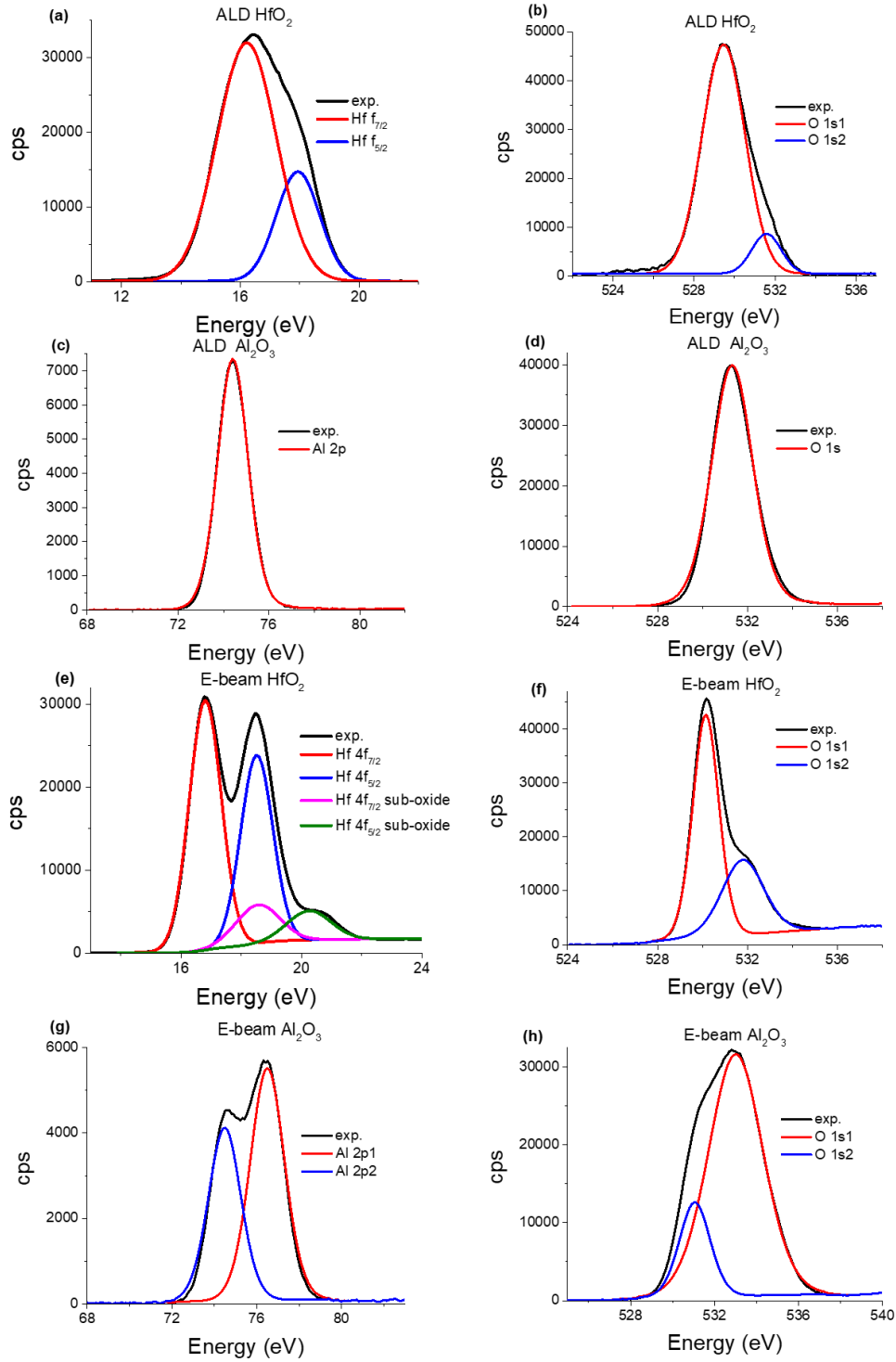


**Figure 5.5** X-ray Photoelectron Spectroscopy (XPS) result of ALD and e-beam fabricated  $\text{HfO}_2$  and  $\text{Al}_2\text{O}_3$  in our experiments. The black curves in each figure represent the captured photo-emitted electron numbers per second in the XPS measurement process. (a,b) Fitted XPS spectra of ALD  $\text{HfO}_2$ . (c,d) Fitted XPS spectra of ALD  $\text{Al}_2\text{O}_3$  (e,f) Fitted XPS spectra of e-beam  $\text{HfO}_2$ . (g,h) Fitted XPS spectra of e-beam  $\text{Al}_2\text{O}_3$ .

The difference between the peak number and positions in the XPS spectra of ALD and e-beam made  $\text{HfO}_2$  and  $\text{Al}_2\text{O}_3$  films is directly demonstrated in Figure 5.5. Figures 5.5a,b and 5.5c,d show the de-convoluted XPS spectra measured on  $\text{HfO}_2$  and  $\text{Al}_2\text{O}_3$  films made by ALD method. For  $\text{Al}_2\text{O}_3$  films prepared by ALD, the fitted Al and O peaks are consistent with previously reported values<sup>136, 137</sup>. The peak positions of Al 2p and O 1s are located at 74.3 eV and 531.3 eV, respectively. For  $\text{HfO}_2$  films prepared by the ALD method, we could observe the Hf 4f<sub>7/2</sub> peak at 16.2 eV and O 1s peak at 529.5 eV, also consistent with the values for  $\text{HfO}_2$  in the literature<sup>137, 208, 209</sup>.

Figures 5.5e,f and 5.5g,h show the de-convoluted XPS spectra measured on  $\text{HfO}_2$  and  $\text{Al}_2\text{O}_3$  films fabricated by e-beam evaporation. A prominent difference between the spectra of e-beam and ALD film is the spectra complexity. Meanwhile, O 1s peak shifts from 531.3 eV for ALD  $\text{Al}_2\text{O}_3$  to 533 eV for e-beam  $\text{Al}_2\text{O}_3$  and 529.5 eV for ALD  $\text{HfO}_2$  to 530.2 eV of e-beam  $\text{HfO}_2$ <sup>210</sup>, where we deduce the presence of oxygen vacancies in e-beam films. Besides, for e-beam fabricated  $\text{HfO}_2$  films, its XPS spectra display peak position shifts for Hf 4f<sub>7/2</sub> and Hf 4f<sub>5/2</sub> peaks at 16.8 eV and 18.5 eV to 16.2 eV and 18.0 eV for those of ALD fabricated structures, which could also be related to the presence of oxygen deficiencies, which is most probably responsible for the super-capacitance property of e-beam fabricated  $\text{HfO}_2$  and  $\text{Al}_2\text{O}_3$ . In fact, a graphene device with e-beam  $\text{HfO}_2$  shows a huge super-capacitance effect in our previous research<sup>84</sup>. Besides, it is established that dielectric property of  $\text{HfO}_2$  is much worse in high electric fields (reaching more than 10  $\mu\text{A}$  leakage current)<sup>84, 211</sup>, and oxygen vacancies in  $\text{HfO}_2$  were proved to control charge carriers' phonon-assisted tunneling recently, which leads to the electrical conductivity.<sup>212</sup> Experiments also confirm the existence of hole trapping in amorphous  $\text{HfO}_2$  and  $\text{Al}_2\text{O}_3$ .<sup>213</sup>

## 5.6 Discussion

It can be seen from the XPS spectra that e-beam films hold a much more complex stoichiometry and presence of oxygen vacancies, which provides us some clues to analyze the different gating hysteresis attributed to different dielectrics fabrication methods. Indeed, in our experiments, ALD films have higher electrical stability and lower electric conductivity. Therefore, we conclude the gating hysteresis is connected to the surface effects which arise at the interface of graphene and the dielectric film. Figure 5.6 depicts our theory.

Figure 5.6a shows our explanation of the positive hysteresis for graphene devices with ALD dielectric. In this case, charge transfer occurs from the graphene flake to the trap centers in the oxide dielectric layer throughout the graphene/dielectric interface during the gate sweeping process. This charge transfer behavior reduces the charge induced in graphene below the expected value of the geometrical capacitance, which results in a positive gating hysteresis, as analyzed in section 5.3. The hysteresis asymmetry observed in Figures 5.3a, b originates from the different characteristics of electron and hole trapping in the ALD-made dielectric layers.

Figure 5.6b shows the negative hysteresis for graphene devices with e-beam fabricated dielectrics. For e-beam oxides, we considered the existence of non-lattice oxygen in the films from the XPS result. Under the high electric gating field, mobile oxygen ions could be formed in the dielectric layer. Due to the film's amorphous structure, the conducting positive and negative ions in the film could move freely, which leads to the so-called “solid-state electrolyte” effect<sup>84</sup>. These ions eventually form an electrical double layer at the interface of graphene and the dielectric layer with time, building a locally enhanced electric field underneath graphene. This local electric field boosts the

charge induced in graphene to the value higher than that determined by the geometrical capacitance, resulting in negative gating hysteresis as analyzed in section 5.3. Indeed, the super-capacitance effect of e-beam deposited  $\text{HfO}_2$  was reported in our previous work, holding a significantly larger capacitance and slower time response regarding the geometrical dielectric capacitance with the same thickness.<sup>84</sup>

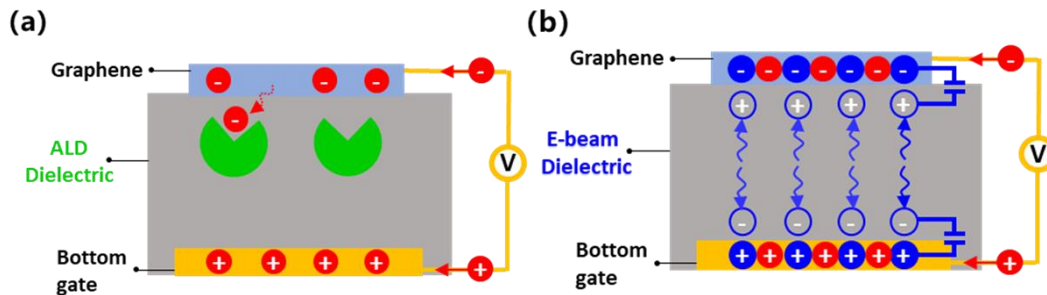


**Figure 5.6** Contrasting mechanisms for graphene conductance gating hysteresis effect with ALD or e-beam fabricated dielectric layers: (a) Charges traps at the interface of graphene and the ALD dielectric layer absorb electrons/holes in the capacitance charging process. (b) The electrical double layer forms around the e-beam dielectric edge during the charging, which locally advances the dielectric capacitance and corresponding carrier numbers in graphene.

## 5.7 Dependence of graphene gating characteristics on sweeping range and speed

We also measured the hysteresis value's dependence on the gate voltage sweeping range and speeds to check the time scale of the gating hysteresis process. As shown in Figure 5.7a, the larger sweeping range presents a more significant hysteresis in ALD  $\text{HfO}_2/\text{Al}_2\text{O}_3$  and e-beam  $\text{Al}_2\text{O}_3$  devices. A larger sweeping range means a longer sweeping time since the sweeping speed was fixed in the measurements. In this case, a longer sweeping time contributes to more carriers' decrease in graphene in the charge trapping process or more carriers' increase in graphene in the double-layer capacitance



forming process. It is worth noting that the dependence of the gating hysteresis on the sweeping range for e-beam fabricated  $\text{Al}_2\text{O}_3$  was relatively small, which reveals the gate voltage's insignificant effect on the forming of the electrical double layer, with the limited gate voltage due to the dielectric breakdown of e-beam  $\text{Al}_2\text{O}_3$  film.

Figure 5.7b shows the dependence of the gating hysteresis on the sweeping speed. The increasing sweeping speed causes a decreasing hysteresis in graphene devices with ALD fabricated  $\text{HfO}_2$  and  $\text{Al}_2\text{O}_3$ . In this case, a faster sweeping speed results in a shorter sweeping time at a fixed sweeping range in our experiments, which reduced graphene's interaction time with charged traps in the dielectric layer, leading to a smaller decrease of the induced charge in graphene and resulting in a smaller hysteresis. Interestingly, we still observed the hysteresis effect when we used the highest sweeping speed of 80 V/min in our ALD devices, although the absolute hysteresis value became very small. For the half of the sweeping process with a gate voltage sweeping range of 16 V, the sweeping is close to ~20 seconds. If we consider one specific type of charge (electron/hole) trapping for the half-sweeping process, its time scale should be less than 20 s. It is worth noting that this measurement was conducted at room temperature while the hysteresis effect became less pronounced at lower temperatures and disappeared almost entirely at -50 °C, shown in Figure 5.10.

The dependence of graphene gating hysteresis on the devices' gate-sweeping speed with e-beam fabricated dielectrics is more complicated than those with ALD dielectrics. Starting with a positive hysteresis, the gating hysteresis becomes negative and then positive as the sweeping speed increases for the e-beam  $\text{Al}_2\text{O}_3$  graphene device. For the graphene device with e-beam  $\text{HfO}_2$ , the positive hysteresis value raises as the gate-sweeping speed increases, but with a small negative hysteresis at first, shown in the inset of Figure 5.7b. The abnormal trends for e-beam devices suggest both charge

trapping effect and the double-layer capacitance effect could work and cooperate in graphene field-effect devices with e-beam dielectrics.<sup>199</sup> If the gate-sweeping speed is very slow, the charge trapping effect is prominent, leading to a decreasing trend (for e-beam  $\text{Al}_2\text{O}_3$  device in Figure 5.7b) or even a positive hysteresis (for both e-beam  $\text{Al}_2\text{O}_3$  and  $\text{HfO}_2$  devices in Figure 5.7b). Interestingly, when the sweeping speed of the gate voltage was exactly 5 V/min, no hysteresis was observed for the graphene device with e-beam fabricated  $\text{Al}_2\text{O}_3$ , suggesting that the double-layer capacitance effect and charge trapping effect cancel each other at this speed.

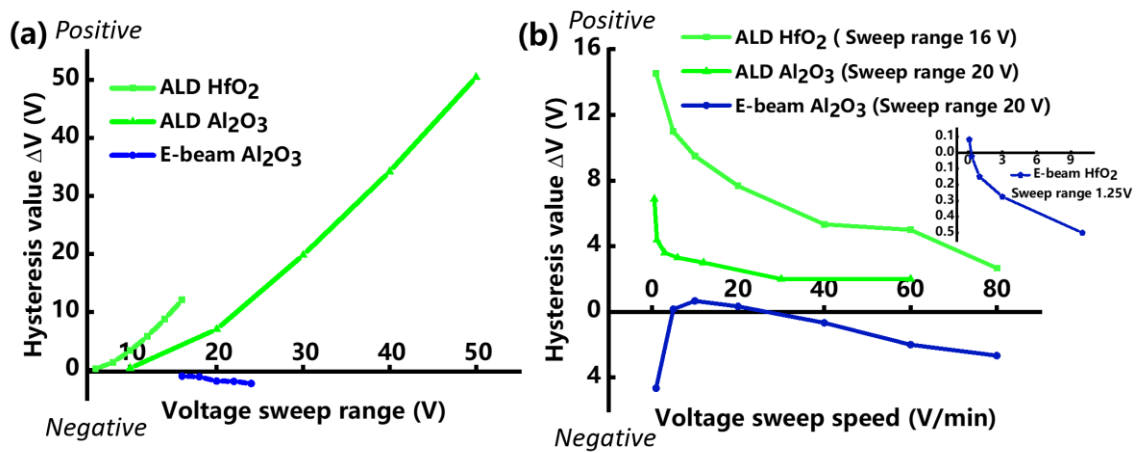


**Figure 5.7** (a) Extractive data from Figures 5.3a, b, and 5.4b shows the dependence of gating hysteresis on the gate-sweeping range for graphene devices with ALD  $\text{HfO}_2$  and ALD/e-beam  $\text{Al}_2\text{O}_3$  dielectrics. (b) Dependence of gating hysteresis on the gate-sweeping speed for graphene devices with ALD/e-beam  $\text{Al}_2\text{O}_3$  and  $\text{HfO}_2$  dielectrics. The value above x-axis means positive hysteresis, and below x-axis means negative hysteresis.

## 5.8 Gate-induced electron density measured with the help of FTIR spectroscopy

Based on the carrier density model of graphene<sup>37</sup>, analyzing the gate voltage-dependent resistance curve of graphene is widely used to calculate the electron/hole density

induced by an applied gate voltage in graphene. In our results above, the actual carrier density in graphene affected by the gate voltage differs from the actual applied voltage, and the contact resistance and the current flowing in the dielectric layer also need to be considered. Therefore, graphene's resistance-voltage characteristics at room temperature should be treated carefully to evaluate its carrier density.

Optical measurements provide another clue to evaluate the unambiguous electron density numbers in graphene. We measured the gate voltage-dependent optical spectra of graphene devices with Al<sub>2</sub>O<sub>3</sub> dielectrics produced by e-beam and ALD methods separately. Both dielectric layers have a thickness of 170 nm. The results are shown in Figures 5.8a, b. It can be seen that the peak observed at -20 V gate voltage of the graphene device with e-beam Al<sub>2</sub>O<sub>3</sub> dielectric is spectrally close to the peak of the ALD Al<sub>2</sub>O<sub>3</sub> graphene device at -70 V gate voltage. The Fermi level of graphene<sup>31</sup> is given by

$$E_F = \hbar v_F \sqrt{\pi n} = \hbar v_F \sqrt{\pi \frac{CV}{e}} \quad (5.1)$$

where  $\hbar$  is the Plank constant,  $v_F$  is the Fermi velocity, taken as  $10^6$  m/s.  $C$  is the dielectric capacitance per unit area, and  $V$  is the gate voltage for an undoped graphene sample. Thus, a rough estimation of the capacitance from the Fermi energy and the gate voltage can be obtained as follows.

$$C = \frac{E_F^2 e}{V \hbar^2 v_F^2 \pi} \quad (5.2)$$

By fitting the theoretical optical response (based on the peak positions) of both devices in Figures 5.8c, d to the experimental reflectance spectra in Figures 5.8a, b, we estimated that the capacitance of an e-beam Al<sub>2</sub>O<sub>3</sub> is  $6.4 \times 10^{-4}$  F/m<sup>2</sup> and the capacitance of ALD Al<sub>2</sub>O<sub>3</sub> is  $3.1 \times 10^{-4}$  F/m<sup>2</sup>. With the same thickness, the capacitance of e-beam

AL<sub>2</sub>O<sub>3</sub> is around 2 times larger than that of ALD Al<sub>2</sub>O<sub>3</sub>. The fitting is not accurate but gives a rough range of the capacitance of e-beam and ALD fabricated Al<sub>2</sub>O<sub>3</sub>.

The standard parallel plane capacitance per unit area is defined as

$$C = \frac{\epsilon_r \epsilon_0}{d} \quad (5.3)$$

where  $d$  is the dielectric thickness,  $\epsilon_r$  is the relative permittivity. The dielectric constant of Al<sub>2</sub>O<sub>3</sub> with a 170 nm thickness is 7.6 based on the reference<sup>214</sup>, which corresponds to a geometrical capacitance per unit area of  $4 \times 10^{-4}$  F/m<sup>2</sup>. This value is located between that of our deposited Al<sub>2</sub>O<sub>3</sub> by ALD and e-beam methods, respectively.

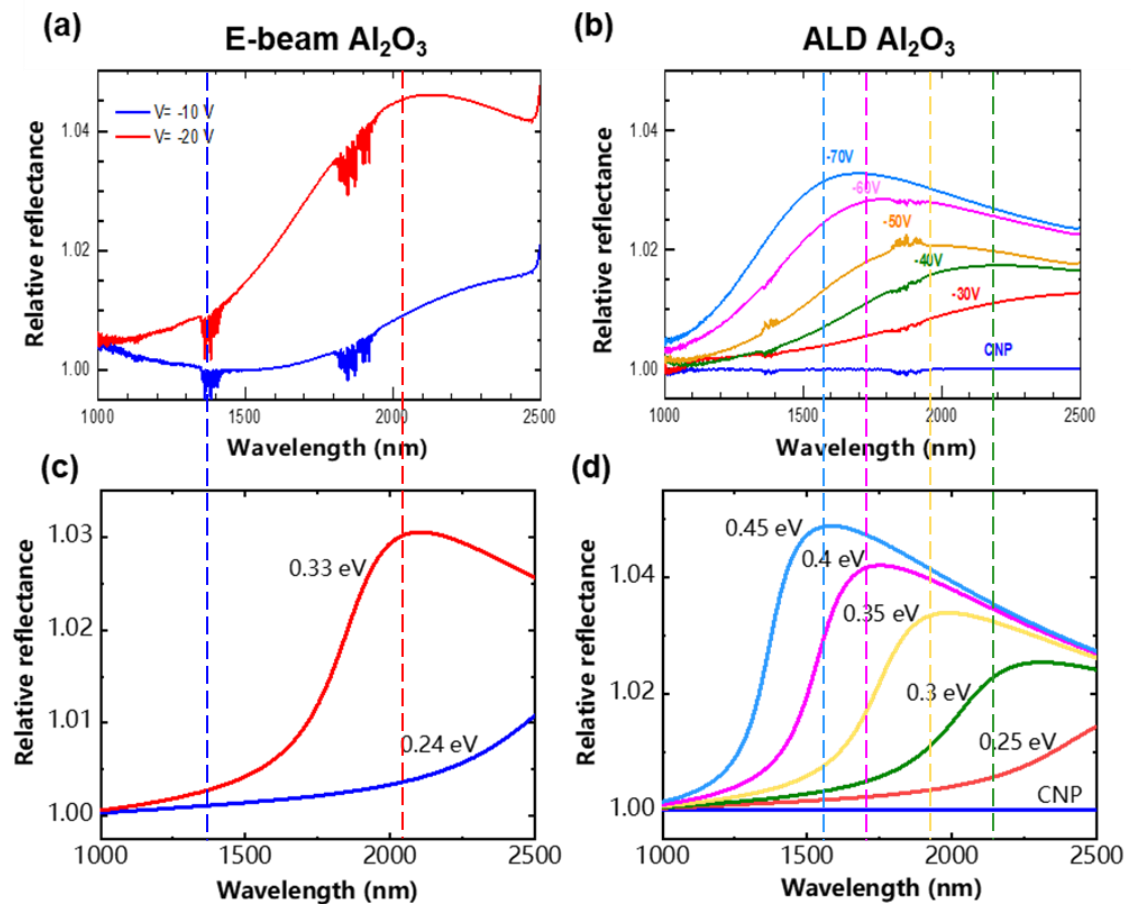


**Figure 5.8** Relative optical reflection spectra of graphene devices (normalized by the reflection at zero gate voltage) under different gate voltages with alumina dielectrics produced by (a) an e-beam method (b) an ALD method. The spectra were measured by FTIR spectroscopy with a

Bruker Vertex 80 system and a Hyperion 3000 microscope. Simulations of the relative reflection of our device at different Fermi energies for alumina produced by (c) the e-beam method (d) the ALD method.

## **5.9 Hysteresis at non-continuous sweeps and temperature dependence**

For the hysteresis curves in Figures 5.3 and 5.4, we used a continuous sweep of a gate voltage in the measurement process. To check the gating effect at a fixed voltage, we performed non-continuous sweeps for our device, where we especially stopped at the maximal positive and minimal negative gate voltage for some time. The corresponding resistance curve for the graphene device with an ALD HfO<sub>2</sub> dielectric separator layer is shown in Figure 5.9. Surprisingly, the graphene resistance increased at both ends of the gate voltage sweepings, where we stopped for three to five minutes until the value was stable before the next forward/backward sweeping. This indicates that graphene is still losing charge to the trapping sites even when the gate voltage is fixed. Also, the resistance increments are larger at the positive gate voltage ends than that at the negative ends, which suggests the speed of electron trapping is faster than that of hole trapping. A similar phenomenon was previously reported in a graphene mica dielectric field-effect device by varying the charging time at the positive and negative ends of the gate voltage sweeping<sup>203</sup>.

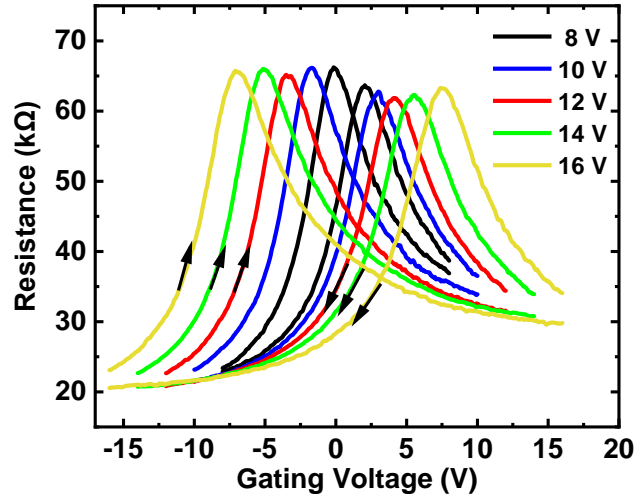


**Figure 5.9** Graphene gating effect measurement with ALD HfO<sub>2</sub> dielectric layer under different bottom gate voltages. The device was measured in vacuum five times at different voltage ranges. All of them started from negative voltages, sweeping to positive voltages, and stopped for several minutes until the graphene resistance value indicated from the lock-in amplifier was stable, then swept back to negative voltages.

On the other hand, if the gating hysteresis in ALD oxide dielectric films relies on a (thermally) excited charge transfer from graphene to the trapping sites, the hysteresis effect should become less pronounced when the temperature decreases. Figure 5.10 shows the temperature's impact on the hysteresis effect in the ALD Al<sub>2</sub>O<sub>3</sub> graphene device, which proved our thought. With a specially low sweeping speed of only 0.01 V/s, no significant gating hysteresis was observed at a low temperature of -50°C. Therefore, low-temperature conditions could be used to suppress the gating hysteresis in graphene devices.

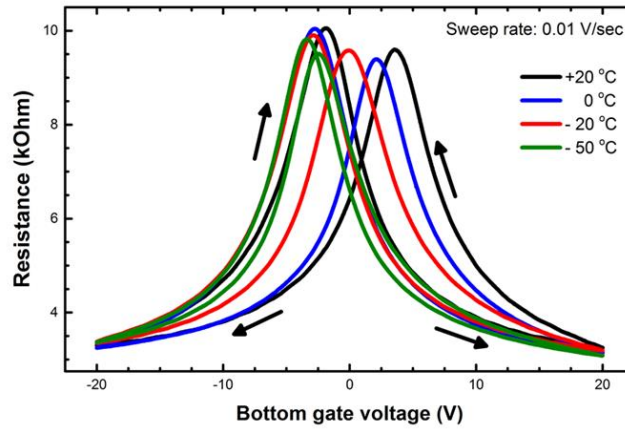


**Figure 5.10** Temperature dependence of hysteresis for ALD Al<sub>2</sub>O<sub>3</sub> graphene device.

## 5.10 Conclusion

For a 2D material-based electro-optical modulator, gating is an easy and essential method to affect the electrical, optical, and chemical properties of 2D material like graphene. This requires reasonably large fields applied over a dielectric gating material. Most dielectrics display some conduction in these fields, which raises an important question: what is the best dielectric to gate graphene, especially for electro-optical devices. We demonstrate that this question is imprecise in this Chapter because the dielectric mediums from different fabrication methods could behave significantly different gating performances. We investigated the dielectric properties of two widely-used dielectric materials, hafnia (HfO<sub>2</sub>) and alumina (Al<sub>2</sub>O<sub>3</sub>), fabricated by atomic layer deposition (ALD) and e-beam evaporation separately. It was found that oxide dielectrics made by atomic layer deposition (ALD) showed a pronounced positive gating hysteresis of graphene transport characteristics. But the same dielectrics produced by the e-beam evaporation method displayed mostly negative hysteresis. From XPS analysis, we attributed this behavior to the samples' stoichiometry and ion migration in the dielectric layers. Our results advise that oxide dielectrics better be avoided in graphene field-effect devices that work at room temperature. On the other

hand, methods have been reported to suppress the gating hysteresis effect. The gating hysteresis effect in GFETs can be significantly reduced by annealing and vacuum treatment<sup>215, 216</sup>. An HMDS surface treatment can reduce the doping level and suppress the hysteresis effect<sup>217</sup>. These processes are also helpful for our gating devices.



# Chapter 6

## Conclusions and outlook

This thesis investigates the integration of 2D material and nanostructures, aiming to study the light-matter interaction and practical applications. A Fabry-Perot (FP) MoS<sub>2</sub> and a graphene plasmonic waveguide modulator have been proposed and realized with high modulation depth. Meanwhile, with the facility of our designed structures, we have studied the gate-controllable optical properties of monolayer MoS<sub>2</sub> and gate-controllable light field distribution in graphene. With the latter one, we could achieve a 20 nm scale nanoscale light field imaging. Lastly, we studied the dielectric performance of two widely-used dielectric materials, hafnia and alumina (HfO<sub>2</sub> and Al<sub>2</sub>O<sub>3</sub>), with a simple graphene field-effect structure and found that the fabrication techniques could influence their dielectric properties.

The resonance introduced by the Fabry-Perot (FP) structure was verified to enhance the interaction between light and MoS<sub>2</sub> significantly. In Chapter 3, we fabricated a visible electro-optical modulator based on an FP structure with monolayer MoS<sub>2</sub>, Si<sub>3</sub>N<sub>4</sub> dielectric, and bottom Au as the gating contact and the reflecting mirror of the FP cavity. Our modulator showed a 6 dB modulation depth at an 80-degree incident angle for s-polarized light at the visible range, which is among the best for MoS<sub>2</sub> based optical modulators<sup>22, 25, 156</sup>. The modulation is mainly located at the excitonic band of monolayer MoS<sub>2</sub>, attributed to the combination of the gate voltage-induced refractive index change of MoS<sub>2</sub> monolayer and the optical resonant features of the FP structure. The modulation with p-polarized light was also studied, which performance was not as

good as the s-polarized light modulation. Besides, we first extracted the gate voltage-dependent complex refractive index of monolayer MoS<sub>2</sub> by analyzing the ellipsometric spectra and modeling. It was found that the absorption coefficient  $k$  of monolayer MoS<sub>2</sub> is gate-dependent at the excitonic wavelength range from 550 to 700 nm. A model based on the transfer matrix and the extracted refractive index was built, and the simulated results matched the experimental results well.

A graphene plasmonic modulator was proposed and demonstrated in Chapter 4, based on the interaction between graphene and the transmitted gap surface plasmon (GSP) mode in the plasmonic slot waveguide. The mechanism is to control the absorption of graphene by the electrical field with a gating structure and a thin high- $k$  dielectric HfO<sub>2</sub> layer. Graphene is located underneath the middle of the waveguide structure. By changing the amplitude and offset of the input AC gate voltage, the modulation depth can be enhanced, reaching 12% in our sample with a piece of 4  $\mu\text{m}$  graphene at a 6 V gate voltage, which corresponds to a modulation depth of 0.12 dB/ $\mu\text{m}$ , comparable to the latest reported value with graphene<sup>34, 169</sup>. On the other hand, we firstly detected a plasmonic wave-induced electrical signal between the source and drain area of graphene. Based on this property, we suggested and experimentally realized a novel electromagnetic field mapping method based on the photo-detection with a p-n junction induced and moved inside graphene by an external gate voltage. The spatial resolution of this electrical technique is determined by the p-n junction width inside graphene, which could achieve  $\sim 20$  nm-scale in our device, demonstrated by mapping the electric field distribution of a strongly confined GSP mode profile. The precision of this characterization method can further be improved by decreasing the thickness of the gating dielectric or decreasing the temperature.

Except for the modulation medium, the dielectric layer is also essential in electro-optics for normal gating. Therefore, the question arises: what is the best dielectric for electro-optics? In Chapter 5, we obtained some thoughts about this question. We investigated the dielectric performance of two widely-used dielectric materials, hafnia and alumina ( $\text{HfO}_2$  and  $\text{Al}_2\text{O}_3$ ), with a simple graphene field-effect structure. We surprisingly found that this question is imprecise as the fabrication methods of gating dielectrics in graphene-based devices could profoundly affect the gating hysteresis. Specifically, oxide dielectrics fabricated by atomic layer deposition display a pronounced positive hysteresis of graphene gating characteristics, but the same dielectrics made by e-beam evaporation showed mostly negative hysteresis. Through an XPS analysis, we concluded that this behavior results from the samples' stoichiometry and ion migration.

In summary, we have studied two approaches for electro-optical modulation with the integration of 2D material and nanostructures. Our devices show reliable modulation, which can be used in realistic applications. On the other hand, our studies provide new paradigms for nanoscale optical characterization, such as ellipsometric analysis of the optical constant of the material and non-invasive light mapping in 2D material, as described in Chapters 3 and 4. Besides, it is suggested that oxide dielectrics shall be avoided in graphene gated devices that work at room temperatures (Chapter 5). Our research provides new paradigms for the design and fabrication in 2D material-based nanoscale electro-optics and offers promising opportunities for nanoscale (plasmonic) on-chip devices.

Our graphene plasmonic waveguide device can also work as a photodetector, producing an electric signal from the waveguide mode. Two pieces of graphene have been fabricated in the plasmonic waveguide devices, and an integrated on-chip plasmonic modulator and detector could be realized in the next stage. Besides, for complete optical

communication, an optical emitter, modulator, and detector are needed. 2D material-based optical emitters could be studied in the future for an integrated on-chip optical communication system.

# Publications

Kravets, V. G.; Wu, F.; Auton, G. H.; Yu, T.; Shinji, I.; Grigorenko, A. N., Measurements of electrically tunable refractive index of MoS<sub>2</sub> monolayer and its usage in optical modulators. NPJ 2D Materials Applications 2019, 3 (1), 36.

Yu, T.; Kravets, V. G.; Imaizumi, S.; Grigorenko, A. N., Effect of dielectric fabrication techniques on graphene gating. The Journal of Physical Chemistry C 2020, 125 (1), 865-872.

Nanoscale light field imaging with graphene, submitted to Nature Photonics, under second review.

Noble metal-dielectric-graphene hybrid nanostructures with enhanced surface plasmon resonance sensitivity based on amplitude and phase measurements, under submission

# Conferences

Graphene-NOWNANO CDT conference 2018, June 2018, Cheshire, UK, Poster presentation: Optical modulators based on hybrid plasmonic nanostructures

Graphene2019 International Conference, June 2019, Rome, Italy, Poster presentation: Tunability of optical absorption of MoS<sub>2</sub> by electrical gating and its application in a hybrid electro-optical modulator

Graphene-NOWNANO CDT conference 2019, July 2019, Cambridgeshire, UK, Poster presentation: Tunability of optical absorption of MoS<sub>2</sub> by electrical gating and its application in a hybrid electro-optical modulator

# References

1. K. S. Novoselov, A. K. G., S. V. Morozov, D. Jiang, Y. Zhang, S. V. Dubonos, I. V. Grigorieva, A. A. Firsov, Electric field effect in atomically thin carbon films. *Science* **2004**, 306 (5696), 666-669.
2. Sun, Z.; Martinez, A.; Wang, F., Optical modulators with 2D layered materials. *Nature Photonics* **2016**, 10 (4), 227-238.
3. Long, M.; Wang, P.; Fang, H.; Hu, W., Progress, challenges, and opportunities for 2D material based photodetectors. *Advanced Functional Materials* **2019**, 29 (19), 1803807.
4. Schwierz, F., Graphene transistors. *Nat Nanotechnol* **2010**, 5 (7), 487-96.
5. Mak, K. F.; Shan, J., Photonics and optoelectronics of 2D semiconductor transition metal dichalcogenides. *Nature Photonics* **2016**, 10 (4), 216-226.
6. Shavanova, K.; Bakakina, Y.; Burkova, I.; Shtepliuk, I.; Viter, R.; Ubelis, A.; Beni, V.; Starodub, N.; Yakimova, R.; Khranovskyy, V., Application of 2D non-graphene materials and 2D oxide nanostructures for biosensing technology. *Sensors* **2016**, 16 (2), 223.
7. Zhang, X.; Hou, L.; Ciesielski, A.; Samorì, P., 2D materials beyond graphene for high performance energy storage applications. *Advanced Energy Materials* **2016**, 6 (23), 1600671.
8. Wu, Y.; Yu, Y., 2D material as anode for sodium ion batteries: recent progress and perspectives. *J Energy Storage Materials* **2019**, 16, 323-343.
9. Mennel, L.; Symonowicz, J.; Wachter, S.; Polyushkin, D. K.; Molina-Mendoza, A. J.; Mueller, T., Ultrafast machine vision with 2D material neural network image sensors. *Nature* **2020**, 579 (7797), 62-66.
10. Jason S. Ross, S. W., Hongyi Yu, Nirmal J. Ghimire, Aaron M. Jones, Grant Aivazian, Jiaqiang Yan, David G. Mandrus, Di Xiao, Wang Yao, Xiaodong Xu, Electrical control of neutral and charged excitons in a monolayer semiconductor. *Nature Communications* **2013**, 4 (1), 1474.
11. Mouri, S.; Miyauchi, Y.; Matsuda, K., Tunable photoluminescence of monolayer MoS<sub>2</sub> via chemical doping. *Nano Lett* **2013**, 13 (12), 5944-8.

12. Li, W.; Chen, B.; Meng, C.; Fang, W.; Xiao, Y.; Li, X.; Hu, Z.; Xu, Y.; Tong, L.; Wang, H.; Liu, W.; Bao, J.; Shen, Y. R., Ultrafast all-optical graphene modulator. *Nano Letters* **2014**, *14* (2), 955-959.
13. Jianfeng, D.; Ruiqiang, J.; Lei, Z.; Lin, Y., Electro-optical response analysis of a 40 Gb/s silicon Mach-Zehnder optical modulator. *Journal of Lightwave Technology* **2013**, *31* (14), 2434-2440.
14. Ahmed, A. N. R.; Nelan, S.; Shi, S.; Yao, P.; Mercante, A.; Prather, D. W., Subvolt electro-optical modulator on thin-film lithium niobate and silicon nitride hybrid platform. *Opt Lett* **2020**, *45* (5), 1112-1115.
15. Janner, D.; Tulli, D.; García-Granda, M.; Belmonte, M.; Pruneri, V., Micro-structured integrated electro-optic LiNbO<sub>3</sub> modulators. *Laser & Photonics Review* **2009**, *3* (3), 301-313.
16. Liu, M.; Yin, X.; Ulin-Avila, E.; Geng, B.; Zentgraf, T.; Ju, L.; Wang, F.; Zhang, X., A graphene-based broadband optical modulator. *Nature* **2011**, *474* (7349), 64-7.
17. Ganz, E.; Ganz, A. B.; Yang, L.-M.; Dornfeld, M., The initial stages of melting of graphene between 4000 K and 6000 K. *Physical Chemistry Chemical Physics* **2017**, *19* (5), 3756-3762.
18. Thurmond, C., The standard thermodynamic functions for the formation of electrons and holes in Ge, Si, GaAs, and GaP. *Journal of the Electrochemical Society* **1975**, *122* (8), 1133.
19. Yu, S.; Wu, X.; Wang, Y.; Guo, X.; Tong, L., 2D materials for optical modulation: challenges and opportunities. *Adv Mater* **2017**, *29* (14).
20. Xia, F.; Mueller, T.; Lin, Y. M.; Valdes-Garcia, A.; Avouris, P., Ultrafast graphene photodetector. *Nat Nanotechnol* **2009**, *4* (12), 839-43.
21. Ferrari, A. C.; Bonaccorso, F.; Fal'Ko, V.; Novoselov, K. S.; Roche, S.; Bøggild, P.; Borini, S.; Koppens, F. H.; Palermo, V.; Pugno, N., Science and technology roadmap for graphene, related two-dimensional crystals, and hybrid systems. *Nanoscale* **2015**, *7* (11), 4598-4810.
22. Mak, K. F.; He, K.; Lee, C.; Lee, G. H.; Hone, J.; Heinz, T. F.; Shan, J., Tightly bound trions in monolayer MoS<sub>2</sub>. *Nat Mater* **2013**, *12* (3), 207-11.
23. Kang, P.; Wang, M. C.; Knapp, P. M.; Nam, S., Crumpled graphene photodetector with enhanced, strain-tunable, and wavelength-selective photoresponsivity. *Adv Mater* **2016**, *28* (23), 4639-4645.



24. Zhao, B.; Zhao, J. M.; Zhang, Z. M., Enhancement of near-infrared absorption in graphene with metal gratings. *Applied Physics Letters* **2014**, *105* (3).
25. Li, B.; Zu, S.; Zhou, J.; Jiang, Q.; Du, B.; Shan, H.; Luo, Y.; Liu, Z.; Zhu, X.; Fang, Z., Single-nanoparticle plasmonic electro-optic modulator based on MoS<sub>2</sub> monolayers. *ACS Nano* **2017**, *11* (10), 9720-9727.
26. He, M.; Quan, C.; He, C.; Huang, Y.; Zhu, L.; Yao, Z.; Zhang, S.; Bai, J.; Xu, X., Enhanced nonlinear saturable absorption of MoS<sub>2</sub>/graphene nanocomposite films. *The Journal of Physical Chemistry C* **2017**, *121* (48), 27147-27153.
27. Hernández, G., *Fabry-perot interferometers*. Cambridge University Press: 1988.
28. Zia, R.; Schuller, J. A.; Chandran, A.; Brongersma, M. L., Plasmonics: the next chip-scale technology. *Materials today* **2006**, *9* (7-8), 20-27.
29. Cao, Y.; Fatemi, V.; Fang, S.; Watanabe, K.; Taniguchi, T.; Kaxiras, E.; Jarillo-Herrero, P., Unconventional superconductivity in magic-angle graphene superlattices. *Nature* **2018**, *556* (7699), 43-50.
30. Mas-Balleste, R.; Gomez-Navarro, C.; Gomez-Herrero, J.; Zamora, F., 2D materials: to graphene and beyond. *Nanoscale* **2011**, *3* (1), 20-30.
31. Wang, F.; Zhang, Y.; Tian, C.; Girit, C.; Zettl, A.; Crommie, M.; Shen, Y. R., Gate-variable optical transitions in graphene. *Science* **2008**, *320* (5873), 206-9.
32. Castro Neto, A. H.; Guinea, F.; Peres, N. M. R.; Novoselov, K. S.; Geim, A. K., The electronic properties of graphene. *Reviews of Modern Physics* **2009**, *81* (1), 109-162.
33. Geim, A. K.; Novoselov, K. S., The rise of graphene. *Nature Materials* **2007**, *6* (3), 183-191.
34. Ansell, D.; Radko, I. P.; Han, Z.; Rodriguez, F. J.; Bozhevolnyi, S. I.; Grigorenko, A. N., Hybrid graphene plasmonic waveguide modulators. *Nature Communications* **2015**, *6* (1), 8846.
35. Sun, F.; Xia, L.; Nie, C.; Qiu, C.; Tang, L.; Shen, J.; Sun, T.; Yu, L.; Wu, P.; Yin, S.; Yan, S.; Du, C., An all-optical modulator based on a graphene-plasmonic slot waveguide at 1550 nm. *Applied Physics Express* **2019**, *12* (4).
36. Ferrari, A. C.; Meyer, J. C.; Scardaci, V.; Casiraghi, C.; Lazzeri, M.; Mauri, F.; Piscanec, S.; Jiang, D.; Novoselov, K. S.; Roth, S.; Geim, A. K., Raman spectrum of graphene and graphene layers. *Phys Rev Lett* **2006**, *97* (18), 187401.

37. Kim, S.; Nah, J.; Jo, I.; Shahrjerdi, D.; Colombo, L.; Yao, Z.; Tutuc, E.; Banerjee, S. K., Realization of a high mobility dual-gated graphene field-effect transistor with Al<sub>2</sub>O<sub>3</sub> dielectric. *Applied Physics Letters* **2009**, *94* (6).
38. Nair, R. R.; Blake, P.; Grigorenko, A. N.; Novoselov, K. S.; Booth, T. J.; Stauber, T.; Peres, N. M. R.; Geim, A. K., Fine structure constant defines visual transparency of graphene. *Science* **2008**, *320* (5881), 1308-1308.
39. Das, A.; Pisana, S.; Chakraborty, B.; Piscanec, S.; Saha, S. K.; Waghmare, U. V.; Novoselov, K. S.; Krishnamurthy, H. R.; Geim, A. K.; Ferrari, A. C.; Sood, A. K., Monitoring dopants by Raman scattering in an electrochemically top-gated graphene transistor. *Nat Nanotechnol* **2008**, *3* (4), 210-5.
40. Chen, C. F.; Park, C. H.; Boudouris, B. W.; Horng, J.; Geng, B.; Girit, C.; Zettl, A.; Crommie, M. F.; Segalman, R. A.; Louie, S. G.; Wang, F., Controlling inelastic light scattering quantum pathways in graphene. *Nature* **2011**, *471* (7340), 617-20.
41. Christy, R. I., Sputtered MoS<sub>2</sub> lubricant coating improvements. *Thin Solid Films* **1980**, *73*, 299-307.
42. Li, G.; Zhang, D.; Qiao, Q.; Yu, Y.; Peterson, D.; Zafar, A.; Kumar, R.; Curtarolo, S.; Hunte, F.; Shannon, S.; Zhu, Y.; Yang, W.; Cao, L., All the catalytic active sites of MoS<sub>2</sub> for hydrogen evolution. *J Am Chem Soc* **2016**, *138* (51), 16632-16638.
43. Hwang, H.; Kim, H.; Cho, J., MoS<sub>2</sub> nanoplates consisting of disordered graphene-like layers for high rate lithium battery anode materials. *Nano Lett* **2011**, *11* (11), 4826-4830.
44. Radisavljevic, B.; Whitwick, M. B.; Kis, A., Integrated circuits and logic operations based on single-layer MoS<sub>2</sub>. *ACS Nano* **2011**, *5* (12), 9934-9938.
45. Radisavljevic, B.; Radenovic, A.; Brivio, J.; Giacometti, V.; Kis, A., Single-layer MoS<sub>2</sub> transistors. *Nature Nanotech.* **2011**, *6* (3), 147-150.
46. Lopez-Sanchez, O.; Lembke, D.; Kayci, M.; Radenovic, A.; Kis, A., Ultrasensitive photodetectors based on monolayer MoS<sub>2</sub>. *Nature Nanotech.* **2013**, *8* (7), 497-501.
47. Yin, Z.; Li, H.; Li, H.; Jiang, L.; Shi, Y.; Sun, Y.; Lu, G.; Zhang, Q.; Chen, X.; Zhang, H., Single-layer MoS<sub>2</sub> phototransistors. *ACS nano* **2012**, *6* (1), 74-80.
48. Mak, K. F.; Lee, C.; Hone, J.; Shan, J.; Heinz, T. F., Atomically thin MoS<sub>2</sub>: a new direct-gap semiconductor. *Phys Rev Lett* **2010**, *105* (13), 136805.

49. Splendiani, A.; Sun, L.; Zhang, Y.; Li, T.; Kim, J.; Chim, C.-Y.; Galli, G.; Wang, F., Emerging photoluminescence in monolayer MoS<sub>2</sub>. *Nano Letters* **2010**, *10* (4), 1271-1275.
50. Najmaei, S.; Liu, Z.; Zhou, W.; Zou, X.; Shi, G.; Lei, S.; Yakobson, B. I.; Idrobo, J. C.; Ajayan, P. M.; Lou, J., Vapour phase growth and grain boundary structure of molybdenum disulphide atomic layers. *Nat Mater* **2013**, *12* (8), 754-9.
51. Pacifici, D.; Lezec, H. J.; Atwater, H. A., All-optical modulation by plasmonic excitation of CdSe quantum dots. *Nature Photonics* **2007**, *1* (7), 402-406.
52. Xu, Q.; Schmidt, B.; Pradhan, S.; Lipson, M., Micrometre-scale silicon electro-optic modulator. *Nature* **2005**, *435* (7040), 325-7.
53. Cocorullo, G.; Rendina, I., Thermo-optical modulation at 1.5  $\mu$ m in silicon etalon. *Electronics Letters* **1992**, *28* (1), 83-85.
54. Courjal, N.; Benchabane, S.; Dahdah, J.; Ulliac, G.; Gruson, Y.; Laude, V., Acousto-optically tunable lithium niobate photonic crystal. *Applied Physics Letters* **2010**, *96* (13).
55. Gawlik, W.; Krzemień, L.; Pustelny, S.; Sangla, D.; Zachorowski, J.; Graf, M.; Sushkov, A. O.; Budker, D., Nonlinear magneto-optical rotation with amplitude modulated light. *Applied Physics Letters* **2006**, *88* (13).
56. Minnai, C.; Di Vece, M.; Milani, P., Mechanical-optical-electro modulation by stretching a polymer-metal nanocomposite. *Nanotechnology* **2017**, *28* (35), 355702.
57. Assefa, S.; Shank, S.; Green, W.; Khater, M.; Kiewra, E.; Reinholm, C.; Kamlapurkar, S.; Rylyakov, A.; Schow, C.; Horst, F.; Pan, H.; Topuria, T.; Rice, P.; Gill, D. M.; Rosenberg, J.; Barwicz, T.; Yang, M.; Proesel, J.; Hofrichter, J.; Offrein, B.; Gu, X.; Haensch, W.; Ellis-Monaghan, J.; Vlasov, Y. In *A 90 nm CMOS integrated nano-photonics technology for 25 Gbps WDM optical communications applications*, 2012 International Electron Devices Meeting, 10-13 Dec. 2012; 2012; pp 33.8.1-33.8.3.
58. Kerr, J., A new relation between electricity and light: dielectrified media birefringent. *The London, Edinburgh, and Dublin Philosophical Magazine and Journal of Science* **1875**, *50* (332), 337-348.
59. Pockels, F. C. A., *Lehrbuch der kristallographie*. BG Teubner: 1906; Vol. 19.
60. Miller, D. A. B.; Chemla, D. S.; Damen, T. C.; Gossard, A. C.; Wiegmann, W.; Wood, T. H.; Burrus, C. A., Band-edge electroabsorption in quantum well

structures: the quantum-confined stark effect. *Physical Review Letters* **1984**, 53 (22), 2173-2176.

61. Reed, G. T.; Mashanovich, G.; Gardes, F. Y.; Thomson, D. J., Silicon optical modulators. *Nature Photonics* **2010**, 4 (8), 518-526.

62. Kravets, V. G.; Wu, F.; Auton, G. H.; Yu, T.; Shinji, I.; Grigorenko, A. N., Measurements of electrically tunable refractive index of MoS<sub>2</sub> monolayer and its usage in optical modulators. *NPJ 2D Materials Applications* **2019**, 3 (1), 36.

63. Guo, Q.; Yao, Y.; Luo, Z.-C.; Qin, Z.; Xie, G.; Liu, M.; Kang, J.; Zhang, S.; Bi, G.; Liu, X.; Qiu, J., Universal near-infrared and mid-infrared optical modulation for ultrafast pulse generation enabled by colloidal plasmonic semiconductor nanocrystals. *ACS Nano* **2016**, 10 (10), 9463-9469.

64. Rahm, M.; Li, J.-S.; Padilla, W. J., THz wave modulators: a brief review on different modulation techniques. *Journal of Infrared, Millimeter, and Terahertz Waves* **2012**, 34 (1), 1-27.

65. Arumugam, M., Optical fiber communication-an overview. *Pramana* **2001**, 57 (5), 849-869.

66. Haffner, C.; Chelladurai, D.; Fedoryshyn, Y.; Josten, A.; Baeuerle, B.; Heni, W.; Watanabe, T.; Cui, T.; Cheng, B.; Saha, S.; Elder, D. L.; Dalton, L. R.; Boltasseva, A.; Shalae, V. M.; Kinsey, N.; Leuthold, J., Low-loss plasmon-assisted electro-optic modulator. *Nature* **2018**, 556 (7702), 483-486.

67. Bonaccorso, F.; Sun, Z.; Hasan, T.; Ferrari, A. C., Graphene photonics and optoelectronics. *Nature Photonics* **2010**, 4 (9), 611-622.

68. Geim, A. K.; Grigorieva, I. V., Van der Waals heterostructures. *Nature* **2013**, 499 (7459), 419-425.

69. Xia, F.; Wang, H.; Xiao, D.; Dubey, M.; Ramasubramaniam, A., Two-dimensional material nanophotonics. *Nature Photonics* **2014**, 8 (12), 899-907.

70. Mohsin, M.; Neumaier, D.; Schall, D.; Otto, M.; Matheisen, C.; Giesecke, A. L.; Sagade, A. A.; Kurz, H., Experimental verification of electro-refractive phase modulation in graphene. *Sci Rep* **2015**, 5, 10967.

71. Hao, R.; Du, W.; Chen, H.; Jin, X.; Yang, L.; Li, E., Ultra-compact optical modulator by graphene induced electro-refraction effect. *Applied Physics Letters* **2013**, 103 (6).

72. Mohsin, M.; Schall, D.; Otto, M.; Noculak, A.; Neumaier, D.; Kurz, H., Graphene based low insertion loss electro-absorption modulator on SOI waveguide. *Opt Express* **2014**, 22 (12), 15292-7.
73. Ye, S.; Wang, Z.; Tang, L.; Zhang, Y.; Lu, R.; Liu, Y., Electro-absorption optical modulator using dual-graphene-on-graphene configuration. *Opt Express* **2014**, 22 (21), 26173-80.
74. Phare, C. T.; Daniel Lee, Y.-H.; Cardenas, J.; Lipson, M., Graphene electro-optic modulator with 30 GHz bandwidth. *Nature Photonics* **2015**, 9 (8), 511-514.
75. Hu, Y.; Pantouvaki, M.; Van Campenhout, J.; Brems, S.; Asselberghs, I.; Huyghebaert, C.; Absil, P.; Van Thourhout, D., Broadband 10 Gb/s operation of graphene electro-absorption modulator on silicon. *Laser & Photonics Reviews* **2016**, 10 (2), 307-316.
76. Liu, M.; Yin, X.; Zhang, X., Double-layer graphene optical modulator. *Nano Lett* **2012**, 12 (3), 1482-5.
77. Yan, J.; Ma, C.; Huang, Y.; Yang, G., Single silicon nanostripe gated suspended monolayer and bilayer WS<sub>2</sub> to realize abnormal electro-optical modulation. *Materials Horizons* **2019**, 6 (2), 334-342.
78. Ansari, N.; Amin, R.; Maiti, R.; Sorger, V. J. In *MoTe<sub>2</sub> based electro-optic modulator on Mach-Zehnder Interferometer*, Frontiers in Optics + Laser Science APS/DLS, Washington, DC, 2019/09/15; Optical Society of America: Washington, DC, 2019; p JW4A.65.
79. Cui, Y.; Xin, R.; Yu, Z.; Pan, Y.; Ong, Z. Y.; Wei, X.; Wang, J.; Nan, H.; Ni, Z.; Wu, Y.; Chen, T.; Shi, Y.; Wang, B.; Zhang, G.; Zhang, Y. W.; Wang, X., High-performance monolayer WS<sub>2</sub> field-effect transistors on high-κ dielectrics. *Adv Mater* **2015**, 27 (35), 5230-4.
80. Pradhan, N. R.; Rhodes, D.; Zhang, Q.; Talapatra, S.; Terrones, M.; Ajayan, P. M.; Balicas, L., Intrinsic carrier mobility of multi-layered MoS<sub>2</sub> field-effect transistors on SiO<sub>2</sub>. *Applied Physics Letters* **2013**, 102 (12).
81. Zhang, W.; Huang, Z.; Zhang, W.; Li, Y., Two-dimensional semiconductors with possible high room temperature mobility. *Nano Research* **2014**, 7 (12), 1731-1737.
82. Kaasbjerg, K.; Thygesen, K. S.; Jacobsen, K. W., Phonon-limited mobility in n-type single-layer MoS<sub>2</sub> from first principles. *Physical Review B* **2012**, 85 (11).

83. Eda, G.; Maier, S. A., Two-dimensional crystals: managing light for optoelectronics. *ACS nano* **2013**, 7 (7), 5660-5665.
84. Rodriguez, F. J.; Aznakayeva, D. E.; Marshall, O. P.; Kravets, V. G.; Grigorenko, A. N., Solid-state electrolyte-gated graphene in optical modulators. *Advanced Materials* **2017**, 29 (19), 1606372.
85. Peng, R.; Khaliji, K.; Youngblood, N.; Grassi, R.; Low, T.; Li, M., Midinfrared electro-optic modulation in few-layer black phosphorus. *Nano Lett* **2017**, 17 (10), 6315-6320.
86. Lin, C.; Grassi, R.; Low, T.; Helmy, A. S., Multilayer black phosphorus as a versatile mid-infrared electro-optic material. *Nano Lett* **2016**, 16 (3), 1683-9.
87. Xia, F.; Wang, H.; Jia, Y., Rediscovering black phosphorus as an anisotropic layered material for optoelectronics and electronics. *Nat Commun* **2014**, 5, 4458.
88. Freestone, I.; Meeks, N.; Sax, M.; Higgitt, C., The Lycurgus cup — a roman nanotechnology. *Gold bulletin* **2007**, 40 (4), 270-277.
89. Mie, G., Beiträge zur Optik trüber Medien, speziell kolloidaler Metallösungen. *Annalen der physik* **1908**, 330 (3), 377-445.
90. Wood, R. W., XLII. On a remarkable case of uneven distribution of light in a diffraction grating spectrum. *The London, Edinburgh, Dublin Philosophical Magazine, Journal of Science* **1902**, 4 (21), 396-402.
91. Rayleigh, L., On the dynamical theory of gratings. *Proceedings of the Royal Society of London. Series A, Containing Papers of a Mathematical, Physical Character* **1907**, 79 (532), 399-416.
92. Fano, U., The theory of anomalous diffraction gratings and of quasi-stationary waves on metallic surfaces (Sommerfeld's waves). *JOSA* **1941**, 31 (3), 213-222.
93. Zenneck, J., Über die Fortpflanzung ebener elektromagnetischer Wellen längs einer ebenen Leiterfläche und ihre Beziehung zur drahtlosen Telegraphie. *Annalen der Physik* **1907**, 328 (10), 846-866.
94. Sommerfeld, A., *Über die Ausbreitung der Wellen in der drahtlosen Telegraphie*. Verlag der Königlich Bayerischen Akademie der Wissenschaften: 1909.
95. Pines, D., Collective energy losses in solids. *Reviews of modern physics* **1956**, 28 (3), 184.
96. Powell, C.; Swan, J., Effect of oxidation on the characteristic loss spectra of aluminum and magnesium. *Physical Review* **1960**, 118 (3), 640.

97. Stern, E.; Ferrell, R., Surface plasma oscillations of a degenerate electron gas. *Physical Review* **1960**, *120* (1), 130.
98. Ritchie, R. H.; Arakawa, E.; Cowan, J.; Hamm, R., Surface-plasmon resonance effect in grating diffraction. *Physical Review Letters* **1968**, *21* (22), 1530.
99. Otto, A., Excitation of nonradiative surface plasma waves in silver by the method of frustrated total reflection. *Zeitschrift für Physik A Hadrons and nuclei* **1968**, *216* (4), 398-410.
100. Kretschmann, E.; Raether, H., Radiative decay of non-radiative surface plasmons excited by light. *Z. Naturforsch. a* **1968**, *23* (12), 2135-2136.
101. Kreibig, U.; Zacharias, P., Surface plasma resonances in small spherical silver and gold particles. *Zeitschrift für Physik A Hadrons and nuclei* **1970**, *231* (2), 128-143.
102. Cunningham, S. L.; Maradudin, A. A.; Wallis, R. F., Effect of a charge layer on the surface-plasmon-polariton dispersion curve. *Physical Review B* **1974**, *10* (8), 3342-3355.
103. Boardman, A. D., *Electromagnetic surface modes*. John Wiley & Sons: 1982.
104. Schatz, G. C.; Young, M. A.; Van Duyne, R. P., Electromagnetic mechanism of SERS. *Surface-enhanced Raman scattering* **2006**, 19-45.
105. Ebbesen, T. W.; Lezec, H. J.; Ghaemi, H.; Thio, T.; Wolff, P. A., Extraordinary optical transmission through sub-wavelength hole arrays. *Nature* **1998**, *391* (6668), 667-669.
106. Gramotnev, D. K.; Bozhevolnyi, S. I., Plasmonics beyond the diffraction limit. *Nature Photonics* **2010**, *4* (2), 83-91.
107. Maier, S. A., *Plasmonics: fundamentals and applications*. Springer Science & Business Media: 2007.
108. Brolo, A. G., Plasmonics for future biosensors. *Nature Photonics* **2012**, *6* (11), 709-713.
109. Atwater, H. A.; Polman, A., Plasmonics for improved photovoltaic devices. *Materials for sustainable energy: A collection of peer-reviewed research review articles from nature publishing group* **2011**, 1-11.
110. Grigorenko, A.; Polini, M.; Novoselov, K., Graphene plasmonics. *Nature Photonics* **2012**, *6* (11), 749-758.
111. Zayats, A. V.; Smolyaninov, I. I.; Maradudin, A. A., Nano-optics of surface plasmon polaritons. *Physics Reports* **2005**, *408* (3-4), 131-314.

112. Barnes, W. L.; Dereux, A.; Ebbesen, T. W., Surface plasmon subwavelength optics. *Nature* **2003**, *424* (6950), 824-830.
113. Devaux, E.; Ebbesen, T. W.; Weeber, J.-C.; Dereux, A., Launching and decoupling surface plasmons via micro-gratings. *Applied Physics Letters* **2003**, *83* (24), 4936-4938.
114. Kriesch, A.; Burgos, S. P.; Ploss, D.; Pfeifer, H.; Atwater, H. A.; Peschel, U., Functional plasmonic nanocircuits with low insertion and propagation losses. *Nano Letters* **2013**, *13* (9), 4539-4545.
115. Pan, D.; Wei, H.; Jia, Z.; Xu, H., Mode conversion of propagating surface plasmons in nanophotonic networks induced by structural symmetry breaking. *Scientific Reports* **2014**, *4* (1).
116. Bharadwaj, P.; Bouhelier, A.; Novotny, L., Electrical excitation of surface plasmons. *Physical Review Letters* **2011**, *106* (22).
117. Maier, S. A.; Kik, P. G.; Atwater, H. A.; Meltzer, S.; Harel, E.; Koel, B. E.; Requicha, A. A., Local detection of electromagnetic energy transport below the diffraction limit in metal nanoparticle plasmon waveguides. *Nat Mater* **2003**, *2* (4), 229-32.
118. Thackray, B. D.; Thomas, P. A.; Auton, G. H.; Rodriguez, F. J.; Marshall, O. P.; Kravets, V. G.; Grigorenko, A. N., Super-narrow, extremely high quality collective plasmon resonances at telecom wavelengths and their application in a hybrid graphene-plasmonic modulator. *Nano Letters* **2015**, *15* (5), 3519-3523.
119. Bozhevolnyi, S. I.; Volkov, V. S.; Devaux, E.; Ebbesen, T. W., Channel plasmon-polariton guiding by subwavelength metal grooves. *Phys Rev Lett* **2005**, *95* (4), 046802.
120. Yang, R.; Wahsheh, R. A.; Lu, Z.; Abushagur, M. A., Efficient light coupling between dielectric slot waveguide and plasmonic slot waveguide. *Opt. Lett.* **2010**, *35* (5), 649-651.
121. Jin Tae Kim, J. J. J., Suntak Park, Min-su Kim, Seung Koo Park, Myung-Hyun Lee, Chip-to-chip optical interconnect using gold long-range surface plasmon polariton waveguides. *Opt. Express* **2008**, *16* (17), 13133-13138.
122. Pimpin, A.; Srituravanich, W., Review on micro- and nanolithography techniques and their applications. *Engineering Journal* **2012**, *16* (1), 37-56.
123. Nagashio, K.; Yamashita, T.; Fujita, J.; Nishimura, T.; Kita, K.; Toriumi, A. In *Impacts of graphene/SiO<sub>2</sub> interaction on FET mobility and Raman spectra in*



*mechanically exfoliated graphene films*, 2010 International Electron Devices Meeting, IEEE: 2010; pp 23.4. 1-23.4. 4.

124. Asay, D. B.; Kim, S. H., Evolution of the adsorbed water layer structure on silicon oxide at room temperature. *The Journal of Physical Chemistry B* **2005**, *109* (35), 16760-16763.

125. Moon, J.-Y.; Kim, M.; Kim, S.-I.; Xu, S.; Choi, J.-H.; Whang, D.; Watanabe, K.; Taniguchi, T.; Park, D. S.; Seo, J.; Cho, S. H.; Son, S.-K.; Lee, J.-H., Layer-engineered large-area exfoliation of graphene. *Science Advances* **2020**, *6* (44), eabc6601.

126. Huang, Y.; Sutter, E.; Shi, N. N.; Zheng, J.; Yang, T.; Englund, D.; Gao, H.-J.; Sutter, P., Reliable exfoliation of large-area high-quality flakes of graphene and other two-dimensional materials. *ACS Nano* **2015**, *9* (11), 10612-10620.

127. Blake, P.; Hill, E. W.; Castro Neto, A. H.; Novoselov, K. S.; Jiang, D.; Yang, R.; Booth, T. J.; Geim, A. K., Making graphene visible. *Applied Physics Letters* **2007**, *91* (6).

128. Feng, J.; Li, W.; Qian, X.; Qi, J.; Qi, L.; Li, J., Patterning of graphene. *Nanoscale* **2012**, *4* (16), 4883-99.

129. J. SINGH, D. E. W., Nano and macro-structured component fabrication by electron beam physical vapor deposition. *Journal of Materials Science* **2005**, *40*, 1-26.

130. George, S. M., Atomic layer deposition: an overview. *Chemical Reviews* **2010**, *110*, 111-131.

131. KRISHNAN, C. V. R. K. S., A new type of secondary radiation. *Nature* **1928**, *121*, 501-502.

132. Binnig, G.; Quate, C. F.; Gerber, C., Atomic force microscope. *Phys Rev Lett* **1986**, *56* (9), 930-933.

133. Binnig, G.; Rohrer, H.; Gerber, C.; Weibel, E., Surface studies by scanning tunneling microscopy. *Physical Review Letters* **1982**, *49* (1), 57-61.

134. Knoll, M., Aufladepotential und sekundäremission elektronenbestrahlter körper. *Zeitschrift für technische Physik* **1935**, *16*, 467-475.

135. Von Ardenne, M., Improvements in electron microscopes. *convention date Germany* **1937**, (GB 511204).

136. Briggs, D., Handbook of X-ray photoelectron spectroscopy. *Surface and Interface Analysis* **1981**, *3* (4), v-v.

137. Moulder, J.; Stickle, W.; Sobol, W.; Bomben, K. D. In *Handbook of x-Ray photoelectron spectroscopy*, 1992.
138. Irene, E. A., Applications of spectroscopic ellipsometry to microelectronics. *Thin Solid Films* **1993**, 233, 96-111.
139. Aspnes, D. E., Spectroscopic ellipsometry — past, present, and future. *Thin Solid Films* **2014**, 571, 334-344.
140. Drude, P., Bestimmung der optischen constanten der metalle. *Ann. Physik Chemie* **1890**, 38, 481-554.
141. Rothen, A., The ellipsometer, an apparatus to measure thicknesses of thin surface films. *Review of Scientific Instruments* **1945**, 16 (2), 26-30.
142. Michelson, A. A.; Morley, E. W., On the relative motion of the earth and of the luminiferous ether. *Sidereal Messenger* **1887**, 6, 306-310.
143. Fellgett, P. B., The multiplex advantage. *Cambridge, UK* **1951**.
144. Kane, Y., Numerical solution of initial boundary value problems involving maxwell's equations in isotropic media. *IEEE Transactions on Antennas and Propagation* **1966**, 14 (3), 302-307.
145. Srivastava, Y. K.; Chaturvedi, A.; Manjappa, M.; Kumar, A.; Dayal, G.; Kloc, C.; Singh, R., MoS<sub>2</sub> for ultrafast all-optical switching and modulation of THz fano metaphotonic devices. *Advanced Optical Materials* **2017**, 5 (23).
146. Sobhani, A.; Lauchner, A.; Najmaei, S.; Ayala-Orozco, C.; Wen, F.; Lou, J.; Halas, N. J., Enhancing the photocurrent and photoluminescence of single crystal monolayer MoS<sub>2</sub> with resonant plasmonic nanoshells. *Applied Physics Letters* **2014**, 104 (3).
147. Janisch, C.; Song, H.; Zhou, C.; Lin, Z.; Elías, A. L.; Ji, D.; Terrones, M.; Gan, Q.; Liu, Z., MoS<sub>2</sub> monolayers on nanocavities: enhancement in light–matter interaction. *2D Materials* **2016**, 3 (2).
148. Schuller, J. A.; Karaveli, S.; Schiros, T.; He, K.; Yang, S.; Kymissis, I.; Shan, J.; Zia, R., Orientation of luminescent excitons in layered nanomaterials. *Nature Nanotech.* **2013**, 8 (4), 271-276.
149. Wooten, F., *Optical properties of solids*. Academic press: 1972.
150. Steinhoff, A.; Rosner, M.; Jahnke, F.; Wehling, T. O.; Gies, C., Influence of excited carriers on the optical and electronic properties of MoS<sub>2</sub>. *Nano letters* **2014**, 14 (7), 3743-3748.

151. Schmitt-Rink, S.; Chemla, D.; Miller, D., Theory of transient excitonic optical nonlinearities in semiconductor quantum-well structures. *Physical Review B* **1985**, *32* (10), 6601.
152. Cheiwchanchamnangij, T.; Lambrecht, W. R., Quasiparticle band structure calculation of monolayer, bilayer, and bulk MoS<sub>2</sub>. *Physical Review B* **2012**, *85* (20), 205302.
153. Lefebvre, P.; Christol, P.; Mathieu, H.; Glutsch, S., Confined excitons in semiconductors: correlation between binding energy and spectral absorption shape. *J Physical Review B* **1995**, *52* (8), 5756.
154. Mostaani, E.; Szyniszewski, M.; Price, C. H.; Maezono, R.; Danovich, M.; Hunt, R. J.; Drummond, N. D.; Fal'ko, V. I., Diffusion quantum monte carlo study of excitonic complexes in two-dimensional transition-metal dichalcogenides. *Physical Review B* **2017**, *96* (7).
155. Kramers, H. A.; Wannier, G. H., Statistics of the two-dimensional ferromagnet. part I. *Physical Review* **1941**, *60* (3), 252-262.
156. Vella, D.; Ovchinnikov, D.; Martino, N.; Vega-Mayoral, V.; Dumcenco, D.; Kung, Y. C.; Antognazza, M. R.; Kis, A.; Lanzani, G.; Mihailovic, D.; Gadermaier, C., Unconventional electroabsorption in monolayer MoS<sub>2</sub>. *2D Materials* **2017**, *4* (2).
157. van Nieuwstadt, J. A.; Sandtke, M.; Harmsen, R. H.; Segerink, F. B.; Prangma, J. C.; Enoch, S.; Kuipers, L., Strong modification of the nonlinear optical response of metallic subwavelength hole arrays. *Phys Rev Lett* **2006**, *97* (14), 146102.
158. Gramotnev, D. K.; Pile, D. F. P., Single-mode subwavelength waveguide with channel plasmon-polaritons in triangular grooves on a metal surface. *Applied Physics Letters* **2004**, *85* (26), 6323-6325.
159. Vernon, K. C.; Gramotnev, D. K.; Pile, D. F. P., Channel plasmon-polariton modes in V grooves filled with dielectric. *Journal of Applied Physics* **2008**, *103* (3).
160. Wang, J.; Cheng, Z.; Chen, Z.; Wan, X.; Zhu, B.; Tsang, H. K.; Shu, C.; Xu, J., High-responsivity graphene-on-silicon slot waveguide photodetectors. *Nanoscale* **2016**, *8* (27), 13206-11.
161. Kravets, V. G.; Kabashin, A. V.; Barnes, W. L.; Grigorenko, A. N., Plasmonic surface lattice resonances: a review of properties and applications. *Chem Rev* **2018**, *118* (12), 5912-5951.
162. Dawlaty, J. M.; Shivaraman, S.; Strait, J.; George, P.; Chandrashekhara, M.; Rana, F.; Spencer, M. G.; Veksler, D.; Chen, Y., Measurement of the optical

absorption spectra of epitaxial graphene from terahertz to visible. *Applied Physics Letters* **2008**, *93* (13).

163. Morozov, S. V.; Novoselov, K. S.; Katsnelson, M. I.; Schedin, F.; Elias, D. C.; Jaszczak, J. A.; Geim, A. K., Giant intrinsic carrier mobilities in graphene and its bilayer. *Phys Rev Lett* **2008**, *100* (1), 016602.

164. Goossens, S.; Navickaite, G.; Monasterio, C.; Gupta, S.; Piqueras, J. J.; Pérez, R.; Burwell, G.; Nikitskiy, I.; Lasanta, T.; Galán, T.; Puma, E.; Centeno, A.; Pesquera, A.; Zurutuza, A.; Konstantatos, G.; Koppens, F., Broadband image sensor array based on graphene–CMOS integration. *Nature Photonics* **2017**, *11* (6), 366-371.

165. Dalir, H.; Xia, Y.; Wang, Y.; Zhang, X., Athermal broadband graphene optical modulator with 35 Ghz speed. *ACS Photonics* **2016**, *3* (9), 1564-1568.

166. Gan, X.; Shiue, R.-J.; Gao, Y.; Meric, I.; Heinz, T. F.; Shepard, K.; Hone, J.; Assefa, S.; Englund, D., Chip-integrated ultrafast graphene photodetector with high responsivity. *Nature Photonics* **2013**, *7* (11), 883-887.

167. Wu, L.; Chu, H. S.; Koh, W. S.; Li, E. P., Highly sensitive graphene biosensors based on surface plasmon resonance. *Opt. Express* **2010**, *18* (14), 14395-14400.

168. Zeng, S.; Sreekanth, K. V.; Shang, J.; Yu, T.; Chen, C. K.; Yin, F.; Baillargeat, D.; Coquet, P.; Ho, H. P.; Kabashin, A. V.; Yong, K. T., Graphene-gold metasurface architectures for ultrasensitive plasmonic biosensing. *Adv Mater* **2015**, *27* (40), 6163-9.

169. Ding, Y.; Guan, X.; Zhu, X.; Hu, H.; Bozhevolnyi, S. I.; Oxenlowe, L. K.; Jin, K. J.; Mortensen, N. A.; Xiao, S., Efficient electro-optic modulation in low-loss graphene-plasmonic slot waveguides. *Nanoscale* **2017**, *9* (40), 15576-15581.

170. Xu, Q.; Almeida, V. R.; Panepucci, R. R.; Lipson, M., Experimental demonstration of guiding and confining light in nanometer-size low-refractive-index material. *Opt. Lett.* **2004**, *29* (14), 1626-1628.

171. Almeida, V. R.; Xu, Q.; Barrios, C. A.; Lipson, M., Guiding and confining light in void nanostructure. *Opt. Lett.* **2004**, *29* (11), 1209-1211.

172. Andryieuski, A.; Malureanu, R.; Biagi, G.; Holmgaard, T.; Lavrinenko, A., Compact dipole nanoantenna coupler to plasmonic slot waveguide. *Opt. Lett.* **2012**, *37* (6), 1124-1126.

173. Lee, H. W.; Papadakis, G.; Burgos, S. P.; Chander, K.; Kriesch, A.; Pala, R.; Peschel, U.; Atwater, H. A., Nanoscale conducting oxide PlasMOSTor. *Nano Lett* **2014**, *14* (11), 6463-8.

174. Ansell, D.; Radko, I. P.; Han, Z.; Rodriguez, F. J.; Bozhevolnyi, S. I.; Grigorenko, A. N., Hybrid graphene plasmonic waveguide modulators. *Nature Communications* **2015**, *6* (1).
175. Radko, I. P.; Bozhevolnyi, S. I.; Grigorenko, A. N., Maximum modulation of plasmon-guided modes by graphene gating. *Opt. Express* **2016**, *24* (8), 8266-8279.
176. Schuler, S.; Schall, D.; Neumaier, D.; Dobusch, L.; Bethge, O.; Schwarz, B.; Krall, M.; Mueller, T., Controlled generation of a p-n junction in a waveguide integrated graphene photodetector. *Nano Lett* **2016**, *16* (11), 7107-7112.
177. Koppens, F. H. L.; Chang, D. E.; Javier Garcia de Abajo, F., Graphene plasmonics: a platform for strong light-matter interactions. *Nano Letters* **2011**, *11* (8), 3370-3377.
178. Low, T.; Chaves, A.; Caldwell, J. D.; Kumar, A.; Fang, N. X.; Avouris, P.; Heinz, T. F.; Guinea, F.; Martin-Moreno, L.; Koppens, F., Polaritons in layered two-dimensional materials. *Nature Materials* **2017**, *16* (2), 182-194.
179. Fang, N.; Lee, H.; Sun, C.; Zhang, X., Sub-diffraction-limited optical imaging with a silver superlens. *Science* **2005**, *308* (5721), 534.
180. Zhang, X.; Liu, Z., Superlenses to overcome the diffraction limit. *Nature Materials* **2008**, *7* (6), 435-441.
181. Born, M.; Wolf, E., *Principles of Optics*. Cambridge University Press: Cambridge, England, 1980.
182. Echtermeyer, T. J.; Britnell, L.; Jasnós, P. K.; Lombardo, A.; Gorbachev, R. V.; Grigorenko, A. N.; Geim, A. K.; Ferrari, A. C.; Novoselov, K. S., Strong plasmonic enhancement of photovoltage in graphene. *Nature Communications* **2011**, *2*, 458.
183. Gabor, N. M.; Song, J. C. W.; Ma, Q.; Nair, N. L.; Taychatanapat, T.; Watanabe, K.; Taniguchi, T.; Levitov, L. S.; Jarillo-Herrero, P., Hot carrier-assisted intrinsic photoresponse in graphene. *Science* **2011**, *334* (6056), 648-652.
184. Freitag, M.; Low, T.; Xia, F.; Avouris, P., Photoconductivity of biased graphene. *Nature Photonics* **2013**, *7* (1), 53-59.
185. Grigorenko, A. N.; Nikitin, P. I.; Jelski, D. A.; George, T. F., Thermoelectric phenomena in metals under large temperature gradients. *Journal of Applied Physics* **1991**, *69* (5), 3375-3377.
186. Mahan, G. D., The Benedicks effect: Nonlocal electron transport in metals. *Physical Review B* **1991**, *43* (5), 3945-3951.

187. Chaves, F. A.; Jiménez, D.; Santos, J. E.; Bøggild, P.; Caridad, J. M., Electrostatics of metal–graphene interfaces: sharp p–n junctions for electron-optical applications. *Nanoscale* **2019**, *11* (21), 10273-10281.
188. Lee, G.-H.; Park, G.-H.; Lee, H.-J., Observation of negative refraction of Dirac fermions in graphene. *Nature Phys.* **2015**, *11* (11), 925-929.
189. Rotenberg, N.; Kuipers, L., Mapping nanoscale light fields. *Nature Photonics* **2014**, *8* (12), 919-926.
190. Yu, T.; Kravets, V. G.; Imaizumi, S.; Grigorenko, A. N., Effect of dielectric fabrication techniques on graphene gating. *The Journal of Physical Chemistry C* **2020**, *125* (1), 865-872.
191. Novoselov, K. S.; Geim, A. K.; Morozov, S. V.; Jiang, D.; Katsnelson, M. I.; Grigorieva, I. V.; Dubonos, S. V.; Firsov, A. A., Two-dimensional gas of massless Dirac fermions in graphene. *Nature* **2005**, *438* (7065), 197-200.
192. Li, Z. Q.; Henriksen, E. A.; Jiang, Z.; Hao, Z.; Martin, M. C.; Kim, P.; Stormer, H. L.; Basov, D. N., Dirac charge dynamics in graphene by infrared spectroscopy. *Nature Phys.* **2008**, *4* (7), 532-535.
193. Ansell, D.; Radko, I. P.; Han, Z.; Rodriguez, F. J.; Bozhevolnyi, S. I.; Grigorenko, A. N., Hybrid graphene plasmonic waveguide modulators. *Nat Commun* **2015**, *6*.
194. Schedin, F.; Geim, A. K.; Morozov, S. V.; Hill, E. W.; Blake, P.; Katsnelson, M. I.; Novoselov, K. S., Detection of individual gas molecules adsorbed on graphene. *Nature Materials* **2007**, *6* (9), 652-655.
195. Manning, M. F.; Bell, M. E., Electrical conduction and related phenomena in solid dielectrics. *Reviews of Modern Physics* **1940**, *12* (3), 215-256.
196. Liu, M.; Yin, X.; Ulin-Avila, E.; Geng, B.; Zentgraf, T.; Ju, L.; Wang, F.; Zhang, X., A graphene-based broadband optical modulator. *Nature* **2011**, *474* (7349), 64-67.
197. Lemme, M. C.; Echtermeyer, T. J.; Baus, M.; Kurz, H., A graphene field-effect device. *IEEE Electron Device Letters* **2007**, *28* (4), 282-284.
198. Schwierz, F., Graphene transistors. *Nature Nanotechnology* **2010**, *5* (7), 487-496.
199. Wang, H.; Wu, Y.; Cong, C.; Shang, J.; Yu, T., Hysteresis of electronic transport in graphene transistors. *ACS Nano* **2010**, *4* (12), 7221-7228.

200. Liao, Z.-M.; Han, B.-H.; Zhou, Y.-B.; Yu, D.-P., Hysteresis reversion in graphene field-effect transistors. *The Journal of Chemical Physics* **2010**, *133* (4), 044703.
201. Xu, H.; Chen, Y.; Zhang, J.; Zhang, H., Investigating the mechanism of hysteresis effect in graphene electrical field device fabricated on SiO<sub>2</sub> substrates using Raman spectroscopy. *Small* **2012**, *8* (18), 2833-40.
202. Friedemann, M.; Woszczyzna, M.; Müller, A.; Wundrack, S.; Dziomba, T.; Weimann, T.; Ahlers, F. J., Versatile sputtering technology for Al<sub>2</sub>O<sub>3</sub> gate insulators on graphene. *Science and Technology of Advanced Materials* **2012**, *13* (2), 025007.
203. Mohrmann, J.; Watanabe, K.; Taniguchi, T.; Danneau, R., Persistent hysteresis in graphene-mica van der waals heterostructures. *Nanotechnology* **2014**, *26* (1), 015202.
204. Aznakayeva, D. E.; Rodriguez, F. J.; Marshall, O. P.; Grigorenko, A. N., Graphene light modulators working at near-infrared wavelengths. *Opt. Express* **2017**, *25* (9), 10255-10260.
205. Pirkle, A.; Chan, J.; Venugopal, A.; Hinojos, D.; Magnuson, C. W.; McDonnell, S.; Colombo, L.; Vogel, E. M.; Ruoff, R. S.; Wallace, R. M., The effect of chemical residues on the physical and electrical properties of chemical vapor deposited graphene transferred to SiO<sub>2</sub>. *Applied Physics Letters* **2011**, *99* (12), 122108.
206. Kalon, G.; Jun Shin, Y.; Giang Truong, V.; Kalitsov, A.; Yang, H., The role of charge traps in inducing hysteresis: capacitance–voltage measurements on top gated bilayer graphene. *Applied Physics Letters* **2011**, *99* (8), 083109.
207. Lafkioti, M.; Krauss, B.; Lohmann, T.; Zschieschang, U.; Klauk, H.; Klitzing, K. v.; Smet, J. H., Graphene on a Hydrophobic Substrate: Doping Reduction and Hysteresis Suppression under Ambient Conditions. *Nano Letters* **2010**, *10* (4), 1149-1153.
208. Barreca, D.; Milanov, A.; Fischer, R. A.; Devi, A.; Tondello, E., Hafnium oxide thin film grown by ALD: an XPS study. *Surface Science Spectra* **2007**, *14* (1), 34-40.
209. Wang, X.; Han, K.; Wang, W.; Xiang, J.; Yang, H.; Zhang, J.; Ma, X.; Zhao, C.; Chen, D.; Ye, T., Band alignment of HfO<sub>2</sub> on SiO<sub>2</sub>/Si structure. *Applied Physics Letters* **2012**, *100* (12), 122907.
210. Dupin, J.-C.; Gonbeau, D.; Vinatier, P.; Levasseur, A., Systematic XPS studies of metal oxides, hydroxides and peroxides. *Physical Chemistry Chemical Physics* **2000**, *2* (6), 1319-1324.

211. Chowdhury, N. A.; Garg, R.; Misra, D., Charge trapping and interface characteristics of thermally evaporated HfO<sub>2</sub>. *Applied Physics Letters* **2004**, 85 (15), 3289-3291.
212. Gritsenko, V. A.; Perevalov, T. V.; Islamov, D. R., Electronic properties of hafnium oxide: a contribution from defects and traps. *Physics Reports* **2016**, 613, 1-20.
213. Strand, J.; Dicks, O. A.; Kaviani, M.; Shluger, A. L., Hole trapping in amorphous HfO<sub>2</sub> and Al<sub>2</sub>O<sub>3</sub> as a source of positive charging. *Microelectronic Engineering* **2017**, 178, 235-239.
214. Groner, M. D.; Elam, J. W.; Fabreguette, F. H.; George, S. M., Electrical characterization of thin Al<sub>2</sub>O<sub>3</sub> films grown by atomic layer deposition on silicon and various metal substrates. *Thin Solid Films* **2002**, 413 (1), 186-197.
215. Lohmann, T.; von Klitzing, K.; Smet, J. H., Four-terminal magneto-transport in graphene p-n junctions created by spatially selective doping. *Nano Letters* **2009**, 9 (5), 1973-1979.
216. Joshi, P.; Romero, H. E.; Neal, A. T.; Toutam, V. K.; Tadigadapa, S. A., Intrinsic doping and gate hysteresis in graphene field effect devices fabricated on SiO<sub>2</sub> substrates. *J Phys Condens Matter* **2010**, 22 (33), 334214.
217. Lafkioti, M.; Krauss, B.; Lohmann, T.; Zschieschang, U.; Klauk, H.; Klitzing, K. V.; Smet, J. H., Graphene on a hydrophobic substrate: doping reduction and hysteresis suppression under ambient conditions. *Nano Lett* **2010**, 10 (4), 1149-53.